The simulation of shock- and impact-driven flows with Mie-Grüneisen equations of state

Thesis by

Geoffrey M Ward

In Partial Fulfillment of the Requirements

for the Degree of

Doctor of Philosophy

California Institute of Technology

Pasadena, California

2011

(Defended December 3rd, 2010)

Dedicated to my family

Acknowledgements

Firstly, I must thank my thesis advisor Professor Dale Pullin for his patience and guidance over the past few years. Without his depth of knowledge and willingness to provide many thoughtful discussions this work would have been nearly impossible to complete. Secondly, I would like to thank my thesis committee, Professors Joe Shepherd, Tim Colonius, and Dan Meiron, for their contributions over the years. In particular, having been a student in several of the classes they taught, I would like to thank each of them for making time to educate students like myself through courses offered each year.

Additionally, I must thank several other people affiliated with Caltech. Firstly, I am grateful to David Hill for the many always insightful conversations on various topics. His working notes on solid mechanics were an invaluable reference for learning the topic from the viewpoint of someone with a background in fluids mechanics. Furthermore, the codes which he developed provided a convenient basic framework on which most of my own work was built. I would also like to thank Manuel Lombardini for his help in getting me acquainted with the Virtual Test Facility (VTF) codes early on in my career and for his willingness to share insight regarding my work. I must also extend my appreciation to the CACR computing staff for their support in keeping everything working, particularly Sharon Brunett for always responded to emails in a timely fashion. Most importantly, I would like to thank Adam Norman for his friendship and entertainment, including everything from flying, hiking, and surfing, to racquetball, tennis, and ping pong, throughout the years. I would also like to thank Michio Inoue for the many enjoyable rounds of golf.

Next, I would like to thank Marianne Francois for the opportunity to partake in a three-month internship at Los Alamos National Laboratory and for agreeing to mentor me throughout the process. The time I spent at LANL was very enjoyable and provided many valuable learning opportunities. Also, I must give thanks to Ralf Deiterding of Oak Ridge National Laboratory for his willingness to respond quickly and insightfully to any emails I sent regarding coding issues.

I would also like to thank the many excellent Professors at the University of Arizona that influenced me during my undergraduate studies. Among those fine teachers, I would like to single out and extend my gratitude to Professors Jeff Jacobs, Frank Champagne, and Thomas Balsa. I would like to extend further special thanks to Jeff Jacobs for giving me the opportunity to participate and

interact with graduate students in his experimental facilities through independent study.

Finally, I would like to thank my family for all their continuing support. There is nothing more valuable than having a supportive family and for that reason I dedicate my thesis to them. In particular, I would like to thank my wife Fei for her enduring love and commitment through the good and bad.

I must acknowledge the financial support of the department of energy (DOE) throughout my time at Caltech. Funding was initially provided under the Advanced Simulation and Computing (ASC) program, subcontract no. B341492 of DOE contract W-7405-ENG-48. Following the end of the ASC project the material was then based upon work supported by the Department of Energy National Nuclear Security Administration under Award Number DE-FC52-08NA28613 for the Predictive Science Academic Alliance Program (PSAAP).

Abstract

An investigation of shock- and impact-driven flows with Mie-Grüneisen equation of state derived from a linear shock-particle speed Hugoniot relationship is presented. Cartesian mesh methods using structured adaptive refinement are applied to simulate several flows of interest in an Eulerian frame of reference. The flows central to the investigation include planar Richtmyer-Meshkov instability, the impact of a sphere with a plate, and an impact-driven Mach stem.

First, for multicomponent shock-driven flows, a dimensionally unsplit, spatially high-order, hybrid, center-difference, limiter methodology is developed. Effective switching between center-difference and upwinding schemes is achieved by a set of robust tolerance and Lax-entropy-based criteria [49]. Oscillations that result from such a mixed stencil scheme are minimized by requiring that the upwinding method approaches the center-difference method in smooth regions. To attain this property a blending limiter is introduced based on the norm of the deviation of WENO reconstruction weights from ideal. The scheme is first demonstrated successfully for the linear advection equation in spatially fourth- and sixth-order forms. A spatially fourth-order version of the method that combines a skew-symmetric kinetic-energy preserving center-difference scheme with a Roe-Riemann solver is then developed and implemented in Caltech's Adaptive Mesh Refinement, Object-oriented C++ (AMROC) [16, 17] framework for Euler flows.

The solver is then applied to investigate planar Richtmyer-Meshkov instability in the context of an equation of state comparison. Comparisons of simulations with materials modeled by isotropic stress Mie-Grüneisen equations of state derived from a linear shock-particle speed Hugoniot relationship [36, 52] to those of perfect gases are made with the intention of exposing the role of the equation of state. First, results for single- and triple-mode planar Richtmyer-Meshkov instability between mid-ocean ridge basalt (MORB) and molybdenum modeled by Mie-Grüneisen equations of state are presented for the case of a reflected shock. The single-mode case is explored for incident shock Mach numbers of 1.5 and 2.5. For the planar triple-mode case a single incident Mach number of 2.5 is examined with the initial corrugation wave numbers related by $k_1 = k_2 + k_3$. A comparison is drawn to Richtmyer-Meshkov instability in fluids with perfect gas equations of state utilizing matching of a nondimensional pressure jump across the incident shock, the post-shock Atwood ratio, post-shock amplitude-to-wavelength ratio, and time nondimensionalized by the Rcithmyer

linear-growth rate time constant prediction. Result comparison demonstrates difference in start-up time and growth rate oscillations. Growth rate oscillation frequency is seen to correlate directly to the expected oscillation frequency of the transmitted and reflected shocks. For the single-mode cases, further comparison is given for vorticity distribution and corrugation centerline shortly after shock interaction that demonstrates only minor differences.

Additionally, examined is single-mode Richtmyer-Meshkov instability when a reflected expansion wave is present for incident Mach numbers of 1.5 and 2.5. Comparison to perfect gas solutions in such cases yields a higher degree of similarity in start-up time and growth rate oscillations. Vorticity distribution and corrugation centerline shortly after shock interaction is also examined. The formation of incipient weak shock waves in the heavy fluid driven by waves emanating from the perturbed transmitted shock is observed when an expansion wave is reflected.

Next, the ghost fluid method [83] is explored for application to impact-driven flows with Mie-Grüneisen equations of state in a vacuum. Free surfaces are defined utilizing a level-set approach. The level-set is reinitialized to the signed distance function periodically by solution to a Hamilton-Jacobi differential equation in artificial time. Flux reconstruction along each Cartesian direction of the domain is performed by subdividing in a way that allows for robust treatment of grid-scale sized voids. Ghost cells in voided regions near the material-vacuum interface are determined from surface-normal Riemann problem solution. The method is then applied to several impact problems of interest. First, a one-dimensional impact problem is examined in Mie-Grüneisen aluminum with simple point erosion used to model separation by spallation under high tension. A similar three-dimensional axisymmetric simulation of two rods impacting is then performed without a model for spallation. Further results for three-dimensional axisymmetric simulation of a sphere hitting a plate are then presented.

Finally, a brief investigation of the assumptions utilized in modeling solids as isotropic fluids is undertaken. An Eulerian solver approach to handling elastic and elastic-plastic solids is utilized for comparison to the simple fluid model assumption. First, in one dimension an impact problem is examined for elastic, elastic-plastic, and fluid equations of state for aluminum. The results demonstrate that in one dimension the fluid models the plastic shock structure of the flow well. Further investigation is made using a three-dimensional axisymmetric simulation of an impact problem involving a copper cylinder surrounded by aluminum. An aluminum slab impact drives a faster shock in the outer aluminum region yielding a Mach reflection in the copper. The results demonstrate similar plastic shock structures. Several differences are also notable that include a lack of roll-up instability at the material interface and slip-line emanating from the Mach stem's triple point.

Contents

List of Figures

List of Tables

Chapter 1

Introduction

1.0.1 Shock-driven flows

1.0.1.1 Overview

The impulsive acceleration of a corrugated material contact by a shock wave is one of the most fundamental research topics in the area of compressible flows. Applications for such research are numerous and vast in complexity, ranging from supernovas to inertial confinement fusion (ICF) to hypervelocity impacts in solids. Richtmyer [71] and Meshkov [53] were first to draw attention to the topic, proposing a simple incompressible model that leads to a linear growth prediction for the corrugation amplitude. A great deal of research has been performed on Richtmyer-Meshkov instability since its introduction [14, 25, 33–35, 39, 41, 50, 60, 89, 93, 93–95, 98]. The present focus of this investigation is on the role of the equation of state. A numerical comparison between simulations of planar Richtmyer-Meshkov instability in fluids with Mie-Grüneisen equation of state derived from shock Hugoniots of solids and perfect gases is undertaken. The majority of prior numerical studies of Richtmyer-Meshkov instability have focused on the perfect gas equation of state. These studies often have a constant specific heat ratio owing to challenges associated with the numerical modeling of multiphase Mie-Grüneisen flows [2]. Presently, in Chapter 3 a low dissipation hybrid solver is developed to address such numerical challenges created by the Mie-Grüneisen equation of state. The solver is implemented as a patch solver in Caltech's virtual test facility (VTF) software suite that utilizes object-oriented C++ adaptive mesh refinement (AMROC) [15–17].

1.0.1.2 Richtmyer-Meshkov instability background

Two distinct variations of Richtmyer-Meshkov instability are commonly noted. The first, more commonly studied, involves a shock wave that begins in a lighter fluid and travels until it reaches a corrugated interface with a heavier fluid. Upon the shock interacting with the material contact, the misaligned gradients of thermodynamic quantities cause baroclinic deposition of vorticity leading to growth of the corrugation amplitude. Transmitted and reflected shock waves move away from

the post-shock corrugation. This situation, often denoted as "light-to-heavy" Richtmyer-Meshkov instability, is schematically depicted in figure 1.1(a). To the right of the schematic, Figure 1.1(b), is a wave diagram for the related zero-corrugation Riemann problem showing the position of the shocks and material contact as a function of time. The frame of reference, as is the case for all simulations presented here, is such that the interface is stationary post-shock for zero-corrugation amplitude. Figure 1.2(a) depicts the second case of interest in which a reflected expansion wave occurs instead of a shock. Although it is also possible to achieve a reflected shock for such cases, in general, a reflected expansion wave occurs when the shock starts out in the heavy fluid. For this reason the reflected expansion situation is referred to as "heavy-to-light" Richtmyer-Meshkov instability. For such cases a phase reversal of the corrugation is also observed due to the difference in the direction of the density gradient yielding baroclinic vorticity generation opposite in sign to that of the "light-to-heavy" case. The wave diagram for the associated zero-corrugation problem is depicted in Figure 1.2(b). Due to the difference in the reflected wave created by the shock-corrugation interaction in the above discussed situations, variation in the solution of these two fundamental cases is expected.

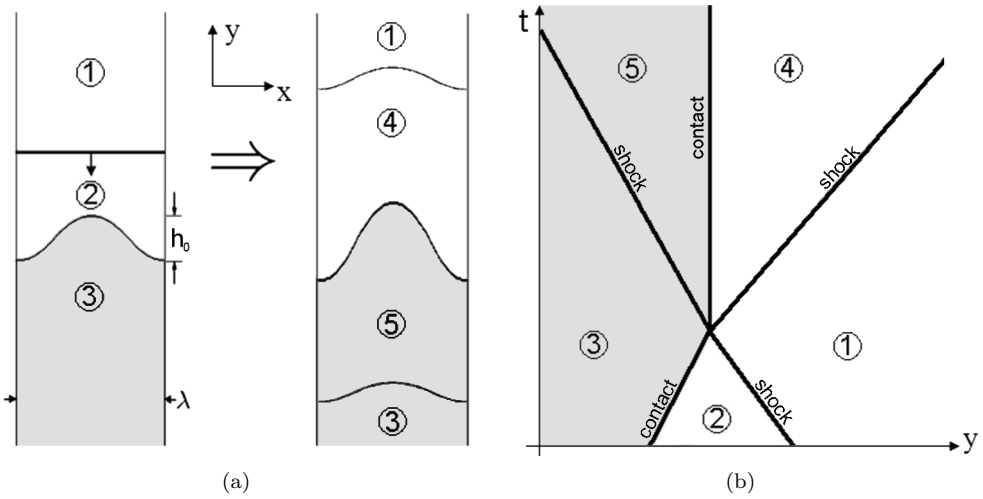

Figure 1.1: (a) Schematic depiction of Richtmyer-Meshkov instability for the case in which the shock starts in the light fluid, resulting in perturbed reflected and transmitted shock waves. (b) Schematic depiction of the y-t diagram for the associated one-dimensional Riemann problem

1.0.1.3 Comparison study overview

In attempting to make comparison between flows with different equations of state it is useful to try to create some level of flow similarity. A variety of theoretical and experimental work has been performed on Richtmyer-Meshkov instability that yields insight into what would be required to achieve a high level of similarity. From simple consideration of the associated one-dimensional Riemann problem it is clear that a set of nondimensional parameters involving corrugation wavenumber, shock

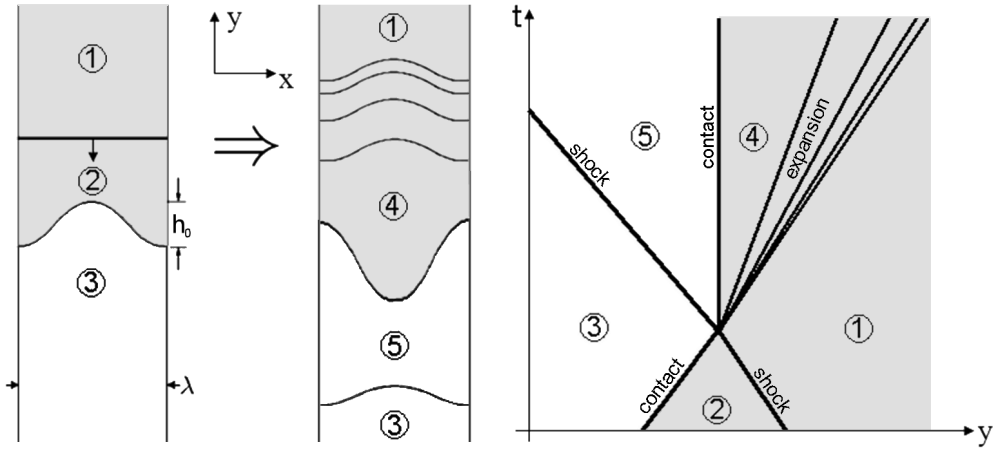

(a) (b)

Figure 1.2: (a) Schematic depiction of Richtmyer-Meshkov instability for the case in which the shock starts in the heavy fluid, typically resulting in a perturbed reflected expansion and transmitted shock waves. (b) Schematic depiction of the y-t diagram for the associated one-dimensional Riemann problem

speeds, speeds of sound, densities, shock Hugoniot slopes, and incident shock strength are important for achieving similarity in the case of a small corrugation. The matching of all the quantities in any such nondimensional set for flows with vastly different equations of state is not likely achievable. This is the underlying motivation for the present study and comparison. For present purposes, in spite of the impossibility of achieving full similarity, several key parameters are matched between flows. The choice of these parameters is somewhat arbitrary, but provides a useful basis for comparison. The quantities matched are the post-shock Atwood ratio, a nondimensional pressure ratio across the incident shock, the ratio of post-shock corrugation amplitude-to-wavelength ratio, and time nondimensionalized by the Richtmyer growth rate prediction time constant. A parameter study of two arbitrary Mach numbers of 1.5 and 2.5 in fluids with Mie-Grüneisen equations of state forms a basis for comparison of single-mode instability. A matching set of initial conditions for perfect gas flows is generated based on these two cases.

Results of the numerical investigation begin in Section 4.4 for two incident shock Mach numbers, 1.5 and 2.5 in the "light-to-heavy" case with a single-mode corrugation in fluids with Mie-Grüneisen equation of state. For comparison purposes also examined is the equivalent matched perfect gas cases. For both equations of state, amplitude and growth rate results are examined in detail in Section 4.4 followed by integral vorticity in Section 4.4.3 and corrugation centerline shortly post-shock in Section 4.4.4. For a single incident Mach number of 2.5, in Section 4.5 next examined is a triple-mode case with the three corrugation wave numbers related by the property that $k_1 = k_2 + k_3$ and $k_1 h_1 = k_2 h_2 = k_3 h_3$. Instability amplitude and growth rate are again examined for both equations of state in Section 4.5.1. Lastly, in Section 4.6 single-mode "heavy-to-light" Richtmyer-Meshkov

instability results are presented. Again two Mach numbers are utilized to compare amplitude and growth rate in Section 4.6.1 as well as post-shock integral vorticity in Section 4.6.2 and centerline distributions in Section 4.6.3 between equations of state.

1.0.1.4 Numerical methods background

In the presence of shocks and interfaces, compressible flows involve both smooth and nearly discontinuous features. In addition to the many challenges associated with simulating Euler flow of perfect gases with such features, creation of a multiphase solver for linear shock-particle centered Hugoniot Mie-Grüneisen equation of state must address several special difficulties. Firstly, whereas many miscible gas mixtures can be well modeled by Dalton's law of partial pressures, no single simple multiphase miscible or immiscible mixture rule exists. Additionally, for multiphase flows catastrophic phase-error driven oscillations can develop without proper numerical treatment [2]. Eulerian Cartesian mesh numerical methods that mitigate such oscillations by separating phases have been proposed that use a pseudo physical mixture rule or a contact model [22, 57], but are generally dissipative in multiphase regions. An alternative approach to modeling immiscible multiphase Mie-Grüneisen flows is to use an ad hoc fluid mixture rule and track additional variables related to the equation of state [4, 81], which allows for more flexibility in the numerical approach utilized. In Chapter 3 a new generalized set of limiters based on WENO [37, 48, 79] is developed that allows for high-order Eulerian schemes to be blended with lower-order upwinding schemes in a robust manner. In conjunction with an ad hoc material mixture Cartesian mesh method that addresses phase-error oscillations [81], these limiters allow for the creation of a new hybrid scheme that combines a high-order skew-symmetric kinetic-energy preserving center-difference [65] approach in smooth flow regions with low-order upwinding at discontinuities for multiphase Mie-Grüneisen flows.

1.0.2 Impact-driven flows

1.0.2.1 Overview

The focus of Caltech's participation in the Predictive Science Academic Alliance Program (PSAAP) program is the validation of simulations of hypervelocity impacts in metallic projectiles and targets. In the spirit of this purpose a brief investigation of an extension of the ghost fluid method [8, 22] for single phase free surface flows with linear shock-particle centered Hugoniot Mie-Grüneisen equation of state is undertaken in Chapter 5. The method is first applied in a one-dimensional impact problem with a simple erosion model for spallation. A corresponding rod impact problem is simulated in the axisymmetric case. Finally, to demonstrate the potential further use of such a solver for hypervelocity impacts in solids, the method is applied to study the three-dimensional axisymmetric impact of an

aluminum sphere and plate modeled as Mie-Grüneisen fluids.

1.0.2.2 Numerical methods background

Impact-driven flows with free surfaces present additional numerical challenges in a fixed grid Eulerian setting. Whereas Lagrangian methods provide a natural approach to keeping track of the free surface and applying traction conditions [21, 62], Eulerian solvers require interpolation of Cartesian mesh data to apply traction conditions and advect the free surface. As was previously discussed, for shock-driven flows a low-dissipation mixed-phase Eulerian solver approach can be utilized to study problems with moderate material property variation between phases. However, such a approach cannot be applied to free surfaces due to their inherently one-sided nature. Instead, the methods required to properly treat vacuum-material interfaces are one-sided upwinding schemes. The ghost fluid and volume of fluid (VOF) method were proposed independently to handle material interfaces, but lend themselves to handle vacuum interfaces as well [22, 57].

For simplicity, although not even conservative in its original implementation, the ghost fluid method is presently extended for fluid-vacuum simulations with the addition of an algorithm for handling single cell sized voids. The ghost fluid method was originally proposed to address the catastrophic oscillations that develop in mixed-phase flux-splitting schemes by separating the phases through a scalar with a sign change referred to as a level-set [22]. For vacuum-interface problems traction conditions can be achieved by tracing out tangent curves to the signed distance function and the solving surface normal Riemann problems to determine ghost cell values. The signed distance function must therefore be calculated periodically [22, 26, 75]. It is important that mechanical information not traverse across small voids for proper treatment of such problems. To address this issue an approach that subdivides the domain utilizing the signed distance function is introduced.

1.0.3 Eulerian solid mechanics

1.0.3.1 Overview

The fundamental difference between solids and fluids is the ability of solids to resist continuous deformation under shear stresses. Therefore utilizing an isotropic stress Mie-Grüneisen equation of state model should not be expected to give realistic results when shear is important. However, many solids can only support a limited amount of anisotropic stress due to plasticity [66, 67, 91]. For this reason an isotropic stress model should be expected to capture at least some solution features for many ductile solids under high compressive stress. In Chapter 6 an exploration of the assumptions of the Mie-Grüneisen fluid equation of state are undertaken in the context of comparison to elastic-plastic metals for several simulations. An Eulerian Cartesian mesh method is utilized to simulate the elastic-plastic solids [30]. First, in one dimension a simple impact problem

is modeled with elastic, elastic-plastic, and fluid Mie-Grüneisen models. Secondly, an axisymmetric three-dimensional simulation is preformed of a two phase problem involving a semi-infinite length copper cylinder surrounded by an aluminum slab struck by a semi-infinite aluminum slab. A Mach disc is generated in the inner copper cylinder traveling along at the same speed as the planar shock in the outer aluminum [11].

Chapter 2

The Mie-Grüneisen equation of state

In a completely general manner, an isotropic stress equation of state can be rigorously constructed about a parametric reference state curve through an integral equation. Choosing to construct pressure as a function of internal energy and density leads to the very convenient Grüneisen formalism

$$p(\rho, e) = p_{ref}(\rho) + \rho \int_{e_{ref}(\rho)}^{e} \Gamma(\rho, e')de', \tag{2.1}$$

where $p_{ref}(\rho)$ and $e_{ref}(\rho)$ form a density parameterized reference state curve and $\Gamma(\rho, e)$ is the Grüneisen parameter defined by

$$\Gamma(\rho, e) = \frac{1}{\rho} \frac{\partial p}{\partial e}\Big|_{\rho}. \tag{2.2}$$

A material is then well defined thermodynamically by $p_{ref}(\rho)$, $e_{ref}(\rho)$, and $\Gamma(\rho, e)$. In practice, whether analytic or tabulated, these three functions should, at a minimum, result in the thermodynamic stability of the material modeled in state regions of interest [57].

2.0.4 Hugoniots as reference state curves

For the simulation of compressible flows involving shocks it is convenient to use shock Hugoniots for reference state curves [36, 52, 73]. For many solids of interest, starting from state ρ_0, p_0, e_0, experimental data indicates that over a large range of shock strengths the relationship between shock and particle speed is adequately approximated by a simple linear fit [36, 52, 73]

$$u_s = c_0 + \sigma u_p, \tag{2.3}$$

where u_s is the shock's speed, u_p is the post-shock particle speed, c_0 is the unshocked medium's speed of sound, and σ is related to the unshocked medium's isentropic derivative of the bulk modulus

K_s with respect to pressure

$$\begin{aligned} K_s &= \left.\frac{\partial \ln(p)}{\partial \rho}\right|_s, \\ \sigma &= \left(\left.\frac{\partial K_s}{\partial p}\right|_s + 1\right)\Big/4. \end{aligned} \tag{2.4}$$

Utilizing (2.3) and the three Rankine-Hugoniot jump conditions for conservation of mass, momentum, and energy,

$$\begin{aligned} \rho &= \rho_0 u_s/(u_s - u_p), \\ p &= p_0 + \rho_0 u_s u_p, \\ e &= e_0 + \tfrac{1}{2}(p + p_0)(1/\rho_0 - 1/\rho), \end{aligned} \tag{2.5}$$

results in the internal pressure and energy parametrized as functions of density along the shock Hugoniot [81],

$$p_{_H}(\rho) = p_0 + \frac{c_0^2(1/\rho_0 - 1/\rho)}{[1/\rho_0 - \sigma(1/\rho_0 - 1/\rho)]^2}, \tag{2.6}$$

$$e_{_H}(\rho) = e_0 + \frac{1}{2}(p_{_H}(\rho) + p_0)(1/\rho_0 - 1/\rho). \tag{2.7}$$

Additionally, for many solids it is approximated that the Grüneisen parameter is given by [57]

$$\begin{aligned} \Gamma(\rho, e) &= \Gamma_0\left(\frac{\rho_0}{\rho}\right)^q \\ &= \Gamma_{_H}(\rho). \end{aligned} \tag{2.8}$$

In terms of internal energy this is a first-order approximation to $\Gamma(\rho, e)$ near the Hugoniot:

$$\begin{aligned} \Gamma(\rho, e) &= \Gamma(\rho, e_{_H}(\rho)) + \left.\frac{\partial \Gamma}{\partial e}\right|_{\rho, e_{_H}(\rho)} (e - e_{_H}(\rho)) + ... \\ &= \Gamma_{_H}(\rho) + O(\Delta e). \end{aligned} \tag{2.9}$$

Thus the equation of state is a first-order approximation in internal energy near the central Hugoniot with

$$p(\rho, e) = p_{_H}(\rho) + \rho \Gamma_{_H}(\rho)(e - e_{_H}(\rho)). \tag{2.10}$$

Generally, (2.6) and (2.7) are only valid for compressed states $\rho > \rho_0$. For expanded states a second-order isentropic continuation to the Hugoniot known as a Murnaghan isentrope is sometimes used [57]:

$$p_{_H}(\rho) = \left(p_0 + \frac{\rho_0 c_0^2}{4\sigma - 1}\right)\left(\frac{\rho}{\rho_0}\right)^{4\sigma - 1} - \frac{\rho_0 c_0^2}{4\sigma - 1}, \tag{2.11}$$

$$e_{_H}(\rho) = e_0 + \int_{\rho_0}^{\rho} \frac{p_{_H}(\rho)}{\rho^2} d\rho. \tag{2.12}$$

$$\tag{2.13}$$

Table 2.1: Hugoniot constants for various materials. For further shock-particle Hugoniot constants refer to [36, 52, 73]

	ρ_0	p_0	Γ_0	c_0	σ	q	T_0
aluminum	2785 kg/m^3	0.0	2.0	5328 m/s	1.338	1.0	298 K
MORB	2660 kg/m^3	0.0	1.18	2100 m/s	1.68	1.0	1673 K
molybdenum	9961 kg/m^3	0.0	1.56	4700 m/s	1.43	1.0	1673 K

2.0.5 Equation of state limitations

Construction of a central Hugoniot utilizing the assumption of a linear shock-particle speed relationship and Murnaghan isentrope extension for expanded states result in two notable limitations. First, using a simple linear fit to the relationship between shock and particle speed causes a singularity in the equation of state that results in a nonphysical maximum density

$$\rho_{max} = \frac{\rho_0}{1 - 1/\sigma}, \tag{2.14}$$

when $\sigma > 1$, as is typical for solids. Second, analysis of isentropes created by the extension of the Hugoniot for expanded states via the Murnaghan isentrope demonstrates a non-physical minimum pressure [90]:

$$\frac{dp}{d\rho}\Big|_s = c_1 \frac{p}{\rho^2} + c_2 \frac{1}{\rho^2} + c_3 \rho^{4\sigma-3} + c_4 \rho^{4\sigma-2} \tag{2.15}$$

along any isentrope when $\rho < \rho_0$ and $p < p_0$, where c_1, c_2, c_3, and c_4 depend on the central Hugoniot constants. Integrating (2.15) from initial conditions ρ_i, p_i, and s_i yields

$$\begin{aligned} p(\rho, s_i) \quad = \quad & (p_i + \tfrac{c_2}{c_1}) e^{c_1(1/\rho_i - 1/\rho)} - \tfrac{c_2}{c_1} \\ & + e^{c_1/\rho} \textstyle\int_{\rho_i}^{\rho} (c_3 {\rho'}^{4\sigma-3} + c_4 {\rho'}^{4\sigma-2}) e^{c_1/\rho'} d\rho'. \end{aligned} \tag{2.16}$$

When approached from the part of the $p - \rho$ plane of physical interest, the limit

$$\lim_{\rho \to 0} p(\rho, s_i) \to -\frac{c_2}{c_1} = \frac{-\rho_0 c_0^2}{4\sigma - 1} \tag{2.17}$$

is obtained for all associated isentropes when $\sigma > 1/2$. Therefore no pressures lower than

$$p_{min} = \frac{-\rho_0 c_0^2}{4\sigma - 1} \tag{2.18}$$

are attainable. With $\rho_0 > 0$, $c_0 > 0$, and $\sigma > 0$ it is clear that $p_{min} < 0$ is typical and therefore negative pressure or tension is permissible. It is useful to place a tensile strength limitation when tension is expected in a simulation. Additionally, positivity of absolute temperature must not be violated. Taking constant specific heat for aluminum yields Figure 2.1, giving some face to the expected $p - \rho$ plane of validity.

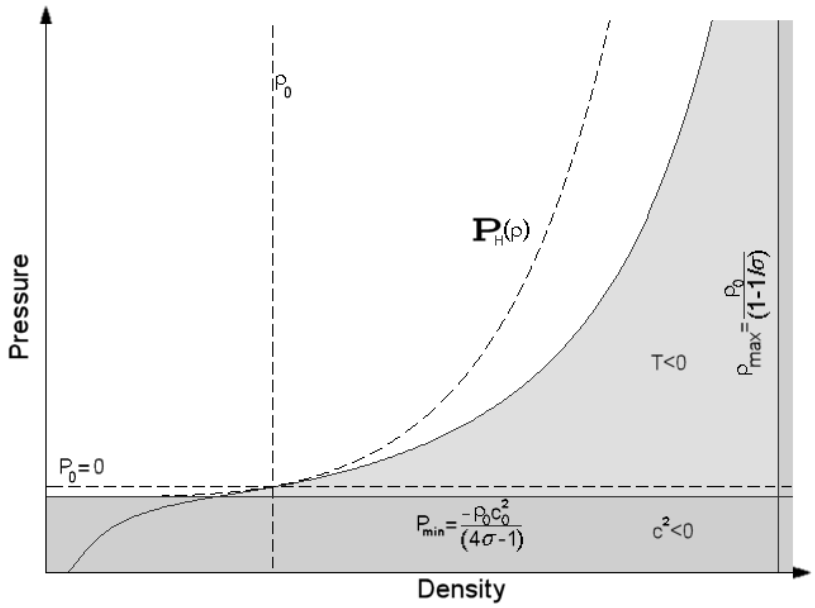

Figure 2.1: Forbidden and allowed state regions of the Mie-Grüneisen equation of state formulated from a linear shock-particle speed central shock Hugoniot and Murnaghan isentrope extension for expanded states. The available states are bounded by negative temperature, a nonphysical minimum pressure, and a nonphysical maximum density.

2.0.6 Mixture rules

Kinetic theory for ideal gas mixtures predicts that total pressure is described by partial pressure summation [40]. For mixtures of perfect gases this law is easily applied to form an analytic equation of state [85],

$$p = (1 - \bar{\gamma})\rho e, \tag{2.19}$$

with

$$\bar{\gamma} = \sum_{i=1}^{n} y_i c_p^i \Big/ \sum_{i=1}^{n} y_i c_v^i \tag{2.20}$$

where y_i, c_p^i, and c_v^i are the ith components mass fraction and specific heats, respectively. Presently, the above mixture rule for perfect gases is applied in simulations. However, for most real materials such a simple theory for molecular interactions in mixtures does not exist. Owing to the complexity inherent in providing a physical mixture model for real materials, previous works addressing the simulation of multiphase flows typically assume discontinuous contact between materials, tracking the contact [57] and applying some isentropic relaxation of phases to mechanical equilibrium or smearing it with an ad hoc mixture rule [4, 81]. An ad hoc blending of parameters is currently used,

$$x_0^{mix} = \sum_{i=1}^{n} \psi_0^i x_0^i, \tag{2.21}$$

where x_0^i is replaced in the formula by the Hugoniot parameters, ρ_0, p_0, e_0, Γ_0, and σ of the ith material. Although in principal this model is not physical, the weak convergence of solutions with discontinuous interfaces should still result.

Chapter 3

Hybrid, center-difference, limiter solver

In the following sections the special difficulties associated with building a hybrid solver for multiphase flows with Mie-Grüneisen equations of state are addressed. For Euler flows a continuous transition from low-order upwinding at discontinuities to high-order low dissipation in smooth regions is desirable. A substantial amount of literature on hybrid solvers for perfect gases exist focusing on the use of WENO interpolation [3, 29, 68]. WENO provides a very natural way to create a hybrid scheme for hyperbolic partial differential equations in the way that it combines sub-stencils based on smoothness measures in order to produce a low-order approximation at sharp features and high-order at smooth solution regions. Designing the desired high-order stencil WENO becomes in smooth solution regions allows for dispersion relation matching to a high-order center-difference scheme for small wave numbers [29]. However, these WENO methods commonly apply a flux-splitting reconstruction approach that is conservative, but fails to prevent catastrophic oscillations [2] at contacts in many Mie-Grüneisen fluids (see Figure 3.1), rendering such methods inadequate. An alternative primitive variable WENO-reconstruction based Roe-Riemann solver [72] has been developed by Johnsen and Colonius [38] that prevents such oscillations from developing in mixtures of perfect gases. However, the stencil associated with any such Riemann solver is dependent on the flow locally and therefore the dispersion relation is complex and does not lend itself to hybrid methodology. For multiphase flows with Mie-Grüneisen equations of state Miller and Puckett [57] developed a volume of fluid approach that utilizes an approximate Riemann solver, again yielding no ideal stencil for smooth flows. Likewise, Shyue [81] has extended Roe's approximate Riemann solver for multiphase Mie-Grüneisen flows. Attempts to form hybrid solvers through simple low-order smoothness measure-based blending of schemes have been made for conservative flux-splitting solvers [3, 68].

Presently, in order to address the above issues, a blending methodology based on a norm of the deviation of local smoothness dependent WENO-reconstruction weights has been developed [90]. In devising an effective limiter similarities between WENO and classical flux and slope limiter type

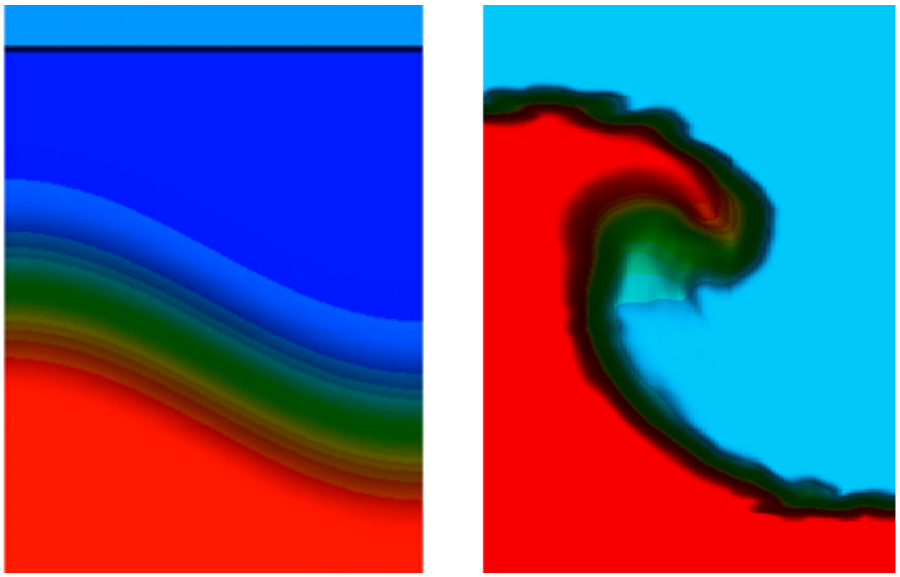

(a) (b)

Figure 3.1: MORB-molybdenum Mach 1.5 single cosine mode perturbation Richtmyer-Meshkov instability simulation by simple flux-splitting method exhibiting catastrophic oscillations. Initial density contour plot (a) and later time (b). The mixed phase region is spread over a large number of scales to demonstrate that the phenomenon is not grid scale generated. At later time the solution is polluted by oscillations driven by phase errors.

methods are exploited. Doing so yields a generalized limiter useful for smoothly blending a lower-order upwinding Riemann solver and high-order center-difference scheme while maintaining high-order convergence for smooth flows. To first explore the properties of the new limiter methodology it is applied to the linear advection equation, building fourth and sixth-order schemes and providing comparison to standard third and fifth-order WENO methods [37, 79]. A detailed description of a spatially fourth-order finite-difference patch-solver for the multiphase Euler equations with special consideration for the Mie-Grüneisen equation of state is then explored. The implementation combines spatially fourth-order skew-symmetric kinetic-energy preserving center-difference and a second-order WENO Roe-Riemann approach. Hybridization is achieved for the solver through Lax-entropy conditions and gradient tolerances. The scheme is then initially demonstrated for solids modeled by isotropic Mie-Grüneisen equations of state in one dimension. This is followed up by applying the methodology in two dimensions with adaptive mesh refinement capabilities utilizing the California Institute of Technology's VTF AMROC software [15].

3.1 Hybrid limiter methodology

Hyperbolic conservation laws typically describe material behavior containing discontinuities and smooth regions, two features best addressed by different numerical schemes. At discontinuities a

low-order upwinding scheme is ideal for preventing oscillations. Alternatively, in smooth regions of the solution a low dissipation method, often in the form of a centered difference scheme, is advantageous [3, 29, 68]. However, applying different schemes directly to different regions can lead to oscillations in regions where schemes meet if their dispersion relations are not suitably well matched [29]. To avoid this difficulty, it is important that the stencil associated with one of the schemes tends toward the others in regions where the schemes will meet. Additionally, flows with mixtures of real materials modeled by Mie-Grüneisen equations of state can develop disastrous oscillations when treated numerically by a conservative flux-splitting numerical scheme [2]. A generalized limiter approach presents a way to address the above issues simultaneously. In practice the success depends heavily on how the limiter is defined. Typically the limiter is based on a measure of smoothness locally. In reality it is difficult to achieve the desired result of the limiter method completely reducing to the desired stencil. For this reason a separate set of criteria resulting in a sharp cutoff filtering of the limiter is of practical use. In effect, all hybrid schemes may be formulated as limiter schemes with sharp cutoff filtering of the limiter.

3.1.1 Limiter methodology

The Lax-Wendroff theorem [45, 46, 86] indicates proper weak solution convergence for hyperbolic conservation laws can be obtained sufficiently by using a numerical scheme that maintains conservation of certain variables. A practical approach to creating such a conservative scheme is to define flux derivatives by a symmetric difference of midpoint reconstructions $\hat{f}_{j\pm1/2}$ of order at least $k-2$,

$$\frac{\partial f}{\partial x} = \frac{\hat{f}_{j+1/2} - \hat{f}_{j-1/2}}{\Delta x} + O(\Delta x^k). \tag{3.1}$$

Although primitive quantities are not conserved, the above methodology can be applied uniformly in approximating all derivatives. Practical application of (3.1) then only requires a midpoint reconstruction of quantities of interest, namely fluxes and primitives such as pressure and velocity.

A blending of multiple reconstruction schemes is appealing for achieving different stencils for sharp and smooth features:

$$\hat{f}_{j+1/2} = \hat{f}^k_{j+1/2} + \Phi(\hat{f}^r_{j+1/2} - \hat{f}^k_{j+1/2}). \tag{3.2}$$

Here Φ is a limiter used to achieve the desired blend of $\hat{f}^r_{j+1/2}$ and $\hat{f}^k_{j+1/2}$, rth- and kth-order midpoint reconstructions, respectively. Typically $\hat{f}^r_{j+1/2}$ is a low-order upwinding scheme and $\hat{f}^k_{j+1/2}$ is a higher-order method with less dissipation ($k > r$). It is therefore desirable that Φ approaches unity at discontinuities and tends toward zero in smooth regions. Furthermore, in order to maintain kth-order global convergence when a smooth solution is present, it is important to use a limiter with

the property that

$$\Phi \propto \Delta x^{\beta}, \quad \beta \geq k - r. \tag{3.3}$$

Defining a good limiter of practical use is a complicated matter [45, 46, 86]. In the following section a structured way to define a practical limiter for a kth-order scheme based on WENO weights is presented.

3.1.2 WENO-weight-inspired limiters

Weighted essentially non-oscillatory (WENO) schemes represent a popular subcategory of solvers for hyperbolic partial differential equations [37, 48, 79]. At a basic level of interpretation WENO is merely polynomial interpolation by weighted hierarchy. For practical application to numerical methods on evenly spaced Cartesian grid points, WENO focuses on the reconstruction of midpoint values, forming a weighted combination of r first-order sub-stencil interpolations q_k^r that tend toward an order $2r-1$ approximation q_{r-1}^{2r-1} of function f at $x = (j+1/2)\Delta x$ in smooth regions:

$$\begin{aligned} f_{j+1/2} &= q_{r-1}^{2r-1}(f_{j-r+1}, \ldots, f_{j+r-1}) \\ &\quad + \sum_{k=0}^{r-1} (w_k - C_k^r) q_k^r (f_{j+k-r+1}, \ldots, f_{j+k}) \\ &= \sum_{k=0}^{r-1} w_k q_k^r (f_{j+k-r+1}, \ldots, f_{j+k}). \end{aligned} \tag{3.4}$$

Here C_k represent ideal sub-stencil weighting and w_k are variable weights dependent on local solution character. The above reflects a slope-limiter-like approach to the reconstruction of midpoint values. Although not directly in slope limiter form, it is not to difficult to design weights that yield classic slope limiter or even ENO methods. More commonly weights are defined systematically by

$$w_k = \frac{\alpha_k}{\sum_{j=0}^{r-1} \alpha_j}, \tag{3.5}$$

$$\alpha_k = \frac{C_k^r}{(\epsilon + IS_k)^p}, \quad k = 0, 1, \ldots, r-1, \tag{3.6}$$

where IS_k is a sub-stencil smoothness measure, p and ϵ are chosen constants, and C_k^r is the desired sub-stencil weight in smooth solution regions [37].

Noting that slope and flux limiter approaches are equivalent, it is instructive to re-arrange (3.4) in a flux-limiter-like form

$$\begin{aligned} f_{j+1/2} &= q_{r-1}^{2r-1}(f_{j-r+1},\ldots,f_{j+r-1}) \\ &+ \sum_{k=0}^{r-2} \phi_k q_k^r(f_{j+k-r+1},\ldots,f_{j+k}) \\ &- \sum_{k=0}^{r-2} \phi_k q_{r-1}^{2r-1}(f_{j-r+1},\ldots,f_{j+r-1}). \end{aligned} \tag{3.7}$$

A matrix relationship exists relating the flux limiters ϕ_k and classic WENO weights w_k,

$$\underline{\underline{A}}(\underline{C}^r)\cdot\underline{\phi} = \underline{w} - \underline{C}^r. \tag{3.8}$$

Taking a norm of the above yields a single generalized limiter,

$$\Phi = \| A \|_p \, \|\underline{w} - \underline{C}^r\|_p. \tag{3.9}$$

It is not surprising that the limiter norm is directly proportional to a norm of the deviation of weights from ideal. Equation (3.9) provides a generalized robust way for defining a limiter for high-order schemes.

3.2 High-order implementation

3.2.1 Linear advection equation solver

To demonstrate application of equation (3.9) the methodology is first applied to the linear advection equation,

$$\frac{\partial u}{\partial t} + \frac{\partial u}{\partial x} = 0, \tag{3.10}$$

creating spatially fourth and sixth-order schemes based on high-order center-differences and WENO reconstruction Riemann solvers.

In constructing a fourth-order method a standard fourth-order center-difference is utilized,

$$\hat{u}_{j+1/2}^{CD4} = -\frac{1}{12}(u_{j+2}+u_{j-1}) + \frac{5}{12}(u_j + u_{j+1}), \tag{3.11}$$

combined by limiter with a third-order WENO scheme $\hat{u}_{j+1/2}^{WENO3}$ [48],

$$\hat{u}_{j+1/2} = \hat{u}_{j+1/2}^{CD4} + \Phi(\hat{u}_{j+1/2}^{WENO3} - \hat{u}_{j+1/2}^{CD4}), \tag{3.12}$$

where the limiter is defined by,

$$\Phi = \|\underline{w} - \underline{C}^r\|_2. \tag{3.13}$$

Standard fifth-order WENO weights with $r = 3$ and preferred stencil coefficients $C_0^3 = 1/10$,$C_1^3 = 6/10$, $C_2^3 = 3/10$ is utilized for evaluating the deviation norm of equation (3.13). In determining the weights, the method described in [37] is followed with $\epsilon = 10^{-6}$, $p = 2$ and smoothness measures

$$\begin{aligned} IS_0 &= \frac{13}{12}(u_{j-2} - 2u_{j-1} + u_j)^2 + \frac{1}{4}(u_{j-2} - 4u_{j-1} + 3u_j)^2, \\ IS_1 &= \frac{13}{12}(u_{j-1} - 2u_j + u_{j+1})^2 + \frac{1}{4}(u_{j-1} - u_{j+1})^2, \\ IS_2 &= \frac{13}{12}(u_j - 2u_{j+1} + u_{j+2})^2 + \frac{1}{4}(3u_j - 4u_{j+1} + 3u_{j+2})^2. \end{aligned} \tag{3.14}$$

Likewise, in constructing a sixth-order scheme the center-difference

$$\hat{u}_{j+1/2}^{CD6} = \frac{1}{60}(u_{j+3} + u_{j-2}) - \frac{2}{15}(u_{j+2} + u_{j-1}) + \frac{37}{60}(u_{j+1} + u_j) \tag{3.15}$$

is applied and combined by limiter with a fifth-order WENO method $\hat{u}_{j+1/2}^{WENO5}$ [37],

$$\hat{u}_{j+1/2} = \hat{u}_{j+1/2}^{CD6} + \Phi(\hat{u}_{j+1/2}^{WENO5} - \hat{u}_{j+1/2}^{CD6}). \tag{3.16}$$

It is possible to combine sixth-order center-difference with third-order WENO scheme and still achieve sixth-order convergence for smooth solutions. However, doing so results in higher dissipation at discontinuities. To construct Φ for the present sixth-order method from equation (3.9) the seventh-order WENO preferred stencil coefficients and smoothness indicators with $p = 5$, for which the equations are omitted and can be found in their original source [6], is used.

To form a complete numerical scheme from the above spatial discretization a temporal discretization is then required. For testing purposes, fourth-order strong-stability-preserving Runge-Kutta (SSP RK-4) temporal discretization [24] is applied,

$$\begin{aligned} q^{(1)} &= q^n + \frac{1}{2}\Delta t L(q^n), \\ q^{(2)} &= q^n + \frac{1}{2}\Delta t L(q^{(1)}), \\ q^{(3)} &= q^n + \Delta t L(q^{(2)}), \\ q^{n+1} &= \frac{1}{3}(-q^n + q^{(1)} + 2q^{(2)} + q^{(3)}) + \frac{1}{6}\Delta t L(q^{(3)}), \end{aligned} \tag{3.17}$$

3.2.2 Test problems

For the purposes of comparison the previously described fourth- and sixth-order methods, as well as third- and fifth-order WENO methods, are applied to the linear advection equation in a periodic domain $-1 \leq x \leq 1$ with initial conditions

$$u(x, t = 0) = \begin{cases} 1, & -3/4 < x < -1/4 \\ e^{-300(x-0.5)^2}, & \text{otherwise.} \end{cases} \tag{3.18}$$

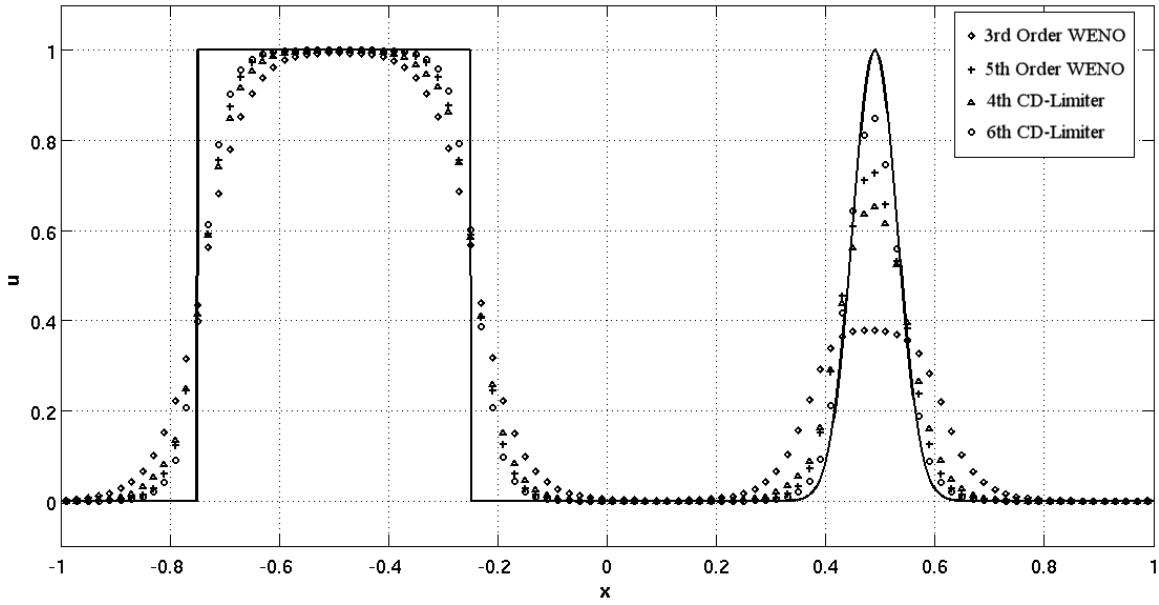

Figure 3.2: Numerical solutions to the linear advection equation in a periodic domain achieved with spatially third and fifth-order WENO, present fourth and sixth-order WENO-inspired limiter methods, denoted by diamonds and crosses, triangles and circles, respectively. Solution depicted at 2000th time step, $CFL = 0.5$ and $n = 100$.

Numerical solutions are shown at the $2000th$ time step in Figure 3.2 for simulation with $n = 100$ points and $CFL = 0.5$. The present sixth-order scheme best captures the solution, retaining the Gaussian's peak with greater fidelity and having a slightly sharper approximation to the square wave. Third-order WENO displays a heavily diffuse approximation to the square wave while the sixth-order method remains the sharpest.

Table 3.1: Square wave L_2 error norm and convergence order for $t = 2$ and $CFL = 0.9$.

	third-order	WENO	*fifth*-order	WENO	*fourth*-order	limiter	*sixth*-order	limiter
N	L_2 error	L_2 order	L_2 error	L_2 order	L_2 error	L_2 order	L_2 error	L_2 order
40	0.218306	-	0.189875	-	0.195927	-	0.180998	-
80	0.171496	0.348180	0.143627	0.402720	0.149808	0.387200	0.134949	0.423568
120	0.148070	0.362235	0.122103	0.400422	0.127423	0.399164	0.113716	0.422196
160	0.133336	0.364332	0.108706	0.403973	0.113588	0.399497	0.100573	0.426928
200	0.122895	0.365437	0.099287	0.406142	0.103838	0.402224	0.091383	0.429473

For smooth solutions the convergence rate is simply the order of the method. For hyperbolic partial differential equations, convergence to weak solutions is of primary interest. To better compare the schemes a spatial convergence study is next presented for a square wave in a periodic domain. The L_2 error norm, defined by

$$L_2 = \Big(\sum_{i=1}^{n} \frac{(u_i - u_i^e)^2}{n} \Big)^{1/2}, \tag{3.19}$$

and its convergence rate are given in Table 3.1. To ensure spatial errors are the dominant contri-

bution, for fifth-order WENO the time step taken is scaled to $\Delta t = \left(CFL \times \Delta x\right)^{5/4}$ and for the sixth-order method $\Delta t = \left(CFL \times \Delta x\right)^{3/2}$. For a simple first order upwinding scheme applied to the linear advection equation with a single step discontinuity the L_1 error is expected to converge as $O(\Delta x^{1/2})$ [45]. Additionally, even for spatially higher-order methods, it has been demonstrated that the L_1 error norm in smooth solution regions upwind of discontinuities will converge as $O(\Delta x)$ [20]. It is therefore reasonable to expect the L_1 error norm for a method of any order to behave as $O(\Delta x^p)$ with $1/2 \leq p < 1$. Presently, the L_2 error norm is examined, which represents a stronger measure of the affect of discontinuities on convergence. The L_1 norm can be bound in terms of the L_2 norm by

$$L_2 \leq L_1 \leq \sqrt{n} L_2. \tag{3.20}$$

The $\sqrt{n}$ can term in this inequality can be interpreted as $\Delta x^{-1/2}$. Therefore, for solutions with discontinuities, the convergence rate of the L_2 error norm is expected to be less than that of the L_1 error norm by as much as $1/2$. As is then expected, the current results yield L_2 error norm convergence rates of less than a half. The present sixth-order method demonstrates a slightly higher L_2 convergence rate to the weak solution then the others. The currently proposed fourth-order method demonstrates roughly the same convergence rate as that of fifth-order WENO, likely due to the limiter being based on fifth-order WENO weights.

3.2.3 Hybrid multiphase Euler solver for Mie-Grüneisen fluids

In the following sections a dimensionally unsplit, spatially fourth-order, cartesian mesh patch solver implementation of a WENO weight limiter-based hybrid scheme for multiphase flows with Mie-Grüneisen equations of state is presented. Classic fourth-order, center-difference in a skew-symmetric formulation of the energy and momentum equations is used for the ideal stencil [65]. For the low-order upwinding solver a third-order WENO reconstruction of primitives coupled with a Roe approximate Riemann solver is applied [81]. The limiter used is calculated from WENO weights associated with a fifth-order flux splitting approach [37]. Temporal discretization is performed by total variation diminishing third-order Runge-Kutta (TVD-RK3). Hybridization is achieved through a Lax-entropy- and gradient-tolerance-based switching criteria [49, 65]. The California Institute of Technology's VTF AMROC [15] software is used to apply this patch solver in up to two dimensions with AMR capability.

3.2.3.1 Euler compressible flow equations

The Euler equations of multicomponent compressible fluid mechanics model a very specific subgroup of flows of interest. Under the assumptions made, fluid motion is described by a set of coupled

conservative hyperbolic partial differential equations

$$\frac{\partial \mathbf{q}}{\partial t} + \frac{\partial \mathbf{F}(\mathbf{q})}{\partial x} + \frac{\partial \mathbf{G}(\mathbf{q})}{\partial y} + \frac{\partial \mathbf{H}(\mathbf{q})}{\partial z} = 0, \tag{3.21}$$

where the directional fluxes F, G, and H are given by

$$\mathbf{F}(\mathbf{q}) = \begin{pmatrix} \rho u \\ \rho u^2 + p \\ \rho uv \\ \rho uw \\ u(\rho E + p) \\ \rho u\psi_1 \\ \vdots \\ \rho u\psi_{n-1} \end{pmatrix}, \mathbf{G}(\mathbf{q}) = \begin{pmatrix} \rho v \\ \rho vu \\ \rho v^2 + p \\ \rho vw \\ v(\rho E + p) \\ \rho v\psi_1 \\ \vdots \\ \rho v\psi_{n-1} \end{pmatrix}, \mathbf{H}(\mathbf{q}) = \begin{pmatrix} \rho w \\ \rho wu \\ \rho wv \\ \rho w^2 + p \\ w(\rho E + p) \\ \rho w\psi_1 \\ \vdots \\ \rho w\psi_{n-1} \end{pmatrix}, \tag{3.22}$$

with conserved vector of state $\mathbf{q}$ defined by

$$\mathbf{q} = (\rho, \rho u, \rho v, \rho w, \rho E, \rho\psi_1, \ldots, \rho\psi_{n-1}). \tag{3.23}$$

Here $E = e + \frac{1}{2}(u^2 + v^2 + w^2)$ is the energy per unit mass and ψ_j represents a scalar quantity of interest associated with the flows jth component. In practice it is useful to track either the scalar mass fraction or a level-set associated with each component.

3.2.3.2 Preventing pressure oscillations in mixtures

An important fundamental subset of solutions to the Euler equations are those for which pressure and velocity are constant for all time, such as the translation of a pressure matched material interface. Any solver of practical use should be able to maintain such conditions to within an acceptable tolerance after each temporal advance of the solution. Simple flux-splitting schemes do not in general meet such requirements for some material models. Designing a scheme that does so for multicomponent flows is not trivial [2]. In practice the degree to which the integrity of such solutions is compromised varies with the material models. For perfect gases with similar specific heat ratios the degradation may be slow enough to neglect for some flows of interest. However, this is not the case in general, particularly for flows involving multiple materials modeled by Mie-Grüneisen equations of state, as is demonstrated in Figure 3.1 using a flux-splitting WENO method. In addressing the issue here the approach of Shyue [81] is followed, tracking three additional functions of density related to the Mie-Grüneisen equation of state for the mixture and re-writing the scalar equation in primitive

form

$$\begin{array}{rcrcl} \frac{\partial}{\partial t}\left(\frac{1}{\Gamma_{_H}}\right) & + & \mathbf{u}\cdot\nabla\left(\frac{1}{\Gamma_{_H}}\right) & = & -\rho\chi_{\Gamma_{_H}}\nabla\cdot\mathbf{u}, \\ \frac{\partial}{\partial t}\left(\frac{p_{_H}}{\Gamma_{_H}}\right) & + & \mathbf{u},\cdot\nabla\left(\frac{p_{_H}}{\Gamma_{_H}}\right) & = & -\rho\chi_{p_{_H}}\nabla\cdot\mathbf{u}, \\ \frac{\partial}{\partial t}(\rho e_{_H}) & + & \mathbf{u}\cdot\nabla(\rho e_{_H}) & = & -\rho\chi_{e_{_H}}\nabla\cdot\mathbf{u}, \\ \frac{\partial\psi_j}{\partial t} & + & \mathbf{u}\cdot\nabla(\psi_j) & = & 0, \quad (j=1,2,\ldots,n-1), \end{array} \tag{3.24}$$

where

$$\chi_{\Gamma_{_H}} = -\Gamma'_{_H}/{\Gamma_{_H}}^2, \tag{3.25}$$

$$\chi_{p_{_H}} = (\Gamma_{_H}p'_{_H} - \Gamma'_{_H}p_{_H})/{\Gamma_{_H}}^2, \tag{3.26}$$

$$\chi_{e_{_H}} = e_{_H} + \rho e'_{_H}, \tag{3.27}$$

$$\tag{3.28}$$

and prime quantities indicate derivative with respect to density: for example,

$$\Gamma'_{_H} = \frac{d\Gamma_{_H}}{d\rho}. \tag{3.29}$$

The new vector of state of interest is then

$$\mathbf{q} = (\rho, \rho u, \rho v, \rho w, \rho E, 1/\Gamma_{_H}, p_{_H}/\Gamma_{_H}, \rho e_{_H}, \psi_1, \ldots, \psi_{n-1}). \tag{3.30}$$

Pressure can be obtained directly from the vector of state by the relationship

$$p = \left(\rho E - \frac{(\rho u)^2 + (\rho v)^2 + (\rho w)^2}{2\rho} + \frac{p_{_H}}{\Gamma_{_H}} - \rho e_{_H}\right)\Big/\left(\frac{1}{\Gamma_{_H}}\right) \tag{3.31}$$

and likewise the speed of sound is defined by

$$\begin{array}{rcl} c^2 & = & \frac{\partial p}{\partial\rho}\Big|_s = \frac{\partial p}{\partial\rho}\Big|_e + \frac{p}{\rho^2}\frac{\partial p}{\partial e}\Big|_\rho \\ & = & \Gamma_{_H}(e + p/\rho + \chi_{p_{_H}} - \chi_{e_{_H}} - p\chi_{\Gamma_{_H}}). \end{array} \tag{3.32}$$

The reasoning behind this choice of additional parameters can be better understood by considering how pressure evolves [81]. For constant pressure translation problems in one dimension the equations of motion reduce to simple forms of conservation of mass and energy,

$$\begin{array}{rcrcl} \frac{\partial\rho}{\partial t} & + & u\frac{\partial\rho}{\partial t} & = & 0 \\ \frac{\partial(\rho e)}{\partial t} & + & u\frac{\partial(\rho e)}{\partial t} & = & 0. \end{array} \tag{3.33}$$

Upon substituting the internal energy form of the Mie-Grüneisen equation of state into the second

equation a pressure evolution equation is obtained,

$$\frac{\partial}{\partial t}\Big(\frac{p-p_{_H}(\rho)}{\Gamma_{_H}(\rho)+\rho e_{_H}(\rho)}\Big) \quad + \quad u\frac{\partial}{\partial t}\Big(\frac{p-p_{_H}(\rho)}{\Gamma_{_H}(\rho)}+\rho e_{_H}(\rho)\Big) \quad = \quad 0. \tag{3.34}$$

From this equation it is clear that the density dependent functions $1/\Gamma_{_H}$, $p_{_H}/\Gamma_{_H}$, and $\rho e_{_H}$ are fundamental to maintaining constant pressure translational solutions. It is not necessary to track these quantities individually, however, doing so reduces the number of Hugoniot function evaluations required [81].

3.2.3.3 Center difference

For a fourth-order, center-difference scheme, a kinetic-energy-preserving skew-symmetric reconstruction of quantities is used [58, 65]. To achieve this the end product of the difference of midpoint reconstructions must be consistent with skew-symmetric form of the momentum and energy equations,

$$\frac{\partial(\rho uv)}{\partial x} = \frac{1}{2}\frac{\partial(\rho uv)}{\partial x} + \frac{1}{2}\rho u\frac{\partial v}{\partial x} + \frac{1}{2}v\frac{\partial(\rho u)}{\partial x}, \tag{3.35}$$

$$\frac{\partial(\rho E+p)u}{\partial x} = \frac{1}{2}\frac{\partial(\rho eu)}{\partial x} + \frac{1}{2}\rho u\frac{\partial e}{\partial x} + \frac{1}{2}e\frac{\partial(\rho u)}{\partial x} + \frac{1}{2}u\frac{\partial(\rho uv)}{\partial x} + \frac{1}{2}\rho uv\frac{\partial u}{\partial x} + u\frac{\partial p}{\partial x} + p\frac{\partial u}{\partial x}. \tag{3.36}$$

Therefore, for product quantities in the above skew-symmetric equations, define their midpoint reconstruction by

$$\hat{fg}^{skew}_{j+1/2} = \frac{1}{2}(\hat{fg}^{div}_{j+1/2} + \hat{fg}^{prod}_{j+1/2}) \tag{3.37}$$

where

$$\hat{f}^{div}_{j+1/2} = \alpha(f_{j+2}+f_{j-1}) + (\alpha+\beta)(f_j+f_{j+1}) \tag{3.38}$$

and

$$\begin{aligned} \hat{fg}^{prod}_{j+1/2} \quad &= \quad \beta(f_jg_{j+1}+f_{j+1}g_j) \\ &\quad +\alpha(f_{j+2}g_j+f_{j-1}g_{j+1}+f_jg_{j+2}+f_{j+1}b_{j-1}). \end{aligned} \tag{3.39}$$

All other quantities are reconstructed by the simple divergence formulation of (3.38). The choice of $\beta = 1/2 - 2\alpha$ and $\alpha = -1/12$ leads to fourth-order finite differences. Alternatively, Hill and Pullin [29] have optimized β and α for the purpose of minimizing dissipation of turbulent kinetic energy over a spectrum of scales for application with an explicit turbulence model.

3.2.3.4 WENO-Roe solver

Riemann solvers represent a popular subset of upwinding numerical methods for hyperbolic partial differential equations. The basic idea behind such solvers is to reconstruct midpoint fluxes through solution to a Riemann problem between biased interpolations of left and right states. In general, for nonlinear equations such as the Euler equations, solution to Riemann problems are complex and can

only be solved numerically at great expense. Linearization of the Riemann problem therefore presents an attractive alternative for providing quick approximate solutions. However, producing a robust and meaningful linearization is not a straightforward task. For perfect gases Roe's approximate Riemann solver [72] provides a meaningful way to linearize the Riemann problem. Extension of the methodology for more general materials, such as metals described by Mie-Grüneisen equations of state, is not necessarily achievable analytically. Despite this drawback, a Roe-like linearization remains useful, retaining a moderate level of robustness while reducing the overall cost associated with solving the Riemann problem [80, 81]. In light of this, the approach to reconstructing midpoint quantities is as follows: First, apply a third-order single dimension WENO interpolation of primitives,

$$\mathbf{u} = (\rho, u, v, w, p, \Gamma_{_H}, p_{_H}, e_{_H}, \psi_1, \ldots, \psi_{n-1}), \tag{3.40}$$

to form left and right states $\mathbf{q_L}$ and $\mathbf{q_R}$. Then, following the approach of [81], the zero characteristic quantities associated with the Riemann problem is approximated by Roe linearization. The process is described in the remainder of this section in detail.

Linearization of the Riemann problem associated with a conservative hyperbolic partial differential equation is most easily achieved by considering the nonconservative form. For the multicomponent Euler equations,

$$\frac{\partial \mathbf{q}}{\partial t} + \mathbf{A}_{_F}(\mathbf{q})\frac{\partial \mathbf{q}}{\partial x} + \mathbf{A}_{_G}(\mathbf{q})\frac{\partial \mathbf{q}}{\partial y} + \mathbf{A}_{_H}(\mathbf{q})\frac{\partial \mathbf{q}}{\partial z} = 0, \tag{3.41}$$

where $\mathbf{A}_{_F}(\mathbf{q})$, $\mathbf{A}_{_G}(\mathbf{q})$, $\mathbf{A}_{_H}(\mathbf{q})$ are the Jacobian matrices defined by

$$\mathbf{A}_{_F}(\mathbf{q}) = \frac{\partial \mathbf{F}(\mathbf{q})}{\partial \mathbf{q}}, \mathbf{A}_{_G}(\mathbf{q}) = \frac{\partial \mathbf{G}(\mathbf{q})}{\partial \mathbf{q}}, \mathbf{A}_{_H}(\mathbf{q}) = \frac{\partial \mathbf{H}(\mathbf{q})}{\partial \mathbf{q}}. \tag{3.42}$$

Let $K = \Gamma(u^2 + v^2 + w^2)/2$ and $H = E + p/\rho$, the enthalpy per unit mass. The Jacobian of $\mathbf{F}(\mathbf{q})$ is then given by

$$\mathbf{A}_{_F}(\mathbf{q}) = \begin{bmatrix} 0 & 1 & 0 & 0 & 0 & 0 & 0 & 0 & 0 & \dots & 0 \\ K-u^2 & u(2-\Gamma) & -v\Gamma & -w\Gamma & \Gamma & -p\Gamma & \Gamma & -\Gamma & 0 & \dots & 0 \\ -uv & v & u & 0 & 0 & 0 & 0 & 0 & 0 & \dots & 0 \\ -uw & w & 0 & u & 0 & 0 & 0 & 0 & 0 & \dots & 0 \\ u(K-H) & H-u^2\Gamma & -uv\Gamma & -uw\Gamma & u(\Gamma+1) & -up\Gamma & u\Gamma & -u\Gamma & 0 & \dots & 0 \\ -u\chi_{\Gamma_H} & \chi_{\Gamma_H} & 0 & 0 & 0 & u & 0 & 0 & 0 & \dots & 0 \\ -u\chi_{p_H} & \chi_{p_H} & 0 & 0 & 0 & 0 & u & 0 & 0 & \dots & 0 \\ -u\chi_{e_H} & \chi_{e_H} & 0 & 0 & 0 & 0 & 0 & u & 0 & \dots & 0 \\ 0 & 0 & 0 & 0 & 0 & 0 & 0 & 0 & u & \dots & 0 \\ \vdots & \vdots & \vdots & \vdots & \vdots & \vdots & \vdots & \vdots & \vdots & \ddots & \vdots \\ 0 & 0 & 0 & 0 & 0 & 0 & 0 & 0 & 0 & \dots & u \end{bmatrix}. \tag{3.43}$$

The right eigenvectors associated with this Jacobian matrix are

$$\mathbf{R}_{_F}(\mathbf{q}) = \begin{bmatrix} 1 & 1 & 1 & 0 & 0 & 0 & 0 & 0 & 0 & \dots & 0 \\ u-c & u & u+c & 0 & 0 & 0 & 0 & 0 & 0 & \dots & 0 \\ v & v & v & 1 & 0 & 0 & 0 & 0 & 0 & \dots & 0 \\ w & w & w & 0 & 1 & 0 & 0 & 0 & 0 & \dots & 0 \\ H-uc & K/\Gamma & H+uc & v & w & p & -1 & 1 & \dots & 0 & \\ \chi_{\Gamma_H} & 0 & \chi_{\Gamma_H} & 0 & 0 & 1 & 0 & 0 & 0 & \dots & 0 \\ \chi_{p_H} & 0 & \chi_{p_H} & 0 & 0 & 0 & 1 & 0 & 0 & \dots & 0 \\ \chi_{e_H} & 0 & \chi_{e_H} & 0 & 0 & 0 & 0 & 1 & 0 & \dots & 0 \\ 0 & 0 & 0 & 0 & 0 & 0 & 0 & 0 & 1 & \dots & 0 \\ \vdots & \vdots & \vdots & \vdots & \vdots & \vdots & \vdots & \vdots & \vdots & \ddots & \vdots \\ 0 & 0 & 0 & 0 & 0 & 0 & 0 & 0 & 0 & \dots & 1 \end{bmatrix}, \tag{3.44}$$

and the corresponding eigenvalues are

$$\Lambda = diag(u-c, u, u+c, u, u, u, u, u, u, \dots, u). \tag{3.45}$$

The Jacobian matrices and associated right eigenvectors of $\mathbf{G}(\mathbf{q})$ and $\mathbf{H}(\mathbf{q})$ can be obtained by simple permutations of velocity components.

In approximating the solution to the Riemann problem between states $\mathbf{q}_{\mathbf{L}}$ and $\mathbf{q}_{\mathbf{R}}$ Roe [72] lin-

earized the Jacobian, eigenvectors, and eigenvalues by a weighted average of fundamental quantities:

$$\hat{x} = \frac{\sqrt{\rho_L}x_L + \sqrt{\rho_R}x_R}{\sqrt{\rho_L} + \sqrt{\rho_R}}. \tag{3.46}$$

Shyue [81] has adapted Roe's linearization for application to multiphase flows with Mie-Grüneisen equations of state. Presently, Shyue's adaptation of Roe's solver is applied. The details needed for finding the approximate midpoint value for flux reconstruction is next described in detail.

For linear equations the solution of a Riemann problem consists of a series of discontinuous jumps across characteristic waves propagating at the rate of their eigenvalues λ. In practice the magnitude of the jumps can be determined by requiring conservation across all characteristic waves,

$$\begin{aligned} \mathbf{R}\alpha &= q_R - q_L \\ &= \Delta q. \end{aligned} \tag{3.47}$$

The approximate zero-characteristic state needed for obtaining midpoint quantities of interest is then

$$q^* = q_R - \mathbf{R^{-1}}\alpha^+ \tag{3.48}$$

$$= q_L + \mathbf{R^{-1}}\alpha^-, \tag{3.49}$$

where

$$\alpha_j^+ = \begin{cases} \alpha_j & \text{if } \lambda_j > 0 \\ 0 & \text{otherwise} \end{cases} \tag{3.50}$$

and

$$\alpha^- = \alpha - \alpha^+. \tag{3.51}$$

3.2.3.5 Limiter

It is not necessary to use the matrix norm $\| A \|_p$ in (3.9) explicitly. A constant of proportionality is acceptable,

$$\Phi_j = B\|\underline{w}_j - \underline{C}^r\|_p. \tag{3.52}$$

Here the value $p = 2$ is taken, corresponding to the L_2 norm. It is of practical interest to limit the range of possible values of Φ,

$$\Phi_{min} \leq \Phi_j \leq \Phi_{max}. \tag{3.53}$$

The values of Φ_{min} and Φ_{max} should be chosen congruently with the constant of proportionality B in order to give the desired amount of dissipation. Too large a value of B will push the limiter

beyond Φ_{max}, voiding any possibility of retaining the desired convergence rate in smooth flows. Generally $B \sim 1$ is typically adequate for maintaining $0 \leq \Phi_j \leq 1$. The upwinding scheme used along with shock strength and the equation of state are all contributing factors to the appropriate determination of a practical Φ_{max}.

In evaluating the deviation norm in equation (3.52), the fifth-order WENO weights are again used in equation(3.14). Density is the single variable by which smoothness is measured, which is generally robust, except in the rare case of a constant density discontinuity. It is important to note that (3.14) contains an asymmetric odd number of points about the midpoint $j+1/2$. Therefore, if applied directly, solutions that should be symmetric under coordinate inversion would not sustain symmetry numerically. Limiter symmetry can be restored by noting that the above is actually Φ_J^+ and that a Φ_j^- also exists from a WENO reconstruction for the same midpoint based on $(j+1)-1/2$. Taking the mean $\Phi_j = \frac{1}{2}(\Phi_j^- + \Phi_j^+)$ then eliminates limiter asymmetry.

3.2.3.6 Temporal discretization

In terms of simplicity and cost effectiveness, explicit Runge-Kutta temporal discretization presents an ideal approach. Whereas upwinding methods generally remain stable with simple first-order explicit time stepping when applied to hyperbolic partial differential equations, center-difference schemes require additional consideration for stability. Third-order or higher temporal discretization is in fact necessary [65]. Currently used is the storage efficient third-order total variation diminishing (TVD) Runge-Kutta [24],

$$\begin{aligned} q^{(1)} &= q^n + \frac{1}{2}\Delta t L(q^n), \\ q^{(2)} &= \frac{3}{4}q^n + \frac{1}{4}q^{(1)} + \frac{1}{4}\Delta t L(q^{(1)}), \\ q^{n+1} &= \frac{1}{3}q^n + \frac{2}{3}q^{(2)} + \frac{1}{6}\Delta t L(q^{(3)}). \end{aligned} \tag{3.54}$$

3.2.3.7 Adaptive mesh refinement

The California Institute of Technology's VTF AMROC [15–17] software is used to extend the methodology for parallel AMR application. AMROC is based on the parallel block structured AMR algorithm of Berger and Oliger [9, 10]. The approach divides the domain into patches of various spatial resolutions, interpolating boundary conditions between levels. The same solver is applied to each patch while maintaining a constant spatial-to-temporal refinement ratio. Presently not addressed are complications associated with load balancing that can result when significant variation in numerical method cost lead to significant loss in parallel performance efficiency for certain problems. In this sense the scheme has not been optimized for parallel computations, but otherwise the simple parallel extension has been successful.

3.2.3.8 Hybrid switching criteria

In practice the limiter described in previous sections will rarely if ever be exactly zero, resulting in some upwinding. Furthermore, if applied uniformly in the domain, the computational cost would remain the same at each point even if the lower-order upwinding scheme is barely used and not truly necessary. Since the center-difference scheme is cheap computationally relative to the upwinding Roe-Riemann solver, overall code efficiency can be improved by only applying the limiter method to regions identified to contain discontinuities. A variety of approaches for flagging regions with discontinuities have been developed in the hybrid scheme literature [29, 65]. Here a Lax-entropy-based approach for detecting shocks [49] is applied to determine if entropy gradients are aligned with pressure gradients typical of compressive shocks,

$$\left(\frac{(\rho u)_{j+1} - (\rho u)_j}{\rho_{j+1} - \rho_j}\right) \quad (p_{j+1} - p_j) < 0, \tag{3.55}$$

with an additional Mach-divergence tolerance criteria,

$$\left|\frac{u_{j+1} - u_j}{c_0}\right| > tol. \tag{3.56}$$

Regions with sharp scalar gradients are flagged by a simple gradient tolerance,

$$\left|\psi_{j+1} - \psi_j\right| > tol. \tag{3.57}$$

Typically tolerance values are on the order of a percent, corresponding to waves slightly stronger than weak shocks and scalar variations larger than those treatable by a center-difference. The above provides a fairly robust set of criteria for flagging regions in need of upwinding. Occasionally a sharp gradient not associated with a shock or scalar quantity may be present. In such cases curvature based detection may be used [29, 65],

$$\frac{\left|q_{j+1} + q_{j-1} - 2q_j\right|}{\left|q_{j+1} + q_{j-1} + 2q_j\right|} > tol. \tag{3.58}$$

In general, determination of the best flagging criteria and associated tolerance value is solution- and scheme-dependent. To protect further against oscillations it is useful to flag several closest neighboring points. Additionally, when hybridization is applied in an adaptive-mesh context oscillations can occur at coarse-fine boundaries making it desirable to add dissipation locally by use of an upwinding method [65].

3.2.3.9 Carbuncle phenomenon

Structured grids can lead to carbuncle phenomena when strong, slow moving discontinuities aligned with a structured grid are present [18, 59, 69, 77]. The classic case of the carbuncle phenomena is observed for inviscid Mach 15.3 perfect gas flow around a cylinder. The source of the name carbuncle was taken from the nonphysical carbuncle-shaped bow shock achieved. Directional dissipation variation leading to grid induced instability is widely accepted as the source [77]. In perfect gases the phenomenon is associated with strong shocks. More generally, the problem is a result of strong grid aligned gradients in wave speeds. In multicomponent flows with exotic equations of state it might be expected that carbuncle phenomenon occur more readily.

For single-mode Mach 1.5 Richtmyer-Meshkov instability between mid-ocean ridge basalt (MORB) and molybdenum modeled by shock-Hugoniot Mie-Grüneisen equations of state, features indicative of a carbuncle phenomenon are present in the form of a notch at the spike tip (see Figure 3.3(a)). The simulation corresponds to a centerline single-mode cosine perturbation of a MORB-molybdenum contact with wavelength $\lambda = 0.5\ m$ and amplitude $h_0 = 0.05\ m$. Initially the states on either side of the contact are in mechanical equilibrium, corresponding to ρ_0, p_0, and e_0 given in Table 2.1. A Mach 1.5 shockwave travels downward through the MORB, eventually reaching the diffuse zone where it deposits vorticity and yields transmitted and reflected shocks. The simulation is performed in a frame of reference corresponding to zero velocity after post-shock-interface interaction when no interface perturbation is present.

A key characteristic of the carbuncle phenomenon is sensitivity to grid-flow alignment. To demonstrate that the feature observed in Figure 3.3(a) is nonphysical, a simulation with a 45 degree rotation of the flow with respect to the grid was performed. The results, seen in Figure 3.3(b), show an alleviation of the notch as well as a considerable change in the general shape of contours, indicating significant dependence of dissipation on grid orientation.

Presently, to produce a fix for the carbuncle phenomenon the approach of Sanders [77] is followed. For approximate linearized Riemann solvers the local directional dissipation matrix is given by

$$M = R|\Lambda|R^{-1}. \tag{3.59}$$

To correct the problem, Sanders [77] adjusts the eigenvalues Λ in (3.59) by an amount equal to the maximum local grid variation in wave speed

$$\eta^H_{i+1/2,j} = max(\eta_{i+1/2,j}, \eta_{i,j+1/2}, \eta_{i,j-1/2}, \eta_{i+1,j+1/2}, \eta_{i+1,j-1/2}), \tag{3.60}$$

where

$$\eta_{i+1/2,j} = \frac{1}{2}|c_{i,j} - c_{i+1,j}| + \frac{1}{2}|u_{i,j} - u_{i+1,j}|. \tag{3.61}$$

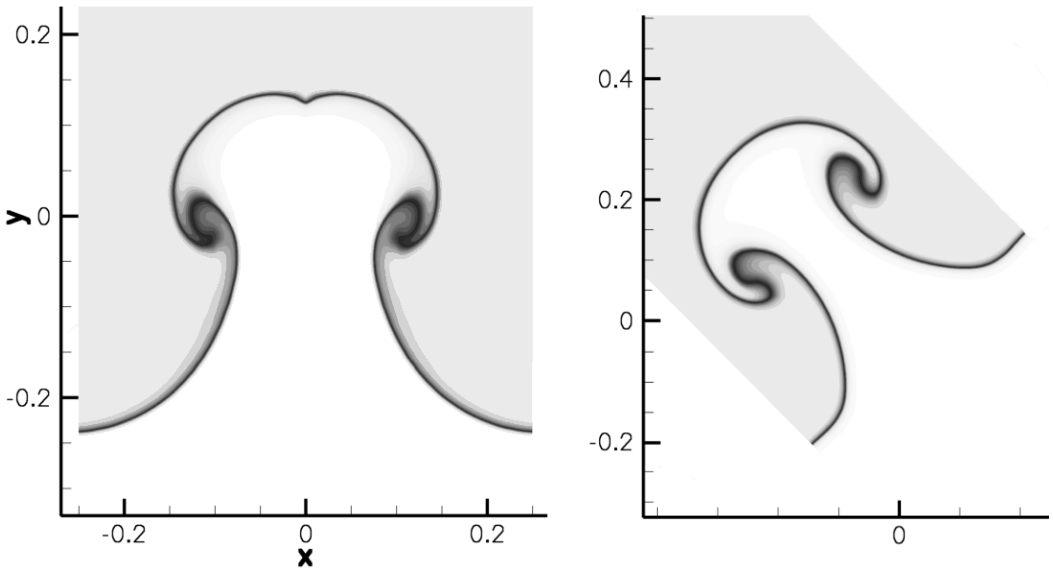

(a) (b)

Figure 3.3: MORB-molybdenum Mach 1.5 single-cosine-mode perturbation Richtmyer-Meshkov instability simulation results exhibiting carbuncle-like features ($t = 37\ ms$). (a) A nonphysical notch at the spike tip is visible. (b) Rotating the flow by 45 degrees with respect to the grid removes the notch.

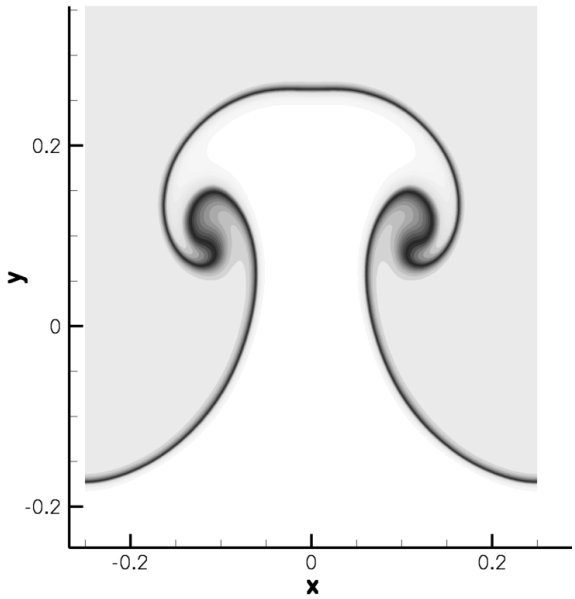

Figure 3.4: MORB-molybdenum Mach 1.5 single-cosine-mode perturbation Richtmyer-Meshkov instability simulation results with present H-correction for carbuncle implemented for $t = 37\ ms$. The carbuncle like notch observed in Figure 3.3 is smoothed over.

The corresponding added amount of dissipation is then

$$\frac{\eta^H_{i+1/2,j}\Delta q_{i+1/2,j} - \eta^H_{i-1/2,j}\Delta q_{i-1/2,j}}{\Delta x}, \tag{3.62}$$

where $\Delta q_j = q_{_R} - q_{_L}$ is the difference in biased stencil reconstructions [77]. The above correction works adequately at removing the notch observed in Figure 3.3 when applied with a low-order linear Riemann solver. However, the solver described currently is not a true linearization of the Euler equations since the blending of nonlinear center-difference and Riemann reconstruction has no definable corresponding left and right state or linearized Jacobian matrix $\hat{A}$. To address these issues a multidimensional H-correction to the limiter is applied,

$$\Phi^H_{i+1/2,j} = \Big(\Phi^2_{i+1/2,j} + max(\Phi^2_{i,j+1/2}, \Phi^2_{i,j-1/2}, \Phi^2_{i+1,j+1/2}, \Phi^2_{i+1,j-1/2})\Big)^{1/2}, \tag{3.63}$$

amplifying the limiter at sonic points with large wave speed variation,

$$\Phi^{H\prime}_{i+1/2,j} = \Big(\frac{\eta^H_{i+1/2,j}/|\lambda|^H_{max}}{|\lambda|^H_{min}/|\lambda|^H_{max} + \varepsilon}\Big)^{1/2}\Phi^H_{i+1/2,j}, \tag{3.64}$$

which promotes dissipation through the steepest parts of shock waves where the limiter often drops bellow the maximum, resulting is an undesirable region with low dissipation. Then added is an amount of dissipation equal to

$$\frac{\Phi^H_{i+1/2,j}\eta^H_{i+1/2,j}\Delta q_{i+1/2,j} - \Phi^H_{i-1/2,j}\eta^H_{i-1/2,j}\Delta q_{i-1/2,j}}{\Delta x}. \tag{3.65}$$

Doing so works reasonably well at mitigating the carbuncle-like notch (see Figure 3.4), but also yields a considerable increase in overall numerical dissipation.

3.2.4 One-dimensional test problems

3.2.4.1 Simple wave

First, to demonstrate how the limiter method behaves on its own, the method is presently applied without hybridization to a simple wave in a one-meter-long periodic slab of mid-ocean ridge basalt (MORB). The initial conditions are continuous and periodic in nature, corresponding to states in tension along the Murnaghan isentrope. For continuous initial conditions, the single-phase Euler equations in one dimension yield the solution [42]

$$u(\rho) = \pm \int \frac{c(\rho)}{\rho} d\rho \tag{3.66}$$

along characteristics defined in space and time from

$$x = t(u \pm c(u)) + f(u). \tag{3.67}$$

From these transcendental equations, a simple periodic single-mode wave solution for isentropes of a perfect gas can be found [42]. The solution is shown to become increasingly steep, resulting in the formation of shock waves. For metals described by Mie-Grüneisen equations of state with reference state curves given by a Hugoniot, an analytic equation for isentropes is not generally attainable. However, the use of a Murnaghan isentrope for extending the equation of state for expanded states provides a single isentrope in the form

$$p(\rho, s = s_0) = A\rho^{\alpha} + B. \tag{3.68}$$

Solution to the Euler equations for this isentrope in terms of velocity is then

$$u(\rho) = \frac{2\sqrt{\alpha A}}{\alpha - 1}\rho^{\frac{\alpha-1}{2}} + const. \tag{3.69}$$

For the initial conditions a simple sine wave for the initial velocity profile is taken,

$$\begin{aligned} u(x, t = 0) &= U_0 \sin(kx), \\ f(u) &= \tfrac{1}{k}\sin^{-1}(u/U), \end{aligned} \tag{3.70}$$

with $U_0 = 60.34\, m/s$, corresponding to a density variation of $2500.4 \leq \rho \leq 2659.7\ kg/m^3$. Simulation results are seen in Figure 3.5 and Figure 3.6 for $CFL = 0.95$ and $\Delta x = 0.01\ m$. For early times the limiter remains relatively small, yielding very little numerical dissipation. As the shockwave begins to form at the inflection point the limiter increases locally to introduce the desired character of the upwinding Roe solver, maintaining a relatively smooth solution.

For smooth solutions such as the simple wave before a shock forms, with the use of fourth-order SSP RK-4 temporal discretization, the numerical convergence rate of the presently described methodology should be fourth-order. To demonstrate the convergence rate an approximation to the L_2 error norm in density is calculated at $t = 0.5\ ms$ for various numbers of points while maintaining a fixed CFL of 0.95. Again, to isolate the numerical method this is done so without hybridization. The results of the study are given in Table 3.2. The convergence order is seen to be mesh-size dependent, asymptotically approaching the expected fourth-order rate of convergence as the number of points increases.

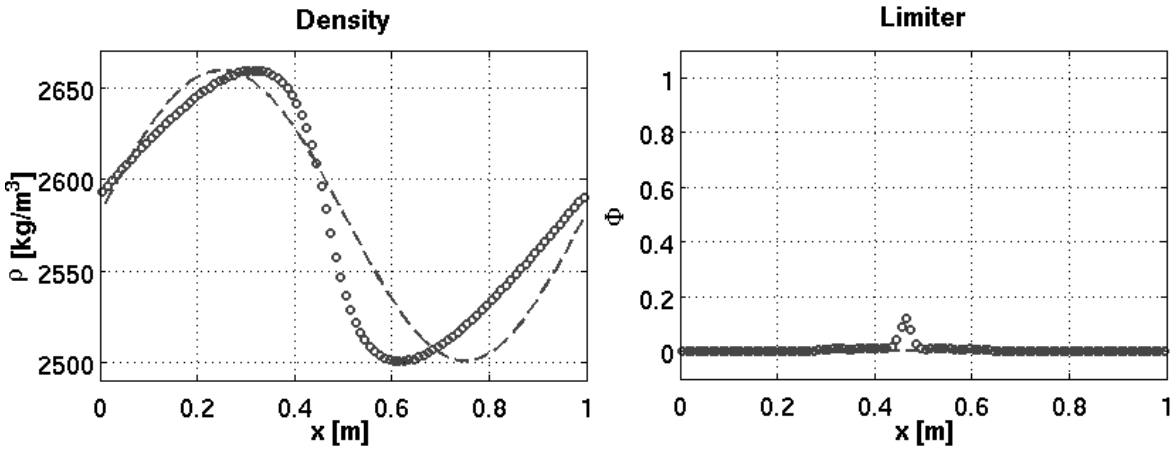

Figure 3.5: Simple wave simulation density and limiter profiles at $t = 0.5ms$. Simulation $CFL = 0.95$ and $\Delta x = 0.01m$. The dashed line refers to the initial conditions. As the solution progresses in time the wave slowly begins to break, inducing a gradual increase in the limiter locally centered around the steepening inflection point.

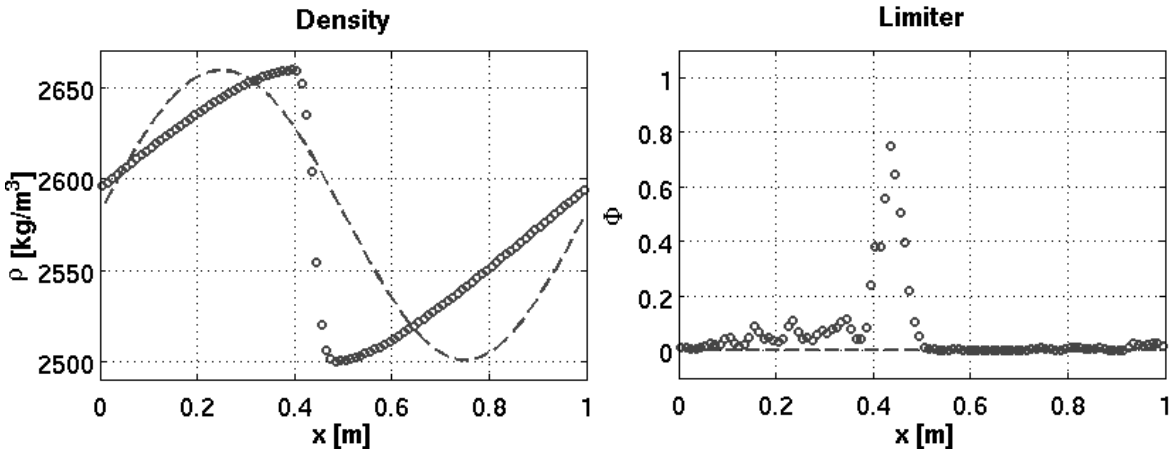

Figure 3.6: Simple wave simulation density and limiter profiles at $t = 1ms$. $CFL = 0.95$ and $\Delta x = 0.01m$. The dashed line refers to the initial conditions. As time progresses and a shock forms the limiter increases to introduce more dissipation locally, maintaining a relatively smooth flow on either side of the shock.

Table 3.2: Simple wave solution density L_2 error norm and convergence order for $t = 0.5ms$. As the grid is refined, the order of convergence is seen to approach the expected fourth-order value.

N	L_2 error	L_2 order
50	3.247172e-1	-
80	6.952834e-2	3.2792
100	3.173425e-2	3.5149
120	1.561053e-2	3.8903
150	6.574074e-3	3.8763
200	2.105829e-3	3.9572
300	4.161969e-4	3.9986

3.2.4.2 Aluminum impact problem

Next a single-phase test problem consisting of an impact between two slabs of aluminum in one dimension [81] is considered. A semi-infinite slab of aluminum with zero stress, corresponding to ρ_0, p_0, and e_0 given in 2.1, travels leftward at 2000 m/s striking a pre-compressed semi-infinite slab of aluminum with density $\rho = 4000\ kg/m^3$ and pressure $p = 7.98\ GPa$. Both slabs are modeled as fluids with a single Mie-Grüneisen equation with Hugoniots as reference state curves. The solution to this Riemann problem consist of a reflected and transmitted shock along with a constant pressure and velocity density jump between them.

Figure 3.7 presents results at $t = 50\ \mu s$ for simulation of the problem with 100 points and an adaptively maintained $CFL = 0.95$. The density, velocity, and pressure all remain relatively smooth. The limiter, plotted bottom right in Figure 3.7, demonstrates the necessary increase near the reflected and transmitted shocks. At the density contact the limiter is slightly less active, a desirable result that is a consequence of the nature of the limiter which decreases as numerical diffusion smooths out the flow. Ideally a hybrid switching criteria would indicate when the center-difference scheme is solely adequate to maintain the feature, however, this is hard to achieve this in practice.

3.2.4.3 Mach 2.5 MORB-molybdenum shock-contact problem

A one-dimensional shock-contact multiphase test problem involving two semi-infinite slabs that make diffuse contact at the origin is next simulated. To the left is molybdenum and the right MORB, states corresponding to ρ_0, p_0, and e_0. Mach 2.5 shock wave travels through the MORB to the left starting from $x = 0.5\ m$. The shock eventually reaches the origin, yielding a transmitted shock in the molybdenum slab and reflected shock back into the MORB. The diffuse contact at the origin is defined by smearing the initial mixture fraction

$$\psi(x, t = 0) = \frac{1}{2} + \frac{1}{2}\tanh(\beta x), \tag{3.71}$$

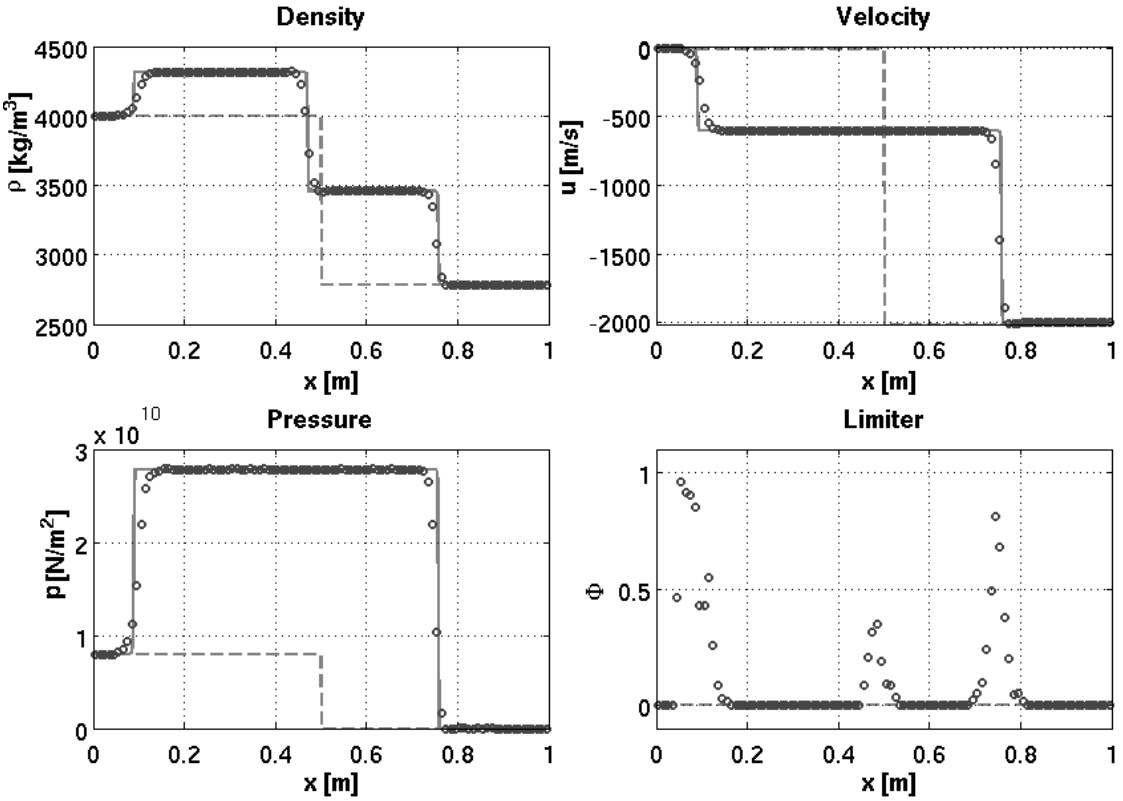

Figure 3.7: Results from a one-dimensional simulation of an aluminum impact problem with 100 points and $CFL = 0.95$ at $t = 50\ \mu s$. The dashed line refers to initial conditions and the solid line to the exact solution. The limiter adjusts at the reflected and transmitted shocks and interface, maintaining solution smoothness.

where $\beta = 50\ m^{-1}$ was taken. The states through diffuse contact are given by the ad hoc mixture rule (2.21).

To keep the contact well within the domain, the simulation is performed in an inertial frame of reference that gives zero velocity between the reflected and transmitted shocks. Results for 100 points and adaptively maintained CFL of 0.95 at $t = 0.18\mu s$ are seen in Figure 3.8. Again it is observed that the density, velocity, pressure, and initial mixture fraction maintain smooth profiles.

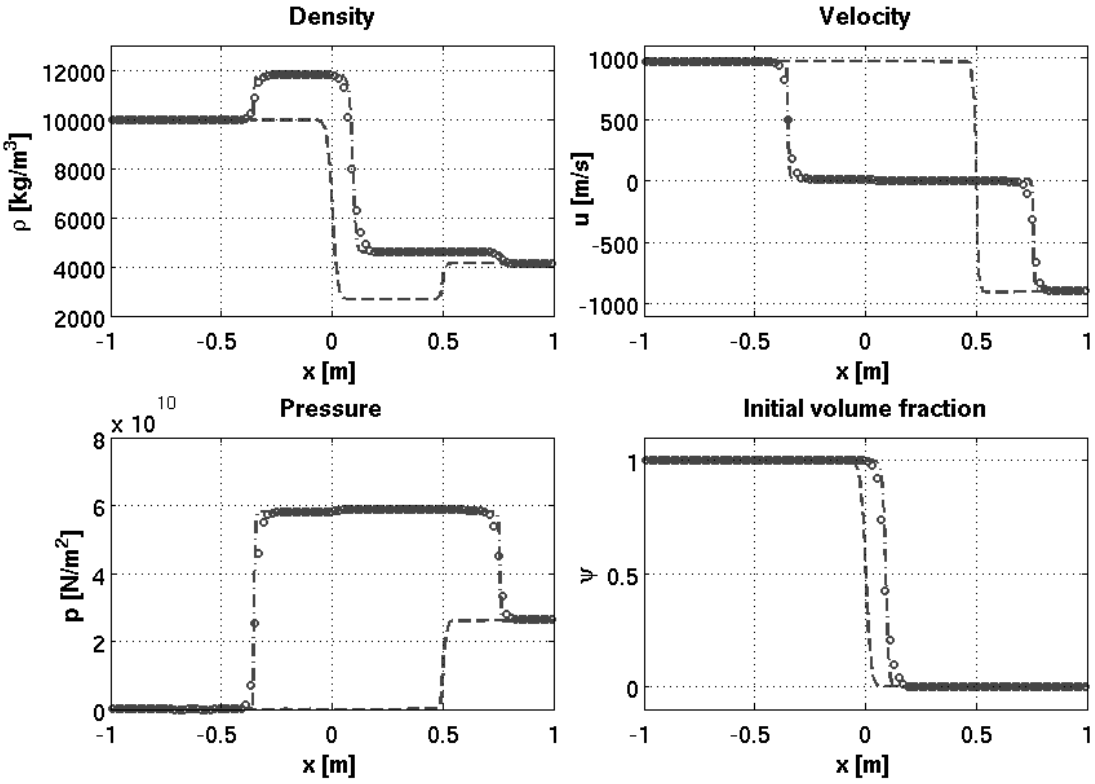

Figure 3.8: Mach 2.5 MORB-molybdenum shock-contact problem density, velocity, pressure, and mixture fraction plots for $t = 0.18\ ms$, shortly after shock-interface interaction. Simulation performed with 100 points and $CFL = 0.95$ maintained adaptively. The dashed line refers to initial conditions and the dash-dot line to a simulation with 1000 points. Transmitted and reflected shocks are observed, leaving a stationary contact in between.

3.2.5 two-dimensional test problem

3.2.5.1 Planar Richtmyer-Meshkov instability with reshock

To demonstrate the methodology in two dimensions, planar Richtmyer-Meshkov instability involving a single-cosine-mode perturbation of an interface between molybdenum and MORB with reshock is next simulated. A Mach 2.5 shock wave travels from top to bottom striking a diffuse interface with

initial mixture fraction perturbation described by

$$\psi(x, y, t = 0) = \frac{h_0}{2} \cos(2\pi x/\lambda)[1 + \tanh(\beta(y - y_0))], \tag{3.72}$$

where the wave length $\lambda = 0.5\ m$, $h_0 = 0.05\ m$, $y_0 = -0.05\ m$, and the factor $\beta = 50\ m^{-1}$. The ad hoc mixture rule (2.21) applied to ρ_0, P_0, and E_0 is then used to define the initial states in the diffuse region. The shock begins at position $y = 0.5\ m$ and travels downward. Unlike the one-dimensional shock-contact problem in the previous section the shock deposits vorticity in addition to creating reflected and transmitted shock waves. The vorticity deposited causes the perturbation to grow in time and eventually roll-up, making the solution complex in nature.

For the purposes of simulation, a domain of 0.5 m wide by 5.0 m tall was utilized with periodic boundary conditions in the x-direction. A base grid of 32 by 320 points was used with three levels of two times refinement corresponding to an effective resolution of 256 by 2560. A CFL of 0.9 is maintained adaptively through out the simulation. A perfectly reflecting wall is 3.8 meters away from the initial interface position of $y = -0.05$ meters. The perturbed transmitted shock travels toward the wall and eventually reflects off it. The reflected shock returns to the now growing perturbed interface, depositing more vorticity and yielding transmitted shocks and reflected expansion waves. Figure 3.9 gives schlieren density contours for time $t = 1.8ms$ calculated by the current fourth-order method and a purely third-order WENO reconstruction method. The time is well after reshock occurred and demonstrates finer roll-up for the present fourth-order methodology.

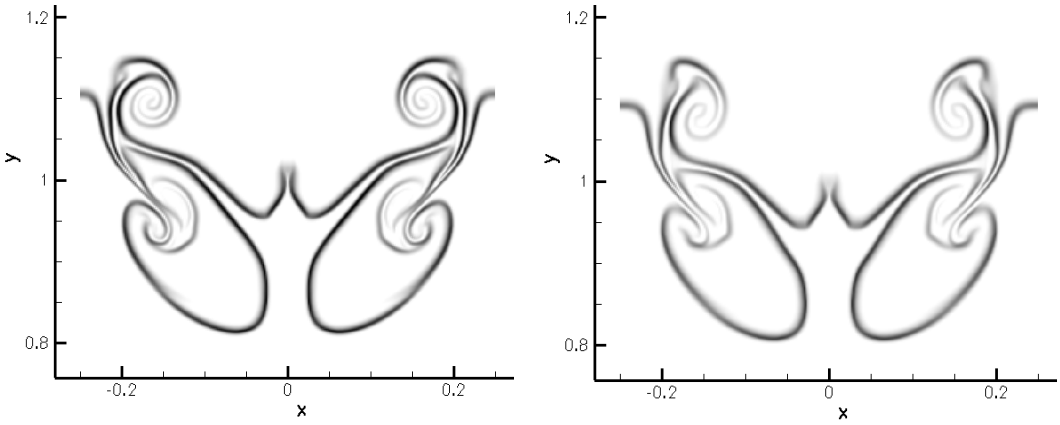

Figure 3.9: Mach 2.5 MORB-molybdenum single-mode Richtmyer-Meshkov instability with reshock schlieren contour plot for $t = 1.8\ ms$ calculated with (a) simulations with present method and (b) primitive third-order WENO reconstruction method. Simulation performed with a base grid of 32 by 320 points with three levels of two times refinement. Adaptive time stepping was used to maintain a CFL of roughly 0.9. The present scheme demonstrates slightly finer detail in small scale structures.

A plot of the amplitude as a function of time for the initial conditions simulated with third-

order WENO reconstruction and present fourth-order methodology is given in Figure 3.10. For Richtmyer-Meshkov instability, despite the complexity of the solution, a simple prediction for early time amplitude growth rate can be made. First-order linear analysis of an impulsively accelerated incompressible perturbed interface, first carried out by [53, 71], predicts that the amplitude growth rate is given by

$$\dot{h} = h_0^+ A^+ k \Delta u, \tag{3.73}$$

where h_0^+ is the post-shock perturbation amplitude, $A^+ = (\rho_4 - \rho_5)/(\rho_4 + \rho_5)$ is the post-shock Atwood ratio in accordance with Figures 1.1(a) and 1.1(a), $k = 2\pi/\lambda$ is the initial perturbation wave number, and Δu is the change in velocity of the interface imparted by the shock associated with the unperturbed shock-contact problem. Results for the amplitude of the present reshock problem are given in Figure 3.10. Making a linear fit of the data for early times yields a calculated impulsive growth rate of $4.914 \times 10^3\ s^{-1}$. Alternatively, the predicted impulsive growth rate from equation (3.73) is $\dot{h}/h_0^+ = 5.313 \times 10^3\ s^{-1}$, which agrees quite well with simulation results despite the simplicity of the model. For times before reshock, the amplitudes calculated with third-order WENO and present fourth-order method agree well. After reshock the measured amplitudes begin to demonstrate discrepancies due to variation in small scales responsible for an important part of vorticity deposition upon reshock [43].

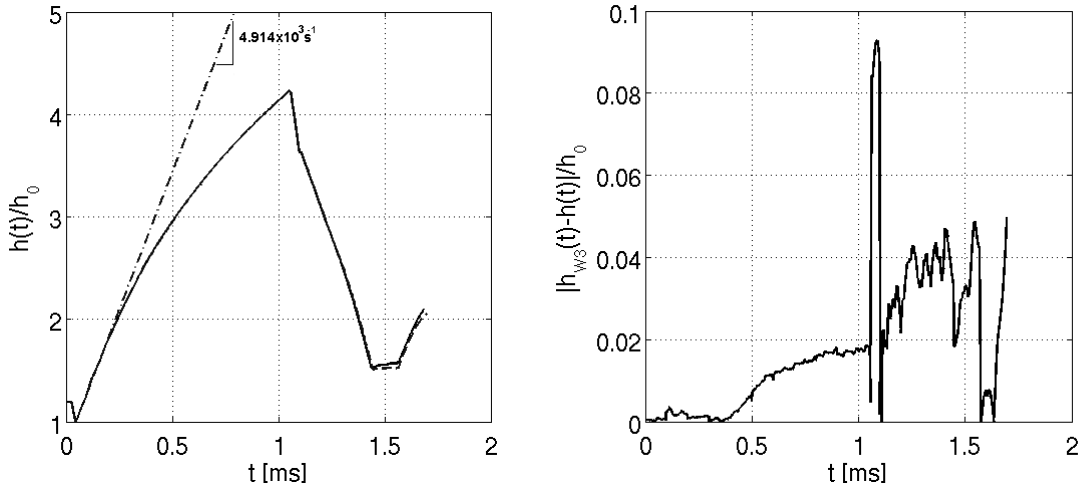

(a) (b)

Figure 3.10: (a) Mach 2.5 MORB-molybdenum Richtmyer-Meshkov instability amplitude growth for third-order WENO and present fourth-order methodology, denoted by dashed and solid lines, respectively. The dash-dot line represents a fit of data in the linear growth regime. The growth rate obtained is $4.914 \times 10^3 s^{-1}$, closely matching the simplified impulsive model of Richtmyer which predicts a growth rate of $5.313 \times 10^3 s^{-1}$. (b) The difference in amplitudes as predicted by third-order WENO and present fourth-order methodology. After reshock the two methods demonstrate increasing difference in predicted amplitude due to greater dissipation of small scales by the WENO method.

Chapter 4

Planar Richtmyer-Meshkov instability

The focus of the present Chapter is a comparison between planar Richtmyer-Meshkov instability in fluids with linear shock-particle centered-Hugoniot Mie-Grüneisen equations of state to that in gamma law gases. To begin, some background theory is given and then utilized to propose a system of matching flows between equations of state for comparison in at least a somewhat meaningful way. Following this, details of initial conditions and a convergence study under adaptive mesh refinement is given. Results for two Mach numbers in the "light-to-heavy" Richtmyer-Meshkov instability are then first presented for the single-mode case. A single Mach number is then used to study the triple-mode case. Following are "heavy-to-light" results, again for two Mach numbers.

4.1 Background theory

4.1.1 Impulsive model

Early attempts to model Richtmyer-Meshkov instability [53, 71] focused on solution to a linearization of the incompressible potential flow equations applied to the impulsive acceleration of a small amplitude corrugation of zero thickness between two fluids. A simple prediction for early time amplitude growth is arrived at from the model,

$$h(t) = h_0^+(1 + kA^+\Delta v t), \tag{4.1}$$

where, for application to modeling Richtmyer-Meshkov instability generated by an incident shock wave, h_0^+ is the post-shock corrugation amplitude, $A^+ = (\rho_4 - \rho_5)/(\rho_4 + \rho_5)$ is the post-shock Atwood ratio, $k = 2\pi/\lambda$ is the corrugation wave number, and Δv is the change in velocity of the interface imparted by the shock associated with the zero-corrugation problem. The linearization of flow equations used to achieve this result assumes that $kh_0^+ \ll 1$. The corresponding prediction for

the amplitude growth rate is given by

$$\dot{h}_\infty = h_0^+ k A^+ \Delta v. \tag{4.2}$$

Additionally, through simple geometric consideration, Richtmyer [71] predicted that the amplitude of the corrugation post-shock interaction should be

$$h_0^+ = h_0(1 - \Delta v / V_{s_1}), \tag{4.3}$$

where V_{s_1} is the incident shock speed relative to the corrugated contact.

Although the classical predictions of equations (4.1)–(4.3) remain important in understanding the underlying phenomenon, the assumptions used in achieving them lead to a narrow range of validity in application to shock-driven Richtmyer-Meshkov instability. A great deal of further analytic work has been performed to shed light on Richtmyer-Meshkov instability. Readers are referred to the original sources of these more complex models [93, 93–95, 98].

4.1.2 Nonlinear regime model

Transition to nonlinear growth occurs as the mixing layer width becomes large in order of magnitude relative to the wavelength ($kh(t) \sim 1$). A variety of attempts to analytically describe the behavior of this nonlinear phase have been made [1, 23, 27, 44, 82, 92, 97, 98]. Among these are incompressible potential flow models focused on predicting the behavior of the flow's large-scale coherent structure based on an incompressible treatment of the flow localized to the bubble or spike tip [1, 23, 44, 97]. Fourier series expansion for the velocity potential is utilized in such models yielding a set of coupled ordinary differential equations. Solution to the system generally predicts an asymptotic bubble velocity inversely proportional to time [23],

$$v_b(t) \to \frac{3 + A_0^+}{3(1 + A_0^+)kt}. \tag{4.4}$$

Thus, the evolution of the bubble position is predicted to be logarithmic in time.

4.1.3 Start-up time

Lombardini [50] has developed a modified impulsive model that takes into account the effect of a reflected and transmitted shock on the instability start-up phase. The model utilizes perturbation methods under the assumption that the parameter

$$\varepsilon_j = \frac{k h_0^+}{2\pi} A^+ \frac{\Delta v}{a_j}, \tag{4.5}$$

is small ($\varepsilon_j \ll 1$), for $j = 1, 2$ with a_j the speed of sound on either side. The transmitted and reflected shock waves, treated as moving boundaries, are shown to play a key role for early times by limiting the effective size of the domain. The theory falls short of making a prediction for the growth rate of the instability. However, the model does provide a useful prediction for the start-up time constant of the instability,

$$\tau = \frac{1}{2k}\Big(\frac{1 - A^+}{V_{s_4}} + \frac{1 + A^+}{V_{s_5}}\Big). \tag{4.6}$$

Here V_{s_4} and V_{s_5} are the reflected and transmitted shock speeds, respectively, in the frame of reference in which the zero-corrugation problem yields a stationary contact. For early times, the mixing layer growth rate is predicted to evolve as

$$\dot{h}(t) = \dot{h}_\infty t/\tau. \tag{4.7}$$

4.2 Matched parameters

The set of demensional parameters describing any flow can be subdivided into three categories: coordinate, initial condition, and equation of state parameters. In a stationary Cartesian coordinate system, the first category is composed of space and time variables

$$(x, y, z, t). \tag{4.8}$$

For single-mode, planar Richtmyer-Meshkov instability, the initial condition is described by three thermodynamic states and three spatial lengthscales associated with the corrugation. Remaining consistent with the labeling of Figures 1.1 and 1.2, the-dimensional intial condition parameter family is

$$(p_1, \rho_2, p_2, \rho_3, \lambda, h_0, \delta). \tag{4.9}$$

Here δ has been added to describe the lengthscale of the mixed-phase zone where the two materials meet at the corrugation. The state behind the shock is only described by one thermodynamic variable because it must lie on the Hugoniot of the state ahead. Additionally, the pressure across the corrugation is continuous and therefore one less thermodynamic quantity is required. It is important to note that thermodynamic variables are interchangeable and therefore the choice of density and pressure used to describe the initial states is not unique.

With fixed equations of state, the initial condition and coordinate parameters provide a basis for a set of nondimensional quantities that define complete similarity between flows. However, presently, the goal is to compare Richtmyer-Meshkov instability across equations of state. For perfect gases a

and b, the specific heats

$$(c_p^a, c_v^a, c_p^b, c_v^b) \tag{4.10}$$

form the set of-dimensional equation of state dependent parameters. These can be reduced to two nondimensional parameters, the specific heat ratios

$$(\gamma^a, \gamma^b), \tag{4.11}$$

required to be matched for complete flow similarity. Alternatively, for two linear shock-particle speed Hugoniot based Mie-Grüneisen equations of state, the list of dimensionless parameters is three times as long,

$$(\frac{p_0^a}{\rho_0^a {c_0^a}^2}, \Gamma_0^a, \sigma^a, \frac{p_0^b}{\rho_0^b {c_0^b}^2}, \Gamma_0^b, \sigma^b). \tag{4.12}$$

Although some correlation can be drawn between Γ_0 and γ, there is no clear cut meaning for σ since perfect gases do not have at least one Hugoniot with a linear shock-particle speed relationship. Achieving complete flow similarity across equations of state is therefore not a realistic goal, providing motivation for the present study. A weaker form of similarity must then be applied as a basis for comparison.

Of fundamental interest to the study of Richtmyer-Meshkov instability is the mixing layer width time evolution $h(t)$. Presently the mixing layer width time evolution is taken as the basis for comparison across equations of state. With the equation of state fixed, Buckingham's pi theorem can be utilized to define a nondimensional form of the instability amplitude strictly as a function of nondimensional intial conditions and time. The-dimensional parameters of interest are

$$(h(t), t, p_1, \rho_2, p_2, \rho_3, \lambda, h_0, \delta). \tag{4.13}$$

There are three fundamental physical quantities among these nine variables (length, time, mass). Therefore, six nondimensional groups can be formed,

$$\frac{h}{\lambda}\Big(\frac{t}{\lambda}\sqrt{\frac{p_2}{\rho_2}}\Big) = \frac{h}{\lambda}\Big(\frac{t}{\lambda}\sqrt{\frac{p_2}{\rho_2}}, \frac{p_1}{p_2}, \frac{\rho_2}{\rho_3}, \frac{h_0}{\lambda}, \frac{\delta}{\lambda}\Big). \tag{4.14}$$

Even when limited to the-dimensional parameters in 4.13, these six groups are not unique. Furthermore, there is no reason to believe that matching such parameters across equations of state will yield any similarity in the nondimensional mixing layer width evolution.

To formulate a more meaningful set of nondimensional parameters it is useful to draw on theory of Richtmyer-Meshkov instability. Richtmyer's linear theory provides a direct prediction for the

post-shock evolution of the nondimensional mixing layer width,

$$\frac{h}{\lambda}\Big(\frac{t}{\tau}\Big) = \frac{h_0^+}{\lambda}\Big(1 + \frac{t}{\tau}\Big), \tag{4.15}$$

where the time scale is given by

$$\tau = (kA^+\Delta v)^{-1}. \tag{4.16}$$

The quantities Δv and A^+ are theoretical predictions for one-dimensional Riemann problems and are therefore strictly related to the thermodynamic states of the initial conditions. Likewise, Richtmyer's linear theory predicts the quantity h_0^+ directly from the initial thermodynamic states and corrugation shape. So long as the final number of nondimensional parameters remains the same, the-dimensional quantities predicted to be of importance by Richtmyer's linear theory can therefore be interchanged with those in 4.14. The resulting nondimensional parameter family should be a better approximation to those necessary to achieve similar nondimensional mixing layer width evolution across flows with different equations of state. Proceeding in this fashion, the nondimensional time evolution of the mixing layer width can be recast in the functional form

$$\frac{h}{\lambda}\Big(kA^+\Delta v t\Big) = \frac{h}{\lambda}\Big(kA^+\Delta v t, \frac{\Delta p}{\rho a_2^2}, A^+, kh_0^+, k\delta\Big). \tag{4.17}$$

In addition to Richtmyer's linear theory, the incident shock strength, originally formulated nondimensionally in terms of the ratio of pressures across the shock, has been replaced by the more robust nondimensional measure of pressure change.

The procedure for setting up matched simulations defined by 4.17 is now described. First, two Mie-Grüneisen fluids are chosen, one "heavy" and one "light." An incident shock Mach number and initial corrugation shape kh_0 are then chosen. From the Mach number the nondimensional pressure jump across the incident shock is determined along with the predicted post-shock Atwood ratio A^+, velocity impulse Δv, and post-shock corrugation shape kh_0^+. From these quantities an itterative process to determining the appropriate perfect gases for matching is undertaken. The additional physical constraint of thermodynamic equilibrium is imposed across the corrugation of the perfect gases. An initial guess for the properties of the gases is made from the Atwood ratio which only depends on the specific heats. The incident shock strength is matched and then an itterative process involving the solution to the uncorrugated Riemann problem is performed to determine the final properties of the perfect gases needed to match the nondimensional values 4.17 associated with the Mie-Grüneisen fluids.

4.2.1 Initial conditions

In practice only weak convergence can be obtained for the numerical solution of hyperbolic partial differential equations with discontinuities [46, 86]. To obtain smooth solutions free of oscillations up-winding is generally required at sharp features, leading to numerical diffusion. Furthermore, gradients on the order of the grid scale can sometimes develop into undesirable fluid instabilities. It is therefore necessary to smear the initial material contact such that several grid points are present across the mixed zone,

$$\rho(x, y, t = 0) = \rho_3 + (\rho_2 - \rho_3)w(y, x), \tag{4.18}$$

with

$$w(x, y) = \frac{1}{2} + \frac{1}{2}\tanh\big(\delta(y - y_c(x))\big), \tag{4.19}$$

where $y_c(x)$ is the centerline of the mixed region defined by $y_c(x) = h_0\cos(kx)$. The quantity δ is a parameter which describes the mixed zone width. Presently, it is not the purpose of the study to explore the effect of δ. Therefore, a value which yields a mixed zone of ten points is used simply to prevent gridscale-driven features from developing. Similarly, across the shock, to minimize errors introduced by approximation of the solution to the Riemann problem by linearization, it is useful to smear the shock wave. The shock is then located as close to the corrugated contact as is possible so that quantities in front of the shock are matched to within a hundredth of a percent of those given by the smeared interface. For all simulations the shock wave starts from above the interface.

In order to maximize efficiency of the domain and mesh utilized, the frame of reference is taken to be that for which the corresponding one-dimensional Riemann problem yields zero velocity for the contact post-shock interaction. Additionally, the initial location of the interface and shock combination are taken such that waves corresponding to the one-dimensional Riemann problem reach the ends of the domain at the same time.

4.2.2 Boundary conditions

The domain is chosen to have a large aspect ratio so as to minimize interaction of the flow field at the material interface with the boundary. Additionally, when necessary the domain is truncated to eliminate shock wave interaction with the top and bottom boundaries. In the horizontal direction the domain is taken to be periodic in nature. Ghost cells are used to implement the periodic boundary conditions in an AMR context. The top and bottom of the domain utilize non-reflecting outflow [74, 84] in a simultaneous approximation term (SAT) [12].

4.3 Convergence testing

A mesh refinement study using adaptive mesh refinement for the "light-to-heavy" case with a Mach 2.5 incident shock was performed to determine the needed effective resolution to capture the mixing layer amplitude effectively. Results for the study are given in Figure 4.1 for up to five mesh levels with successive 2x refinement for a base mesh of 32 points per corrugation wavelength. To the left the amplitude is plotted as a function of time and to the right the L_1 error based on the finest mesh calculation. The size for the mixed cell zone was held constant under refinement. Significant differences in the amplitudes as a function of time are observed between refinements for the first three mesh levels. Between the three- and five-level meshes less significant change is observed. The convergence rate of the amplitude with effective mesh size is slightly greater than one. Engquist [20] demonstrated that in smooth regions behind discontinuities the L_1 error convergence rate of any numerical method will be approximately first order.

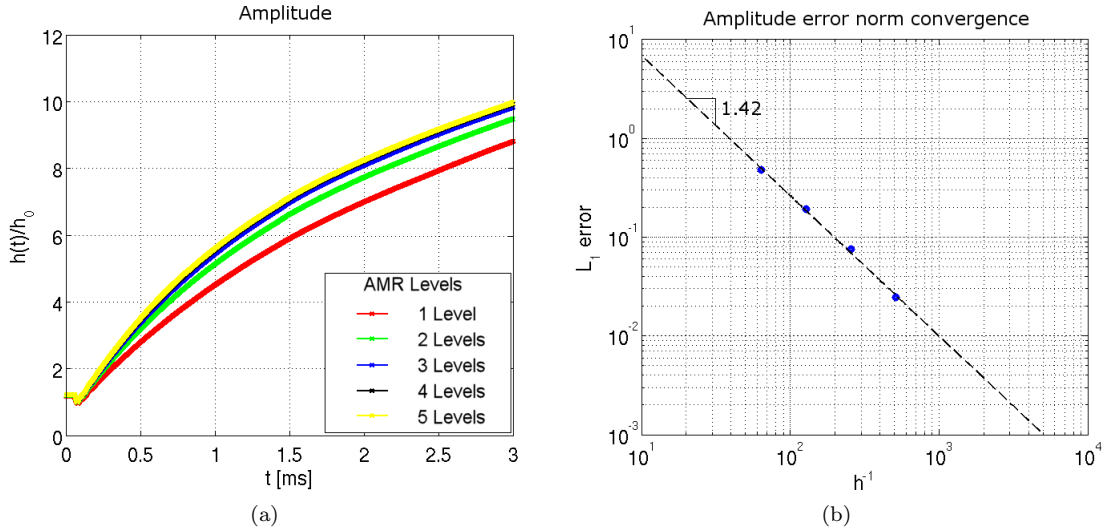

Figure 4.1: "Light-to-heavy" Mach 2.5 Richtmyer-Meshkov amplitude plot and amplitude convergence plot. The convergence rate is based upon the L_1 norm of the amplitude post-shock corrugation interaction for times up to 1.0 ms

Therefore for all simulations a four-level mesh with a base mesh of 32 points per corrugation wavelength and a refinement factor of two for each level beyond the first, corresponding to 256 points per corrugation wavelength was used. Figure 4.2 demonstrates the behavior of the mesh refinement around the unstable interface created by an incident Mach 1.87 shock in perfect gases with gamma of 1.248 and 1.09, "light" and "heavy", respectively. A CFL number of 0.85 was maintained adaptively for all simulations.

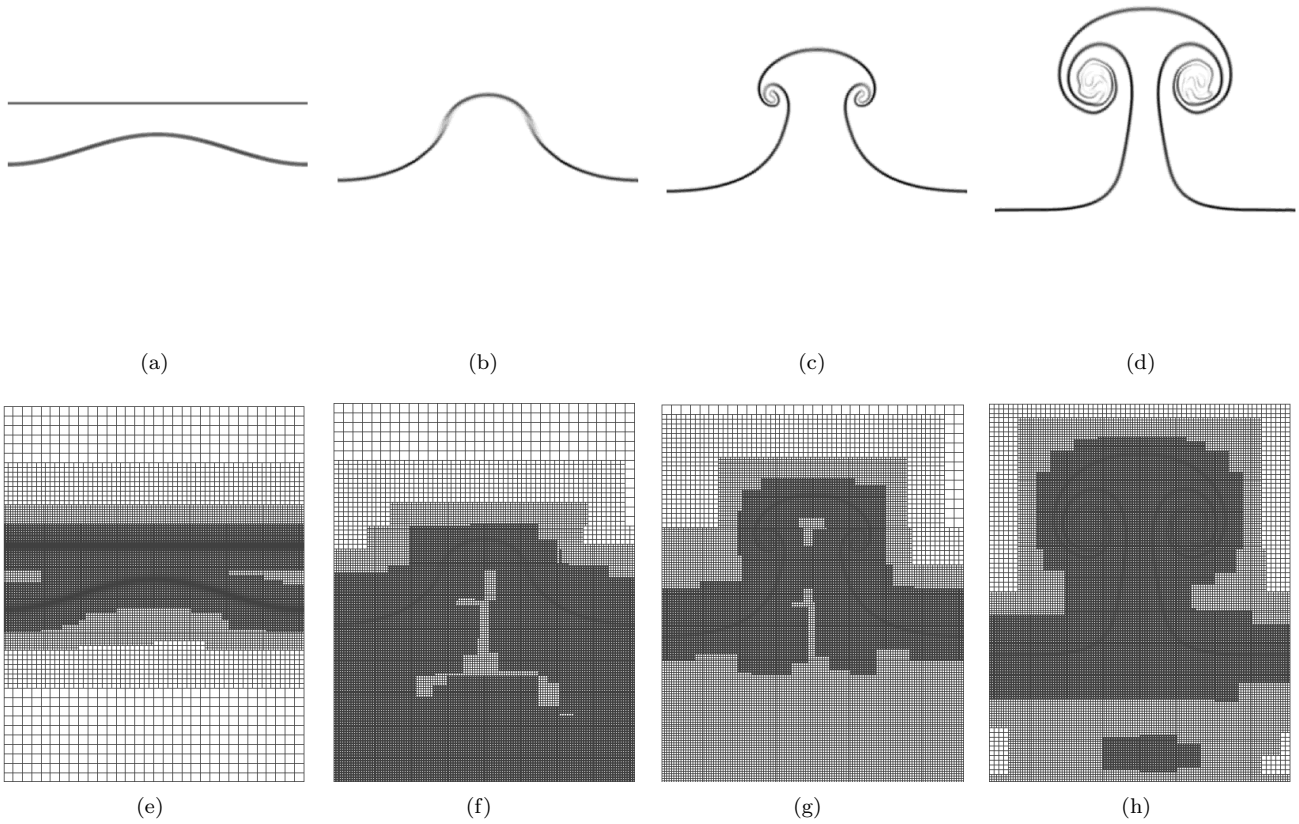

Figure 4.2: Perfect gas "light-to-heavy" Mach 1.87 single-mode Richtmyer-Meshkov instability schlieren plots and mesh plots for times -0.075, 1.225, 2.69, and 6.1 milliseconds

4.4 "Light-to-heavy" single-mode

To investigate the role of the equation of state in Richtmyer-Meshkov instability the single-mode "light-to-heavy" case is first studied. In order to achieve an Atwood ratio of roughly a half, MORB and molybdenum were chosen for the materials with Mie-Grüneisen equation of state. The Hugoniot constants for these two materials are found in Table 2.1. For perfect gases, Air and SF6 were taken as a starting point for intial conditions, the latter being modified in properties to achieve the matched post-shock Atwood ratio. The two Mach numbers 1.5 and 2.5 were arbitrarily chosen. for the MORB and molybdenum case provide a basis for comparison in parameter space. An initial corrugation amplitude of 5% of the wavelenth for MORB and molybdenum was taken with the intention of yielding a value of kh_0^+ sufficient to result in a brief linear growth period. Tabulation of initial conditions and relevant post-shock quantites for zero-corrugation are found in Table 4.1. The unshocked prefect gases are taken to be at approximately room temperature and pressure (T=300 K, p=1 atm). Similarly, the unshocked Mie-Grüneisen fluids are in thermodynamic equilibrium at (ρ_0, p_0), repsectively. Below the entries for MORB and molybdenum are tabulation of initial and post-shock conditions as well, as properties for the corresponding perfect gas cases, matched in the manner proposed in Section 4.2.

MORB-molybdenum

M_s	$\Delta p/\rho_0 c_0^2$	kh_0	A^-	A^+
1.5	0.893	0.10π	0.578	0.479
2.5	4.464	0.10π	0.578	0.438

Perfect gas

M_s	$\Delta p/\rho_0 c_0^2$	kh_0	A^-	A^+
1.225	0.893	0.12π	0.455	0.479
1.87	4.464	0.17π	0.359	0.438

Table 4.1: Initial conditions for single-mode Richtmyer-Meshkov instability in the "light-to-heavy" case for Mie-Grüneisen and perfect gas equations of state

Perfect gas properties

M_s	γ_1	c_{v_1}	γ_2	c_{v_2}
1.225	1.248	$7.17 kJ/kgK$	1.09	$7.40 kJ/kgK$
1.87	1.248	$7.17 kJ/kgK$	1.09	$9.32 kJ/kgK$

Table 4.2: Perfect gas properties for single-mode Richtmyer-Meshkov instability in the "light-to-heavy" case.

Figure 4.3 shows density gradient magnitude contours for the Mach 1.5 case and matched perfect gas, respectively, at several matched nondimensional times. Likewise, Figure 4.4 shows density gradient magnitude contours for the Mach 2.5 case and matched perfect gas. At each time the perfect gas solution, seen on the right of each figure, demonstrates a significantly smaller mixing

layer width compared to the corresponding Mie-Grüneisen solutions to the left. For later times significant variation is observed from one case to another in the shapes of the material contact, particularly in the roll-up.

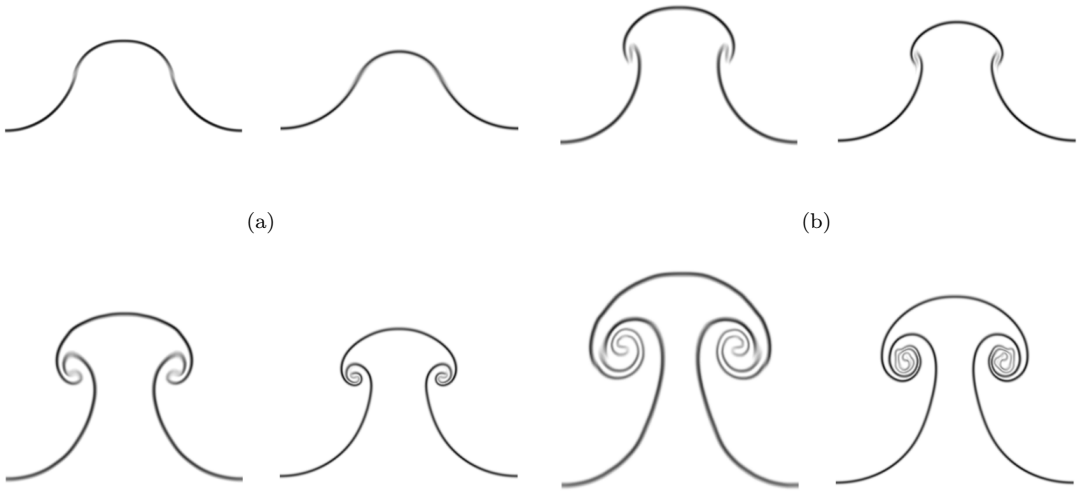

Figure 4.3: "Light-to-heavy" MORB-molybdenum (left) and equivalent perfect gas (right) single-mode Richtmyer-Meshkov instability schlieren plot comparison for Mach 1.5 incident shock at nondimensional times (a) 3.28, (b) 6.56, (c) 9.834, and (d) 16.39.

4.4.1 Amplitude and growth rate

Of fundamental interest to the study of Richtmyer-Meshkov instability is the mixing layer width and its growth rate which are presented in the current section. Various definitions exist for mixing layer amplitude [41, 43]. Here amplitude is defined by a position weighted integral of the scalar mixture fraction for solids modeled by isotropic Mie-Grüneisen equations of state and mass fraction for perfect gases. Before roll-up occurs the interfaces centerline can be determined by

$$y_{cd}(x,t) = \frac{\int_{-\infty}^{\infty} y\psi(x,y,t)(1-\psi(x,y,t))dy}{\int_{-\infty}^{\infty} \psi(x,y,t)(1-\psi(x,y,t))dy}, \tag{4.20}$$

where ψ is the ad hoc mixture fraction. The instability amplitude is then

$$h(t) = \frac{1}{2}(y_{spike}(t) - y_{bubble}(t)), \tag{4.21}$$

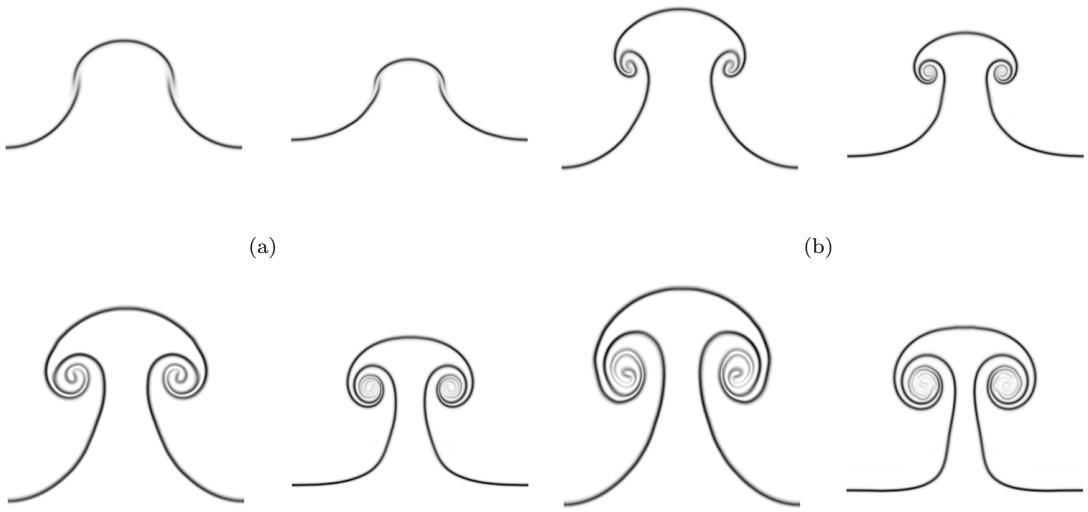

Figure 4.4: "Light-to-heavy" MORB-molybdenum (left) and equivalent perfect gas (right) single-mode Richtmyer-Meshkov instability schlieren plot comparison for Mach 2.5 incident shock at nondimensional times (a) 5.31, (b) 10.62, (c) 15.93, and (d) 21.25

where $y_{spike}(t)$ and $y_{bubble}(t)$ are

$$\begin{aligned} y_{spike}(t) &= max(y_{cd}(x,t) - y_0(t)), \quad -\tfrac{\lambda}{2} < x < \tfrac{\lambda}{2}, \\ y_{bubble}(t) &= min(y_{cd}(x,t) - y_0(t)), \quad -\tfrac{\lambda}{2} < x < \tfrac{\lambda}{2}. \end{aligned} \tag{4.22}$$

Here $y_0(t)$ denotes the position of the interface for the unperturbed shock-interface problem as a function of time. Although equation (4.20) fails to capture the centerline of the interface for later times when roll-up has occurred it still provides a useful measure of the amplitude so long as a single transition zone between phases exist along the vertical line passing through the spike and bubble locations.

Utilizing the above definition for amplitude, Figures 4.5 and 4.5, respectively, display nondimensionalized results for Mach 1.5 and 2.5 Richtmyer-Meshkov instability for the MORB-molybdenum "light-to-heavy" case and associated perfect gas matching. Several differences are observable in these plots. First, note an apparent difference in start-up times is evident in the amplitude growth plot. The perfect gas case clearly demonstrates a longer start-up time, as is predicted by equation (4.5) through an inverse dependence on wave speed and corrugation wavenumber. Wave speeds in solids tend to be significantly higher than those for gases by an order of magnitude. This, along with the wavenumber adjustment required for matching predicted linear growth rates, account for the shorter delay in the MORB-molybdenum cases. Table 4.3 gives corresponding start-up times as predicted by

equation (4.5) under column labeled τ_{1D} and approximate values from two-dimensional results. The meaning of start-up time implies the existence of a nearly steady state for the linear growth regime and therefore values are not quoted with accuracy because such a steady state is not observed in the present growth rate plots. At best the linear growth regime is brief for the MORB-molybdenum cases. The predicted start-up times still remain close in order of magnitude to the measured values in spite of the lack of a true linear growth phase. Increasing Mach number appears to increase the variation in amplitude between equations of state. At the lower Mach number, aside from the shift due to start up, the amplitude growth of each equation of state appears quite similar. Alternatively, the perfect gas matching for the Mach 2.5 MORB-molybdenum case decays away from its maximum growth rate much faster. The growth rate plots provide important further insight into the

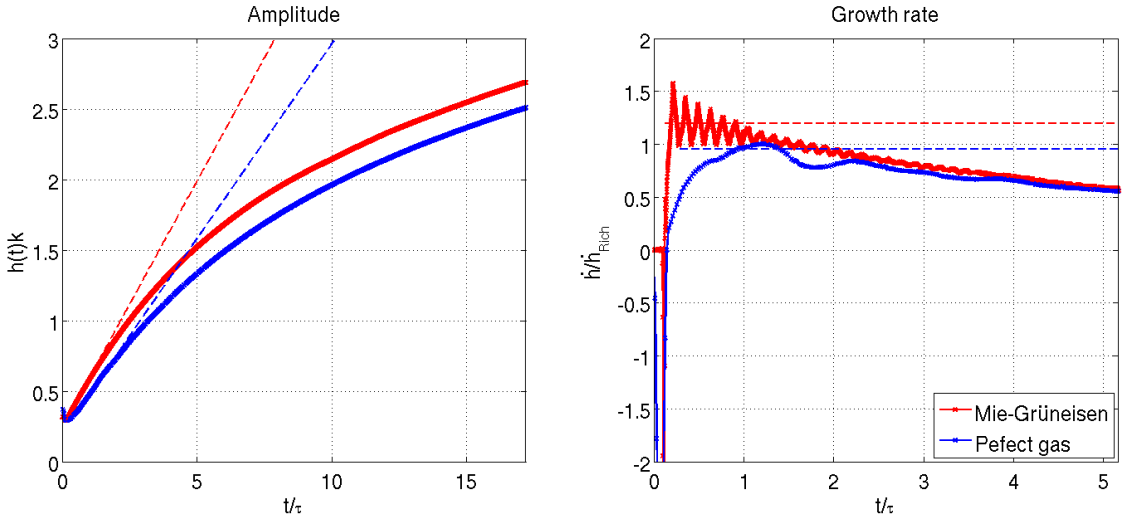

(a) (b)

Figure 4.5: "Light-to-heavy" Mach 1.5 single-mode Richtmyer-Meshkov instability amplitude growth plot (a) and amplitude growth rate plot (b). A start-up time difference is clearly observable between the MORB-molybdenum and perfect gas case. Additionally, post start-up the growth rates are observed to oscillate at considerably different frequencies and amplitudes.

MORB-molybdenum		
M_s	τ_{1D}/τ	τ_{2D}/τ
1.5	0.0228	~ 0.0328
2.5	0.0738	~ 0.0531
Perfect gas		
M_s	τ_{1D}/τ	τ_{2D}/τ
1.225	0.259	~ 0.393
1.87	1.02	~ 1.32

Table 4.3: Start-up times for Richtmyer-Meshkov instability as approximated by zero-corrugation Riemann solution and two-dimensional simulation results

behavior of the mixing layer. Clearly evident are decaying oscillations in growth rate which appear

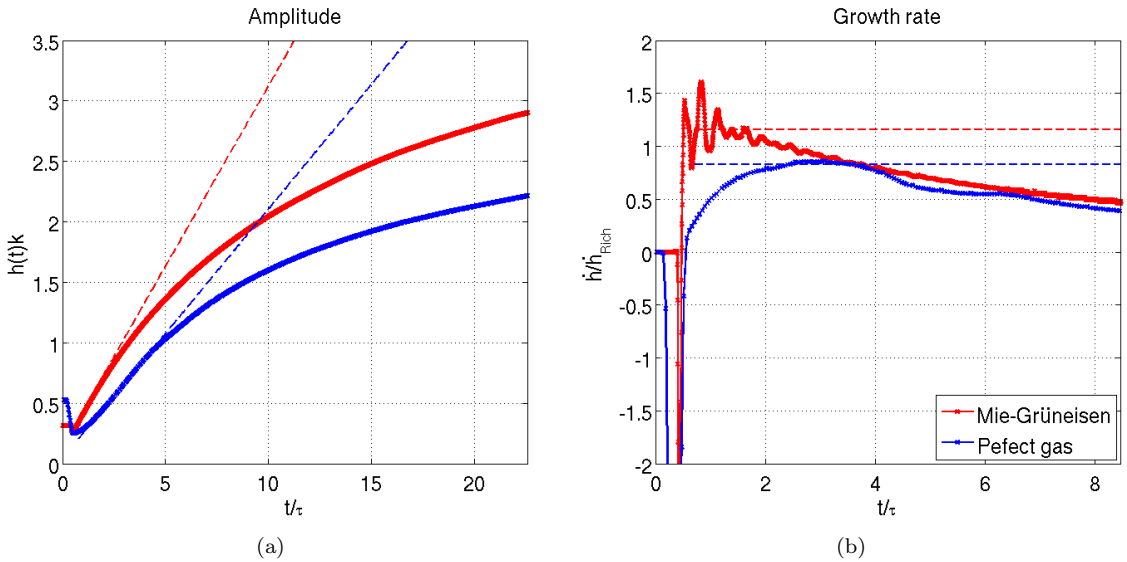

(a) (b)

Figure 4.6: "Light-to-heavy" Mach 2.5 single-mode Richtmyer-Meshkov instability amplitude growth plot (a) and amplitude growth rate plot (b). Again, a start-up time difference is clearly observable between the MORB-molybdenum and perfect gas case. Post start-up oscillations in growth rate for MORB-molybdenum are at much greater frequency and amplitudes than those of the perfect gas.

to be nearly constant in frequency for early times. The MORB-molybdenum cases demonstrate a much higher frequency and amplitude of oscillation than the corresponding perfect gas cases. These oscillations are a direct consequence of the perturbed transmitted and reflected shocks. For most materials, small perturbations in shock shape are stable, oscillating and decaying in time [19]. The oscillation frequency dependence is complex in nature, however, it is directly related to the speed of sound behind the shock and shock perturbation wavenumber [42],

$$(\omega_j - k_y v)^2 = a_j^2(k_x^2 + k_y^2). \tag{4.23}$$

Just as in the start-up time, corrugation wavenumber and material wave speeds are seen to play a similar role in determining the frequency of oscillation, yielding a much higher frequency for MORB-molybdenum than the matched perfect gas case. Table 4.4 gives approximate values for the oscillation frequencies of the transmitted and reflected shocks based on this formula. Additionally, calculated from a Gaussian filtered polynomial fit of the growth rate after shock-interface interaction is a discrete Fourier transform of the growth rate. In general there should be two frequencies observed, however, one is generally dominant after early times as the decay of influence is proportional to the distance. Figure 4.7 presents the power spectrum for the Mach 2.5 MORB-molybdenum demonstrating the two peaks which are not observed in any of the other simulations, most likely for the reasons discussed. Tabulated in 4.4 are the dominantly observed frequency along with the simple approximation values.

MORB-molybdenum

M_s	$\tau f_{R_{1D}}$	$\tau f_{T_{1D}}$	τf_{2D}
1.5	7.05	7.86	7.06
2.5	3.80	2.39	4.99

Perfect gas

M_s	$\tau f_{R_{1D}}$	$\tau f_{T_{1D}}$	τf_{2D}
1.225	1.22	0.68	1.06
1.87	0.43	0.25	0.37

Table 4.4: Nondimensionalized dominant growth rate oscillation frequency $f_{2D}\tau$ for "light-to-heavy" Richtmyer-Meshkov instability and approximate perturbed transmitted and reflected shock oscillation frequency, $f_{T_{1D}}\tau$ and $f_{R_{1D}}\tau$, respectively, based on solution to the zero-corrugation Riemann problem

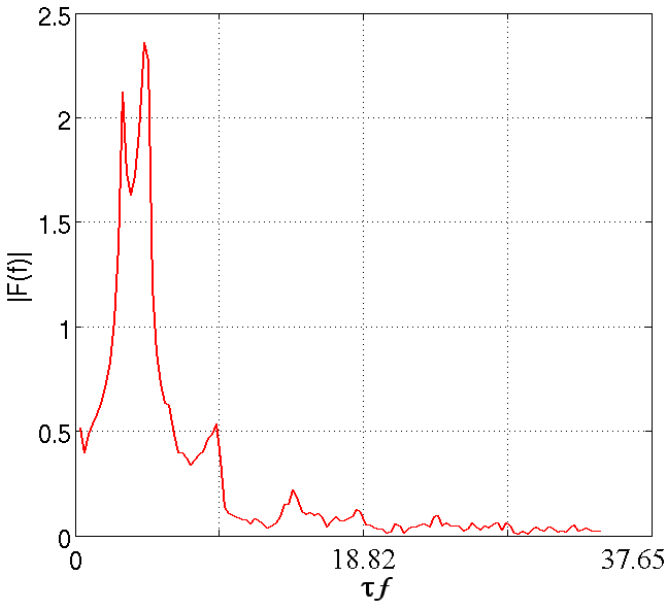

Figure 4.7: "Light-to-heavy" Mach 2.5 single-mode Richtmyer-Meshkov instability Gaussian filtered mixing width growth rate spectrum. A peak in the nondimensionalized frequency response is observed at 49.19.

4.4.2 Nonlinear bubble evolution

Next investigated is the evolution of the bubble in the nonlinear regime. Figure 4.8 gives the bubble position as a function of time for Mach 1.5 and 2.5 MORB-molybdenum cases and the equivalent matched perfect gas cases. The plots, given in semi-log format, demonstrate a logarithmic growth nonlinear growth period in all studied cases. The Mach 2.5 matched perfect gas case simulation also demonstrates a somewhat unexpected reversal of bubble velocity as the curvature of the bubble reaches zero. In each of the plots a dashed line is shown representing the predicted asymptotic slope for the logarithmic time evolution of the bubble by equation (4.4). In each case the simulation results yield a smaller slope than those of the potential flow prediction.

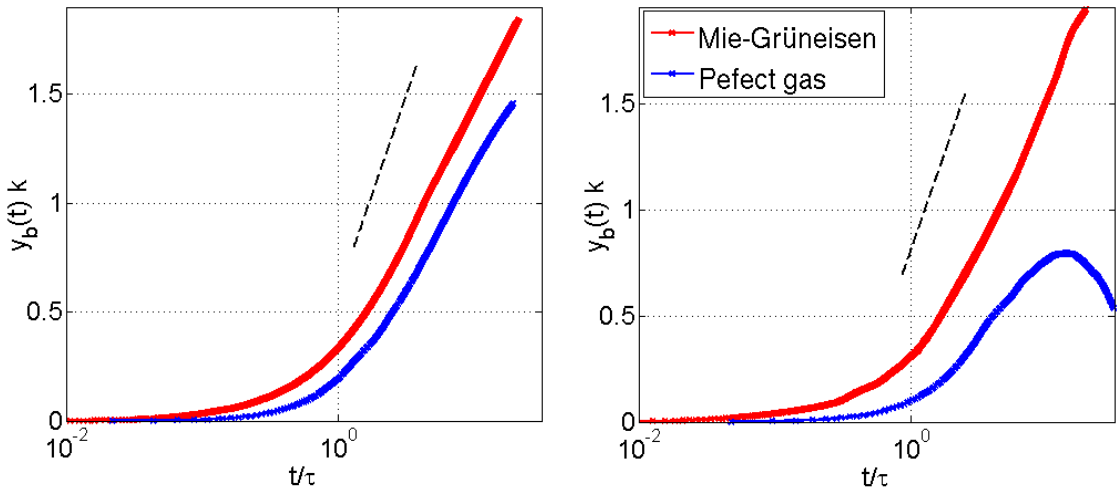

(a) (b)

Figure 4.8: "Light-to-heavy" single-mode Richtmyer-Meshkov instability bubble position semi-log plot for (a) Mach 1.5 and (b) Mach 2.5 cases. The dashed line in the plots represents Goncharov's potential flow slope prediction for the slope of the logarithmic evolution of the bubble in time.

MORB-molybdenum

M_s	*Simulation*	$\frac{3+A^+}{3(1+A^+)}$
1.5	0.558	0.784
2.5	0.686	0.797

Perfect gas

M_s	*Simulation*	$\frac{3+A^+}{3(1+A^+)}$
1.225	0.495	0.784
1.87	0.327	0.797

Table 4.5: Tabulated comparison of two-dimensional bubble evolution parameter for the nonlinear growth regime and Goncharov's nonlinear bubble potential flow approximation

4.4.3 Integral vorticity

Results for the vorticity distribution as deposited by the shock are now given. For a discontinuous corrugation the circulation deposited is merely the transverse velocity jump across the different phases. Numerically it is not possible to measure this, however, since the majority of the vorticity within the domain will be associated with the initial deposition at the contact, an integral of vorticity is examined,

$$\Delta u(x,t) = \int_{-\infty}^{\infty} \omega(x,y,t)dy, \tag{4.24}$$

which is directly related to the tangential velocity jump across the contact. Numerically the integration is carried out by a trapezoidal rule with differentiation of the velocity field by a *Minmod* limiter [45, 86]. Calculation of the power spectrum for each distribution is done by discrete Fourier transform and smoothed out by a high-order least-squares polynomial fit of the spectrum's loga-

rithm. Figures 4.9 and 4.10, respectively, display normalized vorticity distributions and associated power spectrum shortly after shock interaction for MORB-molybdenum Mach 1.5 and 2.5 Richtmyer-Meshkov instability and corresponding perfect gas cases of matched initial conditions. In spite of secondary wave effects, the vorticity distribution exhibits the behavior of a sinusoidal distribution with a single-mode to within roughly 15%, in good agreement with the prediction of Samtaney and Zabusky [76],

$$\Delta u(x,t) = \int_{-\infty}^{\infty} \omega(x,y,t)dy, \tag{4.25}$$

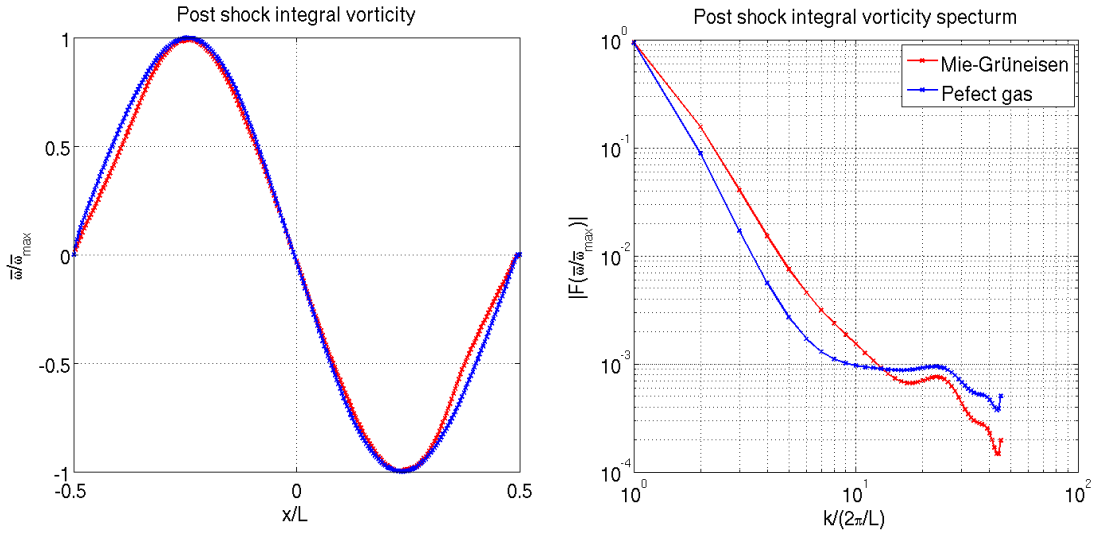

(a) (b)

Figure 4.9: "Light-to-heavy" Mach 1.5 single-mode Richtmyer-Meshkov instability post-shock integral vorticity plot (a) and integral vorticity power spectrum plot (b). Significant change is observed between equations of state due to the nature of the Hugoniot.

4.4.4 Post-shock interface centerline

Next investigate is the post-shock interface centerline as defined by equation (4.20). Figures 4.11 and 4.12, respectively, display normalized centerline plots and associated power spectrum shortly after shock interaction for MORB-molybdenum Mach 1.5 and 2.5 Richtmyer-Meshkov instability and corresponding perfect gas cases of matched initial conditions. The centerlines are seen to remain as a single-mode to within roughly 5%. Furthermore, noted is that the post-shock amplitude agrees to within a percent with the estimate of equation (4.3).

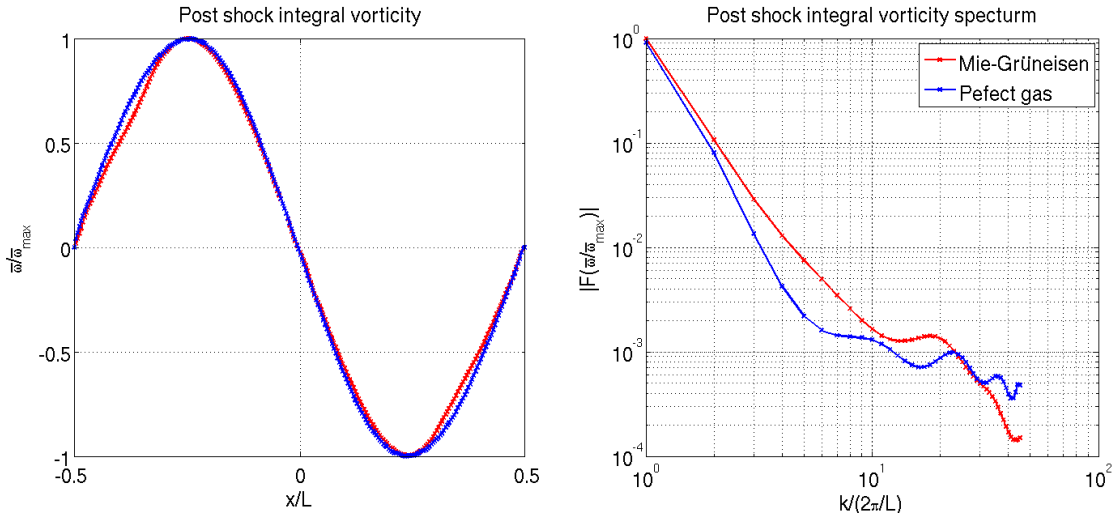

(a) (b)

Figure 4.10: "Light-to-heavy" Mach 2.5 single-mode Richtmyer-Meshkov instability post-shock integral vorticity plot (a) and integral vorticity power spectrum plot (b). Significant change is observed between equations of state due to the nature of the Hugoniot.

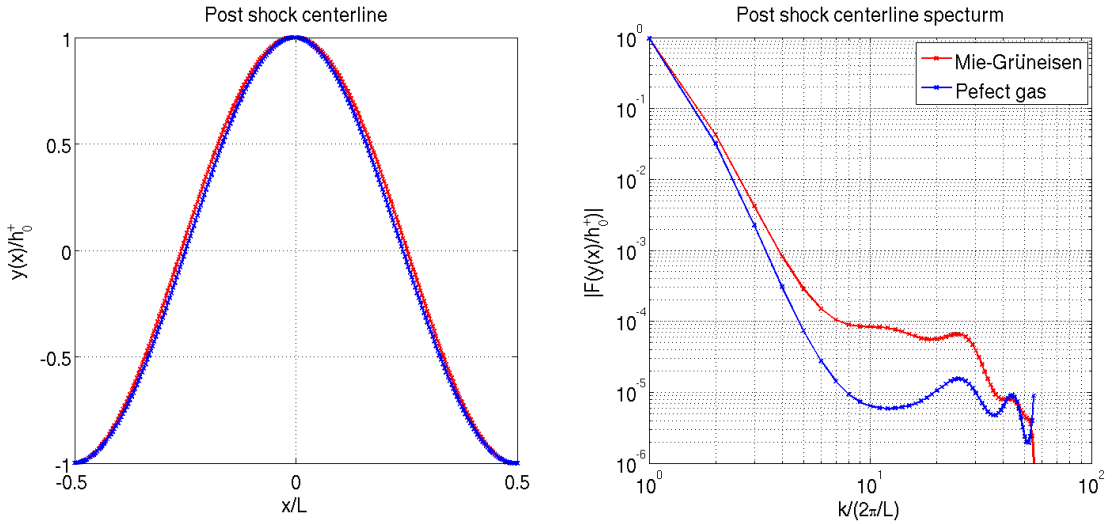

(a) (b)

Figure 4.11: "Light-to-heavy" Mach 1.5 single-mode Richtmyer-Meshkov instability post-shock centerline plot (a) and centerline power spectrum plot (b). Slight variation in shape occurs, however, the post-shock centerlines for both equations of state remain for the most part as a single-mode.

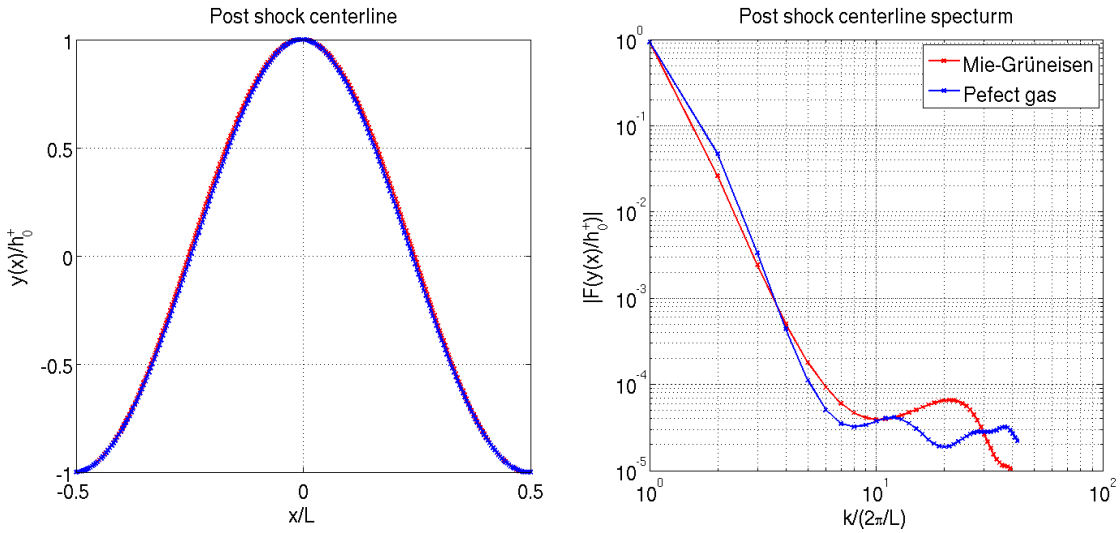

(a) (b)

Figure 4.12: "Light-to-heavy" Mach 2.5 single-mode Richtmyer-Meshkov instability post-shock centerline plot (a) and centerline power spectrum plot (b). The post-shock centerlines for both equations of state remain for the most part as a single-mode.

4.5 "Light-to-heavy" triple-mode

When multiple modes are present, products of variables in the Euler equations can lead to nonlinear reinforcement or interference across modes when two wave numbers sum to a third. One case of triple-mode Richtmyer-Meshkov instability with the mode coupling $k_1 = k_2 + k_3$ where $k_2 = \frac{2}{3}k_1$, $k_3 = \frac{1}{3}k_1$, and $k_1h_1 = k_2h_2 = k_3h_3$ is now examined. As a starting point the wavenumbers from the previous single-mode investigation for k_1 are retained, but with a corrugation amplitude that is 2% of the wavelength. Tabulation of the three initial wavelengths and associated amplitudes are given in table 4.6 for MORB-molybdenum and perfect gas simulations. Figure 4.13 shows density

MORB-molybdenum

M_s	k_1h_1	k_2/k_1	k_3/k_1
2.5	0.04π	2/3	1/3

Perfect gas

M_s	k_1h_1	k_2/k_1	k_3/k_1
1.87	0.025π	2/3	1/3

Table 4.6: Initial conditions for triple-mode Richtmyer-Meshkov instability in the "light-to-heavy" case for Mie-Grüneisen and perfect gas equations of state

gradient magnitude contours for the present triple-mode case and matched perfect gas. Again, the amplitude of the mixing layer for the perfect gas cases is seen to lag behind that of the corresponding MORB-molybdenum cases. Consequently roll-up is delayed in time as well.

(a)

(b)

(c)

Figure 4.13: "Light-to-heavy" MORB-molybdenum Mach 2.5 triple-mode Richtmyer-Meshkov instability schlieren plots and equivalent perfect gas plots for nondimensional times 5.31, 10.6, and 15.9

4.5.1 Amplitude and growth rate

The mixing layer amplitude and growth rate are given in Figure 4.14. A variation in start-up time of the same order of magnitude as in the single-mode case is again observed. A similar order of magnitude variation in growth rate oscillations is also observed. However, three distinct oscillation frequencies are now observed, associated with the three different wavelengths of the corrugation. Tabulation of frequency values is given in table 4.7. Strong correlation is observed between the observed oscillation frequencies and predicted values from the associated zero-corrugation problem.

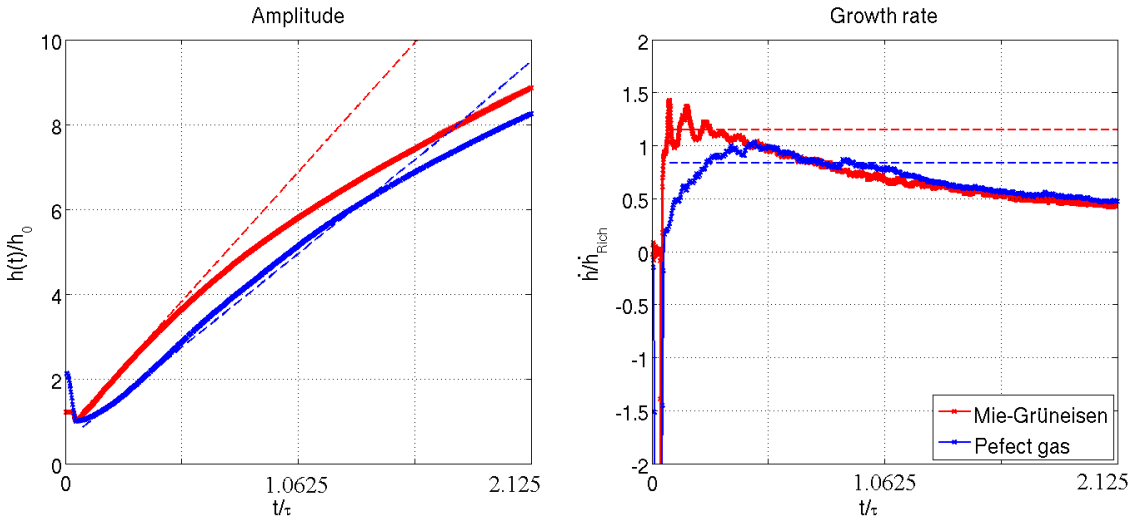

(a) (b)

Figure 4.14: "Light-to-heavy" Mach 2.5 triple-mode Richtmyer-Meshkov instability amplitude growth plot (a) and amplitude growth rate plot (b). A start-up time difference is clearly observable between the MORB-molybdenum and perfect gas case. Post-start-up oscillations in growth rate for MORB-molybdenum are at much greater frequency and amplitudes than those of the perfect gas.

	MORB-molybdenum	Perfect gas
$\tau f_{R1_{1D}}$	3.80	0.433
$\tau f_{T1_{1D}}$	2.39	0.245
$\tau f_{1_{2D}}$	3.61	0.371
$\tau f_{R2_{1D}}$	2.54	0.288
$\tau f_{T2_{1D}}$	1.59	0.163
$\tau f_{2_{2D}}$	2.41	0.213
$\tau f_{R3_{1D}}$	1.27	0.144
$\tau f_{T3_{1D}}$	0.80	0.082
$\tau f_{3_{2D}}$	1.26	0.143

Table 4.7: Dominant growth rate oscillation frequencies $f_{2D}\tau$ for "light-to-heavy" triple-mode Richtmyer-Meshkov instability and approximate perturbed transmitted and reflected shock oscillation frequency, $f_{T1D}\tau$ and $f_{R1D}\tau$, respectively, based on solution to the zero-corrugation Riemann problem

4.6 "Heavy-to-light" single-mode

Presently the single-mode "heavy-to-light" case is investigated. Again MORB and molybdenum are used for the materials with Mie-Grüneisen equation of state and air and SF6 as a starting point for perfect gases. Mach numbers of 1.5 and 2.5 for the MORB and molybdenum case provide the basis for comparison in parameter space for the "heavy-to-light" case as well. For the Mach 1.5 case a 5% of the wavelenth initial corrugation amplitude was taken as well. For the Mach 2.5 case, due to the large compression of the corresponding perfect gas case interface by the shock that would result, a smaller amplitude of 2% of the wavelenth was taken. Tabulation of these initial conditions and relevant post-shock quantites for zero-corrugation are found in Table 4.8. Again, the unshocked prefect gases are taken to be at approximately room temperature and pressure (T=300 K, p=1 atm). Likewise, the unshocked Mie-Grüneisen fluids are in thermodynamic equilibrium at (ρ_0, p_0), repsectively. The entries for MORB and molybdenum are tabulated below, including initial and post-shock conditions as well as properties for the corresponding matched perfect gas cases. Figure

molybdenum-MORB

M_s	$\Delta p/\rho_0 c_0^2$	kh_0	A^-	A^+
1.5	1.049	0.10π	-0.578	-0.437
2.5	5.245	0.04π	-0.578	-0.446

Perfect gas

M_s	$\Delta p/\rho_0 c_0^2$	kh_0	A^-	A^+
1.244	1.049	0.11π	-0.420	-0.437
1.934	5.245	0.095π	-0.391	-0.446

Table 4.8: Initial conditions for single-mode Richtmyer-Meshkov instability in the "heavy-to-light" case for Mie-Grüneisen and perfect gas equations of state

Perfect gas

M_s	γ_1	c_{v_1}	γ_2	c_{v_2}
1.244	1.248	$7.17 kJ/kgK$	1.09	$7.17 kJ/kgK$
1.934	1.248	$7.17 kJ/kgK$	1.09	$8.65 kJ/kgK$

Table 4.9: Perfect gas properties for single-mode Richtmyer-Meshkov instability in the "heavy-to-light" case

4.15 (a) shows density gradient magnitude contours for the Mach 1.5 case and matched perfect gas respectively. Figure 4.15 (b) shows density gradient magnitude contours for the Mach 2.5 case and matched perfect gas. A greater deal of variation in shape is observed from one case to another for the "heavy-to-light" cases, particularly at the higher Mach number, which demonstrates a wider spike.

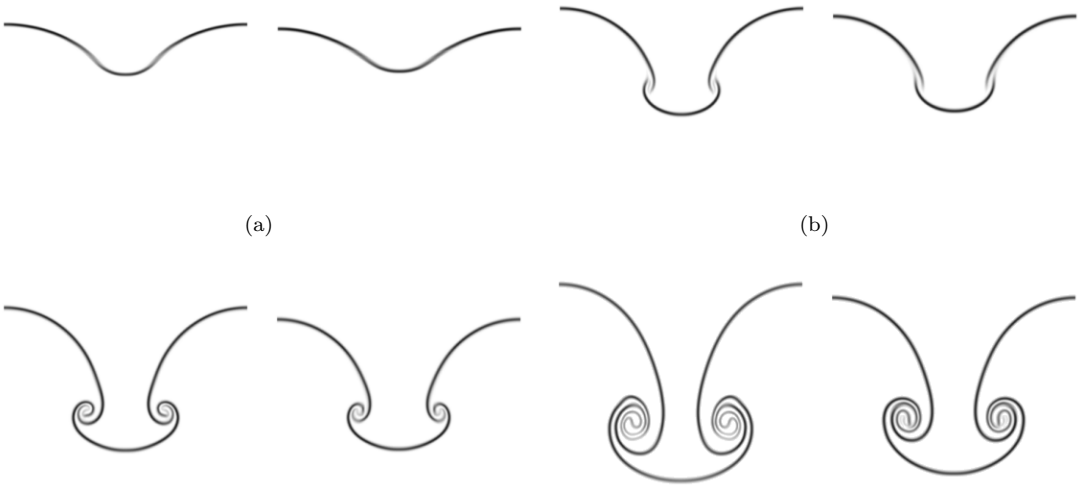

(a) (b)

(c) (d)

Figure 4.15: "Heavy-to-light" MORB-molybdenum (left) and equivalent perfect gas (right) single-mode Richtmyer-Meshkov instability schlieren plot comparison for Mach 1.5 incident shock at nondimensional times (a) 3.01, (b) 6.02, (c) 9.02, and (d) 15.04

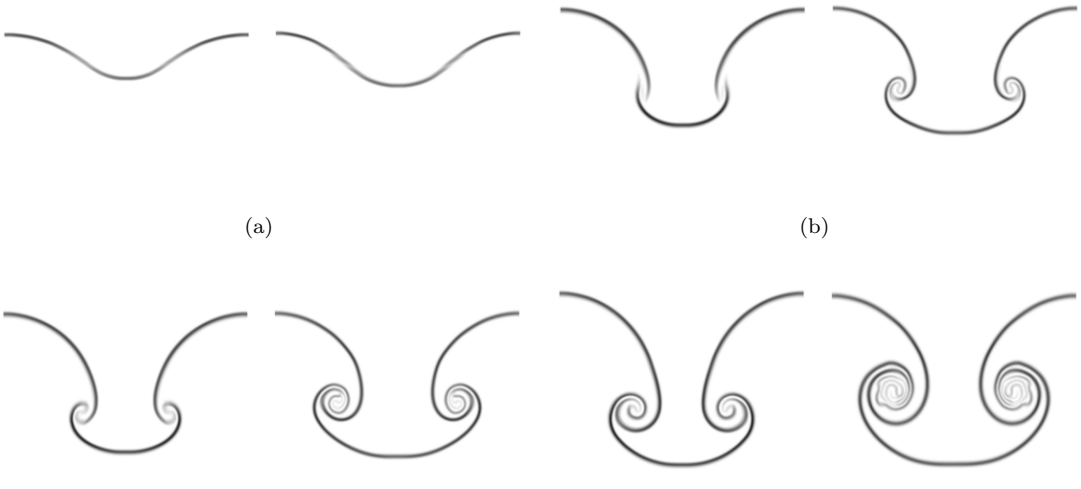

(a) (b)

(c) (d)

Figure 4.16: "Heavy-to-light" MORB-molybdenum (left) and equivalent perfect gas (right) single-mode Richtmyer-Meshkov instability schlieren plot comparison for Mach 2.5 incident shock at nondimensional times (a) 7.9, (b) 23.71, (c) 31.41, and (d) 47.22

4.6.1 Amplitude and growth rate

Figures 4.5 and 4.5 display nondimensionalized results for Mach 1.5 and 2.5 Richtmyer-Meshkov instability respectively for the MORB-molybdenum "heavy-to-light" case and associated perfect gas matching. The growth rate plots have been scaled by the alternative prediction [54],

$$\dot{h}_\infty = \frac{1}{2}(h_0^- + h_0^+)kA^+\Delta v, \tag{4.26}$$

which gives better agreement. Unlike the "light-to-heavy" case, a much higher degree of similarity is observed in the features of the growth plots. The most notable difference is that the peak growth rate attained by the perfect gases is considerably less than those of the MORB-molybdenum. Start-up time and growth rate oscillations are all similar in magnitude. Evidently the wavenumber required to yield a matching of growth rate correlates directly to wave speed for the present case. Again, the linear growth regime is not distinctly evident in the present growth rate plots. Just as in the "light-to-heavy" case, the decay in growth rate deviates between equations of state more as the strength of the shock increases, MORB-molybdenum demonstrating a higher decay rate. This is in part due to the larger compression of the perfect gas interface requiring a bigger h_0^- to obtain similar h_0^+k values, thus yielding a larger linear growth rate for the perfect gas by the prediction of equation (4.26).

MORB-molybdenum

M_s	$\tau f_{T_{1D}}$	$\tau f_{_{2D}}$
1.5	1.21	1.21
2.5	1.20	0.49

Perfect gas

M_s	$\tau f_{T_{1D}}$	$\tau f_{_{2D}}$
1.244	1.26	1.22
1.934	0.42	0.38

Table 4.10: Growth rate oscillation frequency $f_{_{2D}}$ for "heavy-to-light" Richtmyer-Meshkov instability and approximate perturbed transmitted shock oscillation frequency $f_{T_{1D}}$ based on solution to the zero-corrugation Riemann problem

4.6.2 Integral vorticity

Examination of the vorticity distribution for the "heavy-to-light" case shortly after shock-contact interaction is now presented. Figures 4.19 and 4.20 display normalized vorticity distributions and associated power spectrum shortly after shock interaction for MORB-molybdenum Mach 1.5 and 2.5 Richtmyer-Meshkov instability and corresponding perfect gas cases of matched initial conditions respectively. Just as in the "light-to-heavy" case, the vorticity distribution exhibits the behavior of a sinusoidal distribution with a single-mode to within roughly 15%.

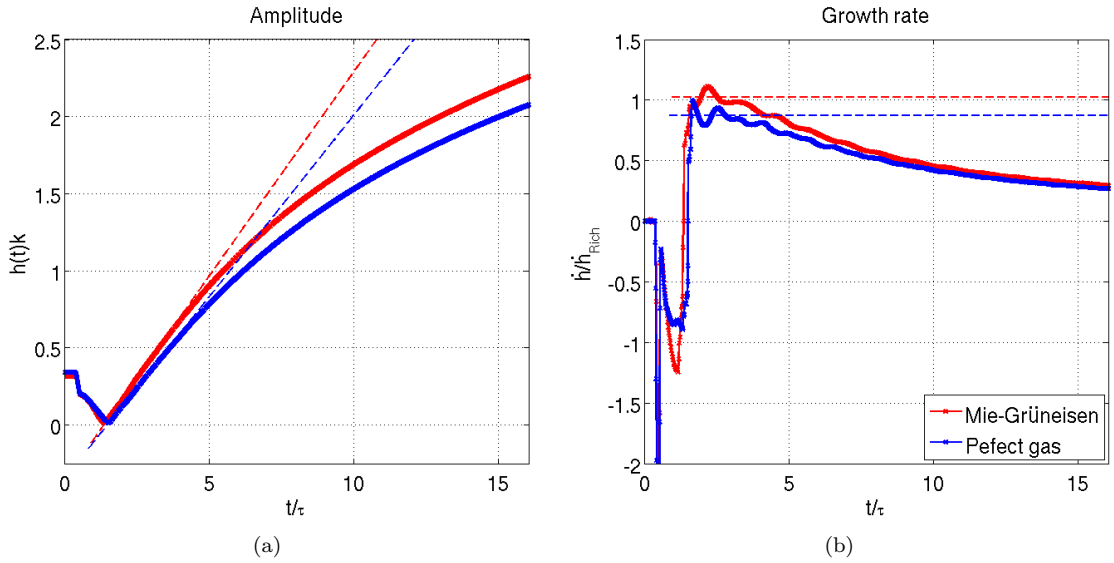

(a) (b)

Figure 4.17: "Heavy-to-light" Mach 1.5 single-mode Richtmyer-Meshkov instability amplitude growth plot (a) and amplitude growth rate plot (b). The plots show a greater level of similarity than the "light-to-heavy" case. Start-up times are observed to be on the same order of magnitude. Post-start-up oscillations in growth rate also demonstrate similar frequencies and amplitudes.

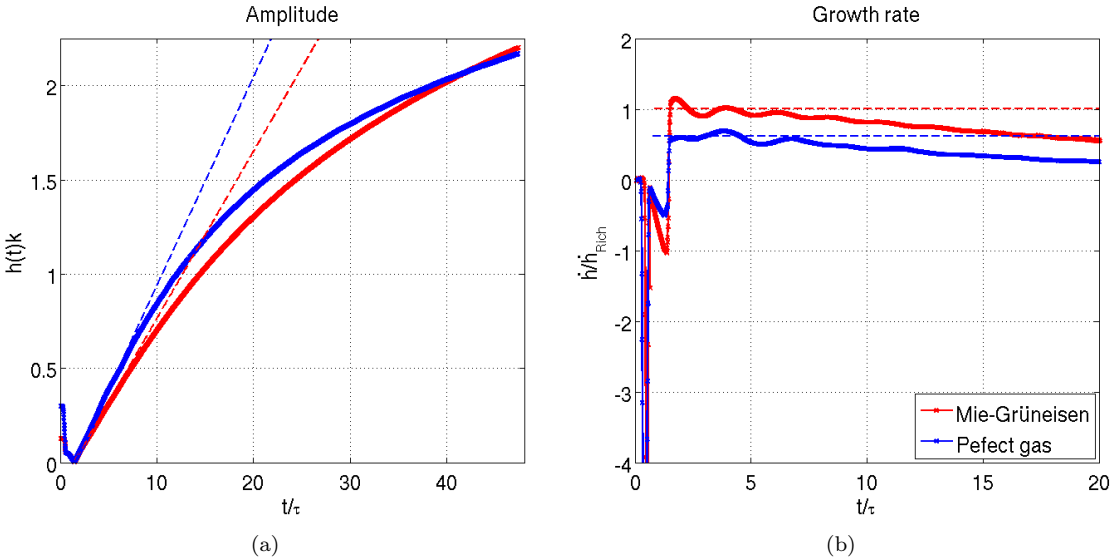

(a) (b)

Figure 4.18: "Heavy-to-light" Mach 2.5 single-mode Richtmyer-Meshkov instability amplitude growth plot (a) and amplitude growth rate plot (b). Again, start-up times are observed to be on the same order of magnitude. Post-start-up oscillations in growth rate also demonstrate similar frequencies and amplitudes.

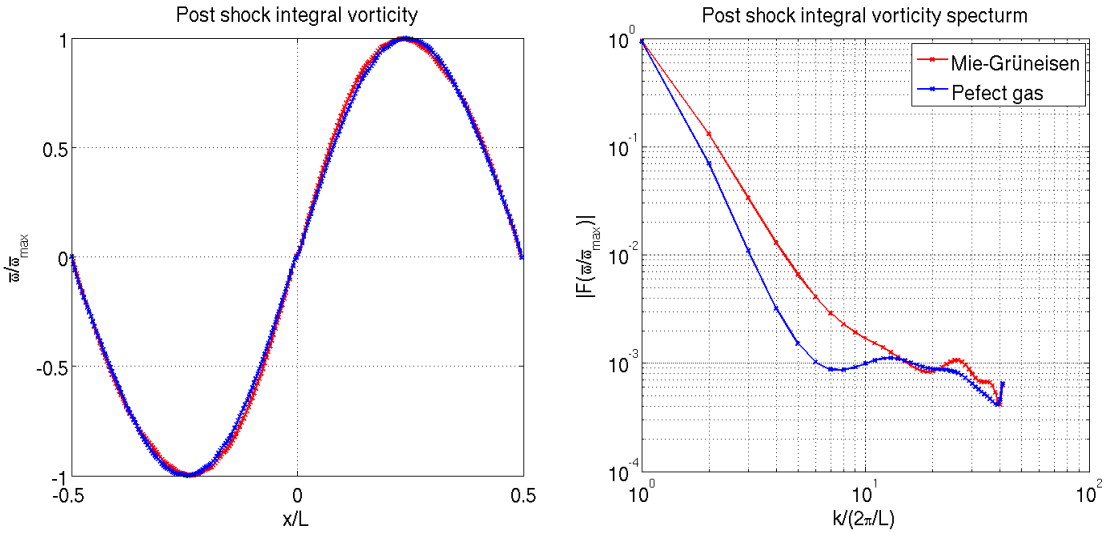

(a) (b)

Figure 4.19: "Heavy-to-light" Mach 1.5 single-mode Richtmyer-Meshkov instability post-shock integral vorticity plot (a) and integral vorticity power spectrum plot (b). Significant change is observed between equations of state due to the nature of the Hugoniot.

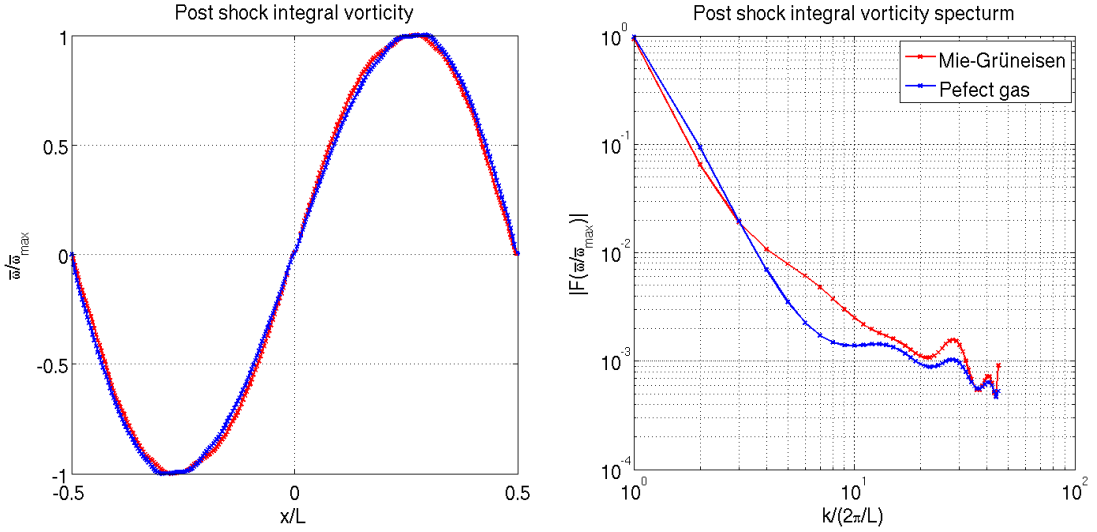

(a) (b)

Figure 4.20: "Heavy-to-light" Mach 2.5 single-mode Richtmyer-Meshkov instability post-shock integral vorticity plot (a) and integral vorticity power spectrum plot (b). Significant change is observed between equations of state due to the nature of the Hugoniot

4.6.3 Post-shock centerline

Examination of the centerlines for the "heavy-to-light" case post-shock yields similar results to the "light-to-heavy" case. Figures 4.21 and 4.22 display normalized centerline plots and associated power spectrum shortly after shock interaction for MORB-molybdenum Mach 1.5 and 2.5 Richtmyer-Meshkov instability and corresponding perfect gas cases of matched initial conditions. The centerlines remain as a single-mode to within roughly 5%.

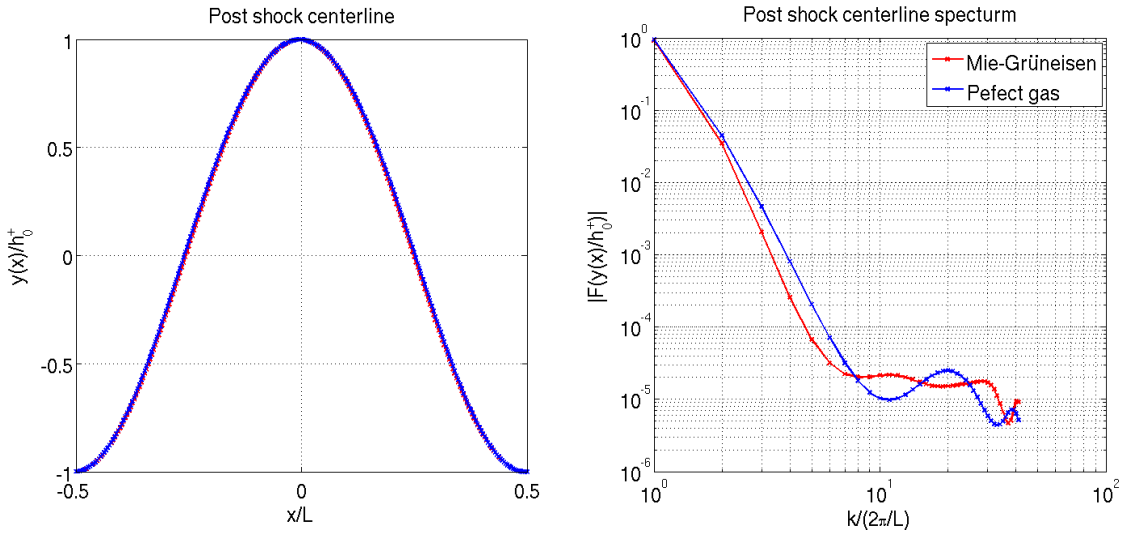

(a) (b)

Figure 4.21: "Heavy-to-light" Mach 1.5 single-mode Richtmyer-Meshkov instability post-shock centerline plot (a) and centerline power spectrum plot (b). Slight variation in shape occurs, however, the post-shock centerlines for both equations of state remain for the most part as a single-mode.

4.6.4 Incipient weak shock waves

Figure 4.23 gives density contour plots at several different times for "heavy-to-light" Mach 1.5 Richtmyer-Meshkov instability in MORB-molybdenum. Clearly evident in the contour plots is a transmitted shock and reflected expansion wave. However, an additional and somewhat unexpected series of shock waves is observed to form within the region of the expansion fan. These shock waves first form along the boundary and propagate away from the corrugation. A somewhat analogous phenomenon has been observed in Rayleigh-Taylor instability [61]. For Rayleigh-Taylor instability, Olson and Cook observed that the acceleration of an interface driven by a constant gravitational field generated shocklets, much in the same way a piston does, which eventually catch up to one another to form a weak shock. Presently, in "heavy-to-light" Richtmyer-Meshkov instability, the formation of incipient weak shock waves generated by oscillations in the difuse material contact are observed. It is evident that waves produced by the perturbed transmitted shock cause oscillations

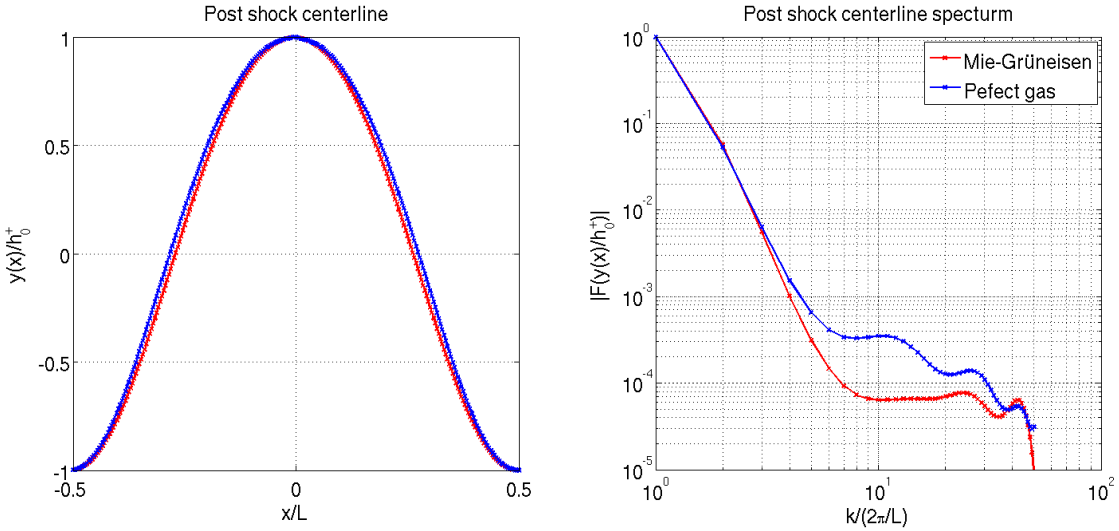

(a) (b)

Figure 4.22: "Heavy-to-light" Mach 2.5 single-mode Richtmyer-Meshkov instability post-shock centerline plot (a) and centerline power spectrum plot (b). The post-shock centerlines for both equations of state remain for the most part as a single-mode.

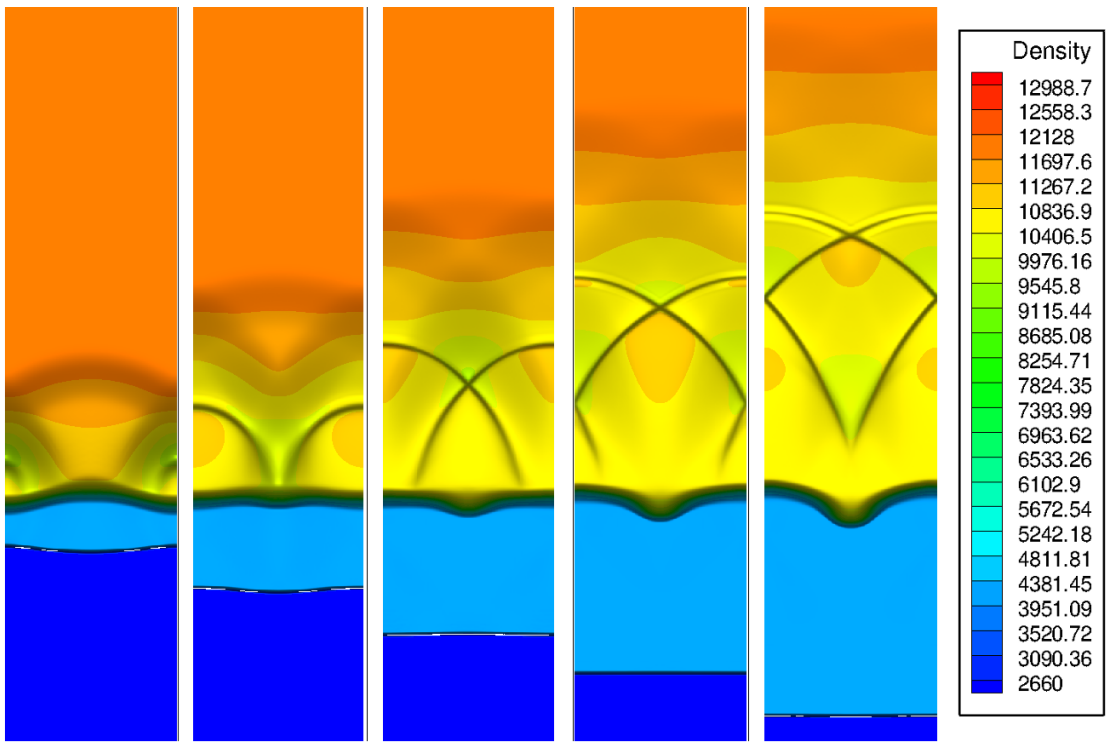

Figure 4.23: Density contours showing the formation of incipient weak shock waves for Richtmyer-Meshkov instability in MORB-molybdenum modeled by Mie-Grüneisen equations of state for Mach 1.5 in the "heavy-to-light" case. At early times the transmitted shock and reflected expansion are clearly visible. Formation of the incipient weak shock waves begins along the edge.

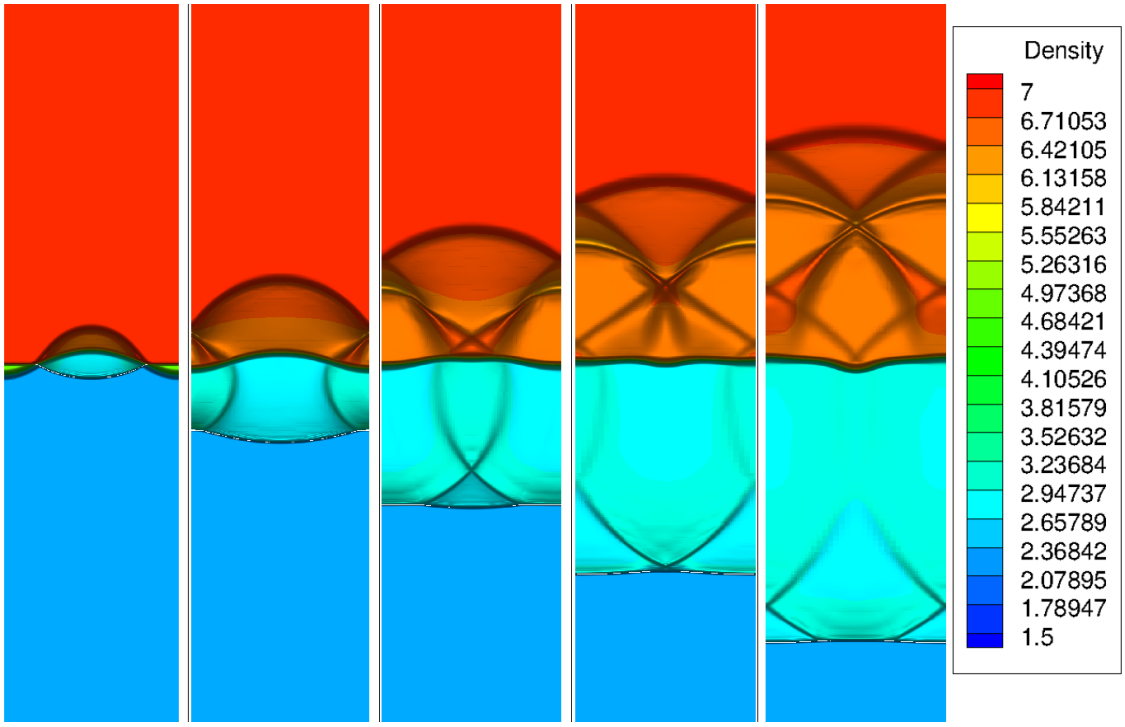

Figure 4.24: Density contours showing the formation of incipient weak shock waves for Richtmyer-Meshkov instability in fluids with perfect gas equations of state for Mach 1.244 in the "heavy-to-light" case. At early times the transmitted shock and reflected expansion are clearly visible. Formation of the incipient weak shock waves begins along the edge.

in the shape of the interface centerline. In the present case of "heavy-to-light" Ricthmyer-Meshkov instability the strength of these oscillations is strong enough to generate noticeably strong shocks within the heavy material for both Mach 1.5 and 2.5 cases. A similar set of incipient weak shock waves is observable for the corresponding perfect gas cases, as seen in Figure 4.24 for a 5% intial corrugation amplitude. The formation of several incipient weak shock waves is clearly observable.

Chapter 5

Level-set, ghost cell methodology

In the following sections an Eulerian, Cartesian mesh, ghost fluid methodology is developed for single-phase impact-driven flows with free surfaces. The methodology utilizes a level-set to define the location of the material-vacuum interface. Ghost cells are interpolated based on surface normal Riemann problems along gradient trajectories of the signed distance function [8, 83]. Flux reconstruction along each Cartesian direction of the domain is achieved by subdividing in a way that allows for robust treatment of grid-scale sized voids. Additionally, introduced is a two-variable approach to the reinitialization of the distance function from the level-set which leaves the material boundary defining zero level-set essentially intact. Implementation of the code in parallel with adaptive mesh refinement (AMR) is performed in California Institute of Technology's VTF (Virtual Test Facility) AMROC [15–17]. Results for several impact-driven flows in vacuum of interest are given in one and two dimensions to demonstrate the methodology for fluids with Mie-Grüneisen equation of state. First, in one dimension an impact problem involving two finite length aluminum slabs is examined. Next, a similar three-dimensional axisymmetric impact problem involving aluminum rods is demonstrated. Lastly, the axisymmetric impact of a sphere and plate is examined.

5.1 Level-set

level-sets provide a simple way to define an arbitrarily complex surface by a scalar in an Eulerian setting. The level-set scalar is evolved by the linear advection equation

$$\frac{\partial \phi}{\partial t} + \vec{\mathbf{u}} \cdot \vec{\nabla} \phi = 0, \tag{5.1}$$

allowing for the natural splitting of isocontours which can be utilized to define material regions. Presently, for the purpose of simulating flows with fluid-vacuum interfaces, fluid and vacuum regions

of a single-phase flow are defined by a scalar ϕ, where

$$\phi < 0, \quad vacuum, \tag{5.2}$$

$$\phi = 0, \quad interface, \tag{5.3}$$

$$\phi > 0, \quad material. \tag{5.4}$$

The advection of the zero level-set is therefore of critical importance to such a level-set method.

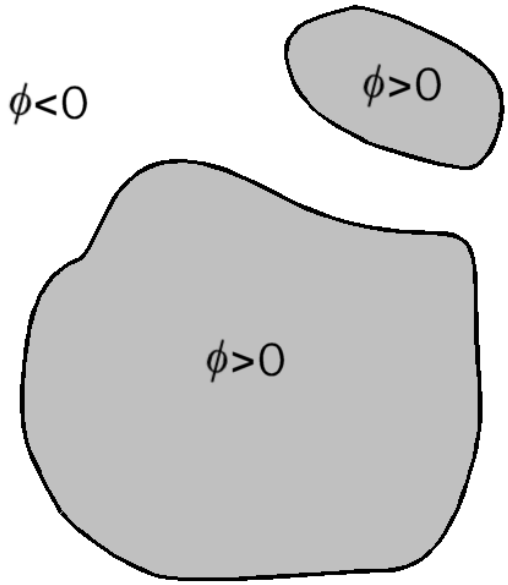

Figure 5.1: Schematic of level-set definition for fluid-vacuum interface problems

5.1.1 Ghost cells

The assignment of ghost cell values in a narrow band outside of a free surface should at a minimum provide an approximation to the proper traction conditions. It was initially proposed by Fedkiw [22] that the signed distance function should be utilized to apply the proper traction conditions at an interface between two materials. For a given fluid region defined by a level-set the entropy and velocity field are extrapolated along tangent curves of the signed distance function. The final conservative ghost fluid vector of state is given by enforcing the pressure of the contacted material. The method was initially applied to ideal gas law fluids. For a general fluid, such as those defined by Mie-Grüneisen equation of state, or even a solid, it is not in general useful to extrapolate entropy which may not be simply extracted. Instead it is more practical to utilize approximate Riemann problem solutions [7, 8], analogous to using an isentrope which is an approximate solution Riemann

problem solution to third-order in entropy [85]. For each ghost cell, as in Figure 5.2, a tangent path to the signed distance function is traced out to the location of the free surface,

$$\vec{\mathbf{x}}_s = \vec{\mathbf{x}}_{i,j} + \int_{\phi_{i,j}}^{0} \vec{\mathbf{n}}(s)ds, \tag{5.5}$$

where

$$\vec{\mathbf{n}}(s) = \frac{\vec{\nabla}\phi}{\|\vec{\nabla}\phi\|}. \tag{5.6}$$

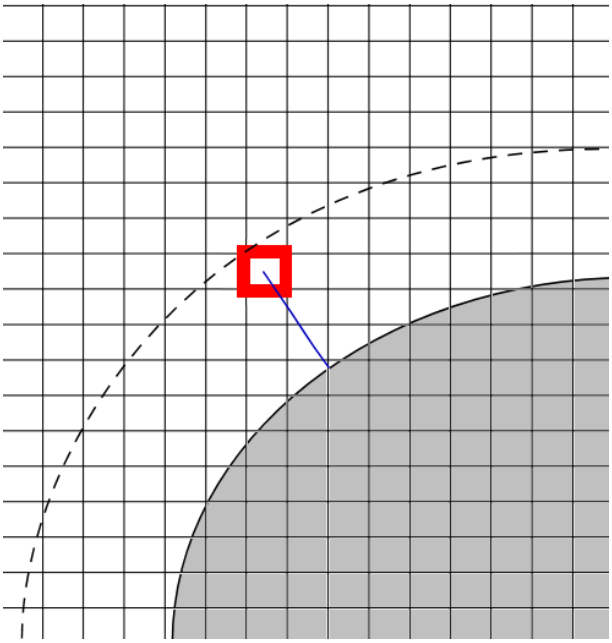

Figure 5.2: Schematic of a ghost cell band and its tangent path to a free surface

Numerically this path integration is carried out by an adaptive stepping third-order Runge-Kutta integration with the bilinear interpolation of the gradient of ϕ. The differential step ds is taken to be

$$ds = min(3\Delta x/4, max(|\phi|, \Delta x/10)), \tag{5.7}$$

with integration complete upon reaching a value of ϕ greater than zero. Once the surface is reached an interpolation of the conserved vector of state is performed by weighted bilinear interpolation to give an approximation to the state locally. The surface normal, defined by the gradient in the signed distance function, is then utilized to decompose the momentum state into a local coordinate system for determining a Riemann problem solution. This Riemann problem solution is then assigned to the ghost cell.

5.1.1.1 Riemann solver

For most fluids the solution to the Riemann problem between left and right states is comprised of compressive shock wave discontinuities, isentropic expansion waves, and contact discontinuities [47, 85]. A valid solution must yield a common pressure and velocity across the shock and expansion waves connecting left and right states. The locus of states accessible by expansion or compression is known as a Hugoniot. It is useful to think of this Hugoniot in terms of velocity and pressure in order to meet the matching constraint from left and right states. Figure 5.3(a) depicts left and right state velocity-pressure Hugoniot with intersection defining the appropriate solution. The related Riemann problem solution wave diagram in space and time is shown in Figure 5.3(b) composed of leftward traversing shock and contact discontinuity and rightward expansion wave.

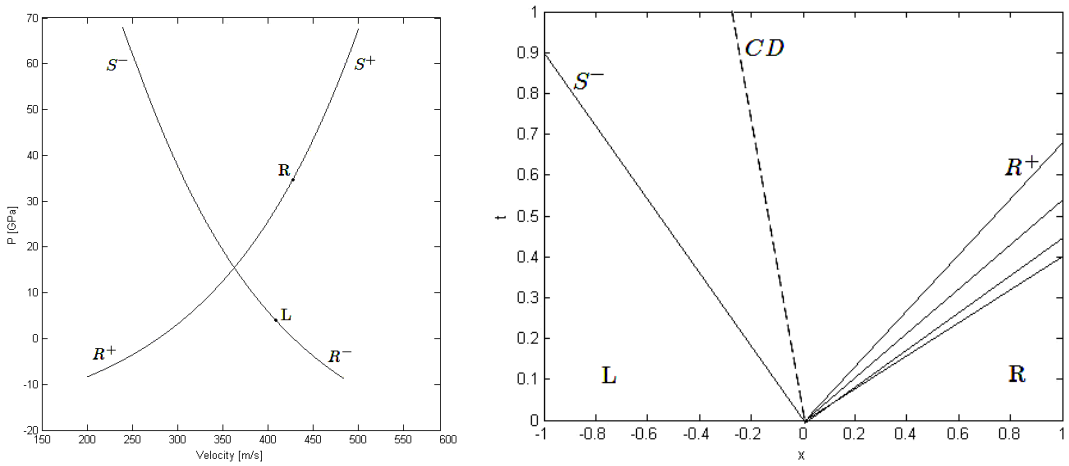

(a) (b)

Figure 5.3: Schematic of a Riemann problem solution consisting of shock and expansion waves

Analytically the shock branch of the Hugoniot of states can be described by a transcendental equation derived from Rankine-Hugoniot jump conditions,

$$e_{cd} = e_{R/L} + \frac{1}{2}(p_{cd} + p_{R/L})(1/\rho_{cd} - 1/\rho_{R/L}), \tag{5.8}$$

and

$$u_{cd} = u_{R/L} \pm \sqrt{(p_{cd} - p_{R/L})(1/\rho_{R/L} - 1/\rho_{cd})}. \tag{5.9}$$

Alternatively, the expansion branch of the Hugoniot is described by integral equations

$$u_{cd} = u_{R/L} \pm \int_{p_{R/L}}^{p_{cd}} \frac{1}{\rho c} dp', \tag{5.10}$$

and

$$\rho_{cd} = \rho_{R/L} + \int_{p_{R/L}}^{p_{cd}} \frac{1}{c} dp'. \tag{5.11}$$

For most fluid equations of state no analytic solution to the Riemann problem is attainable. Solution must therefore be performed numerically by root finding for the intersection of the Hugoniot. Additionally, it may be necessary to use root finding to produce the shock-branch and integration quadrature for the expansion-branch of each Hugoniot. Solving the Riemann problem can therefore be a relatively expensive computational procedure. Fortunately for a Godunov-style numerical solver applied to many flows of interest, it is in general unnecessary to solve the Riemann problem to numerical precision to approximate fluxes at midpoints.

5.1.1.2 Linearized Riemann solver

A variety of simple low-order approximations to Riemann problem solutions have proven to be, for many flows of interest, a practical alternative to full solutions for Godunov solvers [13, 45, 46, 72, 86, 87]. Presently, two approaches are used for approximating the Riemann problem solution. The first is a simple linear $p - u$ approximation to the Hugoniot introduced by Colella [13],

$$p_{cd} = p_{L/R} \pm \rho_{L/R} a_{L/R} (u_{cd} - u_{L/R}). \tag{5.12}$$

From this simple linear Hugoniot approximation can be obtained an expression for u_{cd} and p_{cd} strictly in terms of left and right state quantities,

$$u_{cd} = \frac{\rho_R u_R a_R + \rho_L u_L a_L}{\rho_R a_R + \rho_L a_L}. \tag{5.13}$$

Density along the Hugoniot can be approximated by the linear equation

$$\rho_{cd} = \rho_{L/R} + (p_{cd} - p_{L/R})/a_{L/R}^2. \tag{5.14}$$

This simple solver is relatively robust for moderate shock strengths and is applied to the first two test problems examined. Such an approximation can be considered as a single step of a Newton-Raphson root finding approximation to the Hugoniot intersection problem. It is noteworthy that for problems involving a free surface the value of $p_{cd} = 0$ is a given. This reduces the computational cost of solving the full Riemann problem by more than half that of a two-material problem where p_{cd} is an unknown. For the vacuum case when $p_{L/R} > 0$ it is then only necessary to perform a simple numerical integration of equations (5.10) and (5.11). Again, in practice it is not necessary to have a solution to numerical precision. Instead, a limited number of integration steps can be utilized to give a higher-order approximation, useful for stronger expansions. Similarly, for cases with $p_{L/R} < 0$ a

higher-order approximation to the Riemann problem solution can be obtained by applying a limited number of root finding steps. Utilizing Secant root finding and third-order Runge-Kutta integration, this higher-order approach is applied to the third test problem examined of a sphere-plate impact.

5.1.2 Level-set reinitialization

The use of a the signed distance function to define ghost cells in the previous section presents an additional complication. In general the level-set does not carry any additional meaning besides defining regions by a sign change. However, since the signed distance function is utilized in defining ghost cells it becomes natural to use the level-set scalar to carry this information. Unfortunately the linear advection equation does not constrain the level-set scalar to satisfy the Eikonal equation for all time as a signed distance function should. It is therefore an important part of level-set methods to periodically reinitialize the level-set into a true distance function which satisfies the Eikonal equation [26, 64, 75, 83],

$$\|\overrightarrow{\nabla}\phi\| = 1. \tag{5.15}$$

Presently, to achieve a level-set which satisfies the above constraint, a modified version of the artificial time marching differential equation based reinitialization of Russo and Smereka [75] is introduced. Sussman [83] first introduced the concept of differential equation based reinitialization, utilizing the Hamilton-Jacobi differential equation

$$\frac{\partial\phi}{\partial\tau} + S(\phi_0)(\|\overrightarrow{\nabla}\phi\| - 1) = 0 \tag{5.16}$$

which tends to the unique viscosity solution of the Eikonal equation as τ approaches infinity. For numerical purposes $S(\phi_0)$ is a smoothed out sign function of the initial condition defined by

$$S(\phi_0) = \frac{\phi_0}{\phi_0^2 + \epsilon^2} \tag{5.17}$$

with ϵ given by the grid length scale. For a first-order continuous zero level-set, reinitialization numerically by this approach directly can yield a shift of the location of the zero level-set on the order of the grid length scale. Furthermore, at corners in the zero level-set the location is significantly rounded and shifted. For situations where the level-set is advected only a fraction of the grid length scale over long periods of time the approach is therefore inadequate when applied repeatedly. A good numerical reinitialization should shift the location of the zero level-set by as little as possible. Russo [75] introduced a modified version of the approach which used a one-sided direct calculation of distance for points near the level-set. Hartmann et al. [26] introduced a more sophisticated numerical approach to constrain the location of the zero level-set.

Presently, a modified version of the work in [75] is introduced. The current method utilizes a two-

variable approach. The first variable, denoted here by ψ, is never reinitialized and initially contains the same zero level-set as the distance function but is an otherwise meaningless scalar advected by the physical flow field,

$$\frac{\partial \psi}{\partial t} + \vec{\mathbf{u}} \cdot \vec{\nabla} \psi = 0. \tag{5.18}$$

The second variable, denoted here by ϕ, is the level-set which is advected physically by equation (5.18) as well, but is reinitialized periodically to the distance function by solution to differential equation in artificial time τ. The function ψ is utilized to tie down the zero level-set for the numerical method. The numerical approach is defined as follows:

$$\frac{d\phi_{i,j}}{dt} = \begin{cases} \frac{1}{2} \frac{(|S(\phi_{i,j})|+|S(d_{i,j})|)(d_{i,j}-\phi_{i,j})}{\vec{\mathbf{\Delta x}} \cdot \vec{\nabla} \psi_{i,j} / \|\vec{\nabla} \psi_{i,j}\|} & \text{if } (x_i, y_j) \text{ on } \Gamma, \\ S(\phi_{i,j})(1 - \|\vec{\nabla} \phi_{i,j}\|) & \text{otherwise.} \end{cases} \tag{5.19}$$

Here Γ is used to denote points nearest to the zero level-set that are positive in value of ψ. Applying the the direct distance calculation to only one side of the interface alleviates over constraining which may lead to inconsistencies. The value $d_{i,j}$ is given by a direct approximation to the distance of such points,

$$d_{i,j} = \frac{\psi_{i,j}}{\|\vec{\nabla} \psi_{i,j}\|}. \tag{5.20}$$

Evaluation of $\|\vec{\nabla} \psi_{i,j}\|$ numerically requires special consideration. At smooth first-order continuous features in the level-set contour a high-order approximation is desirable. Alternatively, at corners and cusps a low-order approximation is best. Therefore the approximation of $\|\vec{\nabla} \psi_{i,j}\|$ is taken as the maximum of the central slope limiter of Van Leer [88] and

$$\frac{|\psi_{i+l,j+k} - \psi_{i,j}|}{\sqrt{(l\Delta x)^2 + (k\Delta y)^2}}, \quad \forall \quad l,k = -1,0,1 \quad with \quad \psi_{i+l,j+k}\psi_{i,j} \leq 0. \tag{5.21}$$

Evaluation of $\|\vec{\nabla} \phi_{i,j}\|$ is performed by the methods described in [63] using a fifth-order WENO scheme [37, 48] with third-order Runge-Kutta temporal discretization.

To demonstrate reinitialization of a meaningless scalar field by the means discussed, consider the initial profile

$$\phi(\tau = 0, x, y) = C \tanh(\delta(r - r_0)), \tag{5.22}$$

which has the zero isocontour of a circle of radius r_0 (see Figure 5.4), but is not the signed distance function for a circle. Figure 5.5 shows the artificial time reinitialization solution after 40, 80, 120, 160, 200, and 240 numerical steps for a uniform mesh of 200x200 points with a CFL of 0.5 on a periodic domain. Initially the scalar values in the flattest regions are rapidly forced away from their true signed distance values. After 240 steps the solution appears to have reached it steady state and resembles the expected cone-shaped solution for the signed distance function of a circle.

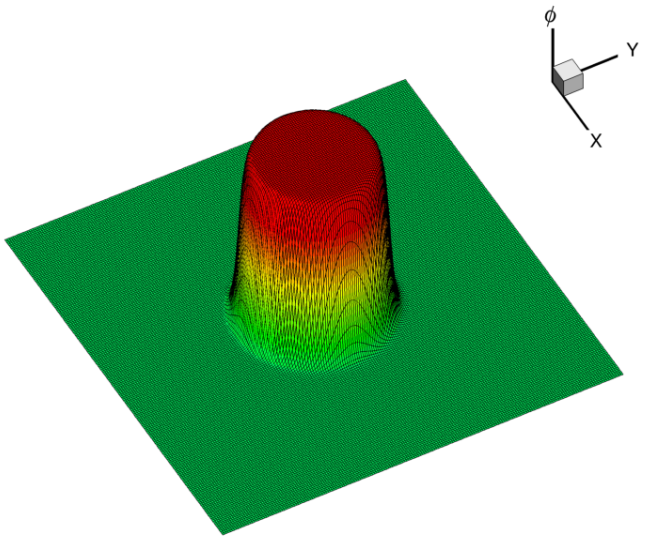

Figure 5.4: Initial conditions utilized for the reinitialization of the distance function for a circle from a meaningless scalar through numerical solution to differential equation for a mesh size is 200x200 points

For practical application to the ghost fluid method it is only necessary to reinitialize points inside of a narrow band around a material interface. For example, for three-dimensional axisymmetric simulation of a sphere-plate impact Figure 5.6 shows the narrow region around the impact reinitialized to the distance function. It is important that the scalar ψ remain continuous to achieve a good approximation to the zero level-set distance. To force ψ to remain continuous an artificial time reinitialization is applied,

$$\frac{\partial \psi}{\partial \tau} + S(\psi)\Big(max\Big(\Big|\frac{\partial \psi}{\partial x}\Big|, \Big|\frac{\partial \psi}{\partial y}\Big|\Big) - 1\Big) = 0, \tag{5.23}$$

for a few points outside of the band of ghost cells utilized.

5.2 Numerical method

The ghost fluid methodology is composed of two separate essential components. The first is the previously discussed management of the reinitialization of the level-set into a signed distance function. This function is performed after a fixed number of advances in real time of the solution for a finite number of iterations in artificial time. The second component is the physical solver which advances the flow in time. Each advance in time of the solution, performed by third-order Runge-Kutta TVD temporal discretization, is essentially composed of two steps. Firstly, the signed distance function is utilized to interpolate ghost cells from surface normal Riemann problem solutions. Secondly,

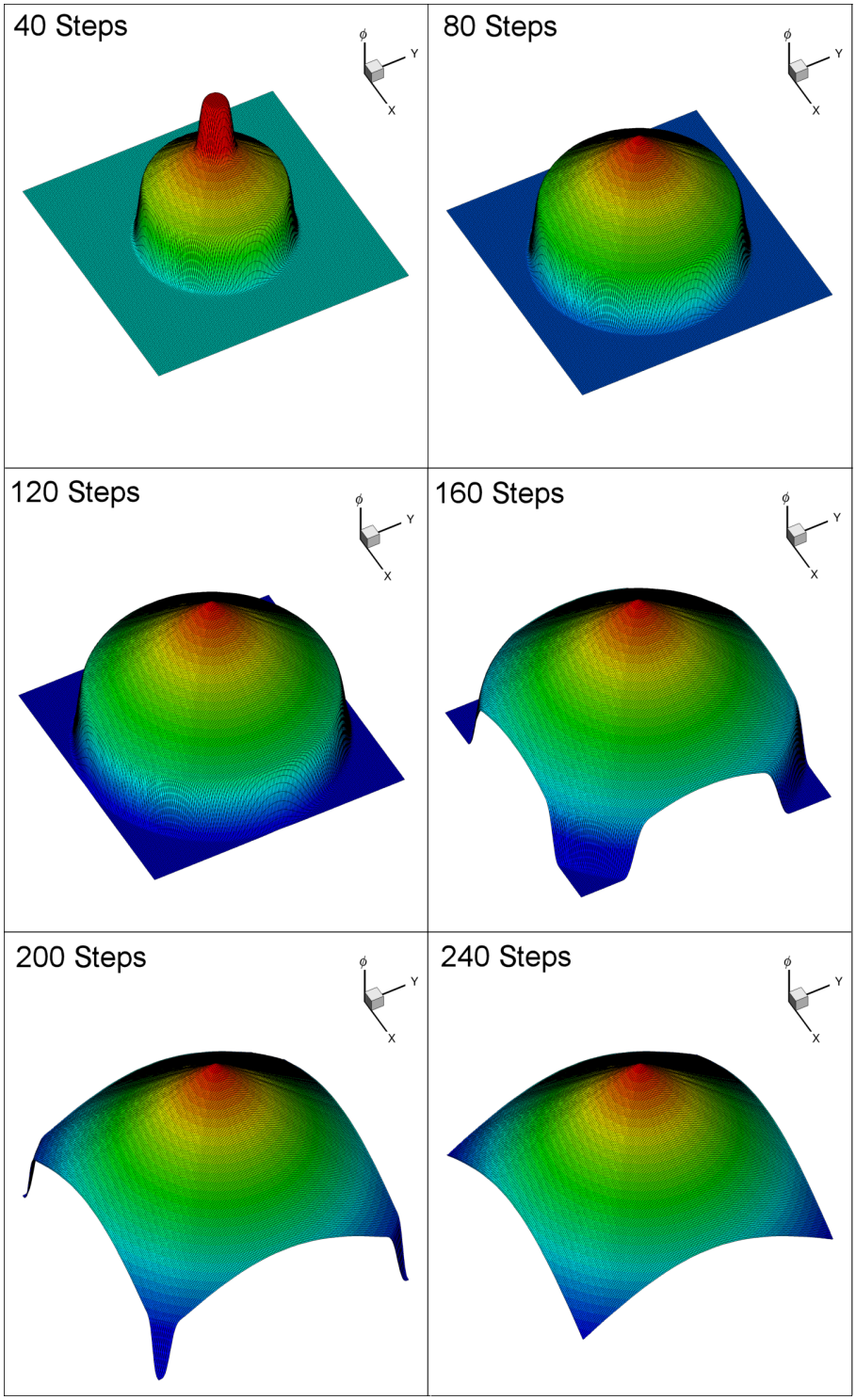

Figure 5.5: Reinitialization of the distance function for a circle from a meaningless scalar through numerical solution to differential equation for a mesh size is 200x200 points. After roughly 240 steps in artificial time the steady-state solution to the Eikonal equation is achieved.

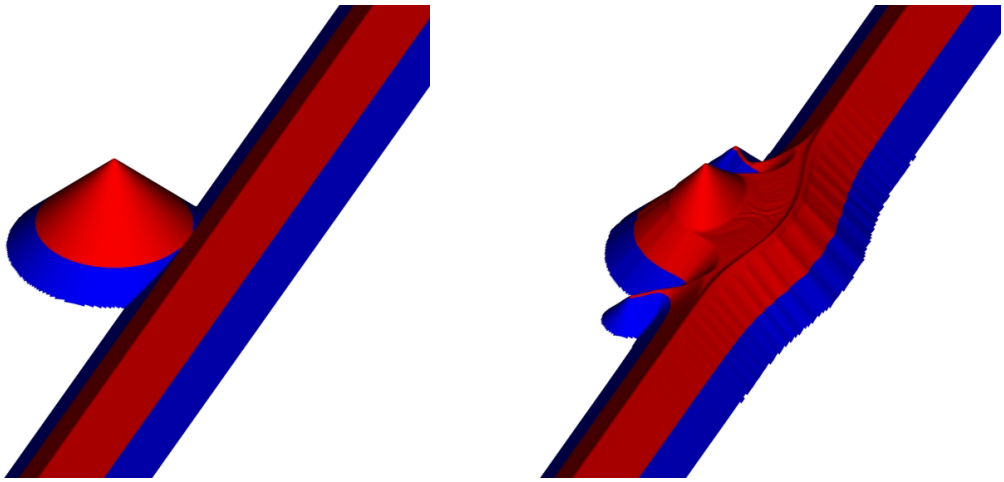

(a) (b)

Figure 5.6: Reinitialization band around fluid-vacuum interface for a sphere-plate impact problem. Initially the level-set is assigned to be the true distance function. Later only a narrow band around the fluid-vacuum interface is maintained as a signed distance.

a reconstruction of fluxes at midpoints must be performed to update each physical cell. Special treatment of near vacuum-fluid interfaces is required to ensure that no waves propagate through the vacuum to a neighboring free surface. The following section describes how this can be achieved in a simple robust manner.

5.2.1 Domain decomposition

The standard reconstruction of midpoint fluxes along a given direction is inadequate for situations where gradients in the level-set are discontinuous. For such situations neighboring ghost cells will have diverging paths along the tangent to the gradient of the level-set and thus refer to points on the zero level-set that are unrelated in position and state. Such situations are fundamental to the impact of two material regions in a vacuum when described by a single levelest. Before contact no mechanical information must be transmitted between regions separated by even a single cell. To properly handle such situations the domain is subdivided accordingly. Treatment of ghost cell and material regions is done separately. For each subdivided material region fluxes at the fluid-vacuum contact are determined by approximation of the solution to a Riemann problem in terms of the surface normal. Interior fluid midpoint point fluxes are determined by padding the region on either side with the solution to the Riemann problem and then performing a local Lax-Fredrichs splitting of fluxes,

$$f^{\pm} = \frac{1}{2}\big(f(q(x)) \pm |\lambda_{max}| q(x)\big), \tag{5.24}$$

in conjunction with fifth-order WENO to reconstruction. Ghost cells are subdivided into regions defined by the sign of the level-set gradient along the direction. Again for the ghost cells nearest to the contact flux reconstruction is determined by Riemann problem. The ghost cell regions are truncated to only include points within three cells of a material point. Figure 5.7 depicts the presently used subdivision for a situation in which a material region has a hole in it. Reconstruction of fluxes in the horizontal direction for the cells highlighted in red requires six subdivisions. It is important to note that each region may contain an overlap in the midpoints utilized for flux reconstruction. A single flux associated with a given midpoint is not possible and the scheme is not conservative.

5.2.2 Adaptive mesh refinement

As a simple extension to an adaptive mesh refinement capable solver each mesh patch is treated in the same manner. In taking this approach potential complications can occur when small voids or thin ligaments on a fine mesh are prolonged onto a coarse mesh. It is particularly problematic near thin ligaments where ghost cells would be identified but tracing along the tangent to the signed distance function would not result in actually reaching a free surface for use in a Riemann solver. To avoid such complications ghost cells that are within the appropriate limited band but do not result in a proper interpolation are flagged to be ignored.

Proper mesh refinement criteria for a level-set should include a curvature-based detection. Presently, a much simpler technique is utilized by flagging about changes in sign of the level-set ϕ. Additionally, density and velocity tolerance flagging criteria are applied. Vacuum cells are more or less inactive cells, except those nearest to free surfaces. It is therefore possible to use a very coarse base mesh with a large factor of refinement to the next mesh. For instance, for the axisymmetric simulation of a sphere-plate impact problem (see Figure 5.8) one level of refinement is used with a base mesh of 64x64 and refinement factor of 16x resulting in an equivalent mesh of 1024x1024 points.

5.3 Test problems

5.3.1 One-dimensional aluminum impact problem

To first explore the ghost fluid method outlined in previous sections for impact-driven flows in one dimension a unigrid code was developed in MATLAB. As a simple test an impact problem is utilized which demonstrates the capability of the method to handle single-cell voids in one dimension. Signed distance function reinitialization is performed directly rather than by partial differential equation solution. Additionally, a simple cell erosion approach to handling spallation is implemented in this one-dimensional code. When tension above some modeled value is achieved at a corresponding point that point is replaced by a vacuum. A grid scale violation of conservation occurs from the erosion

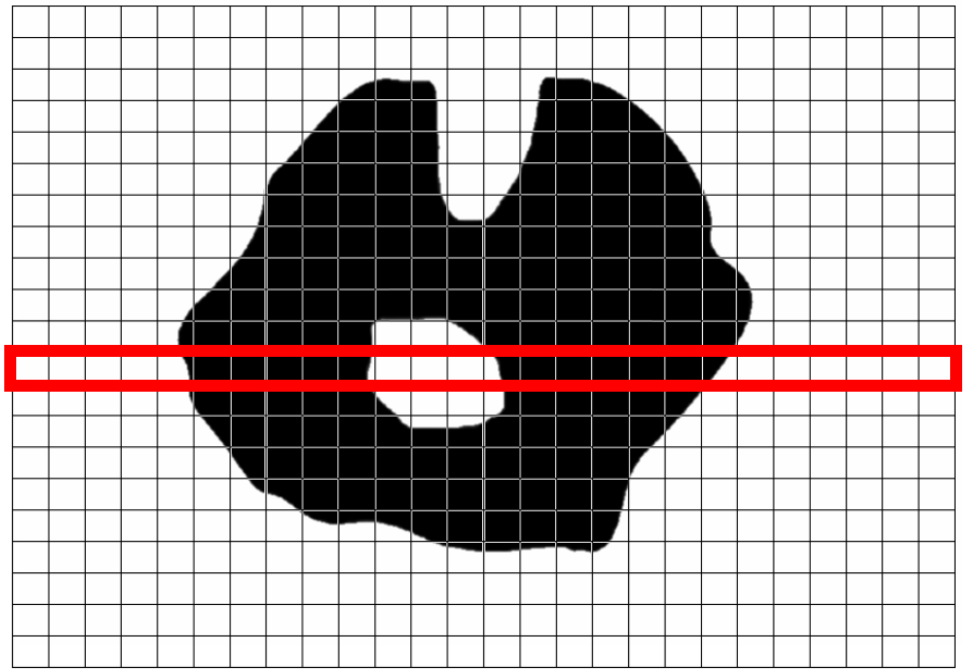

(a)

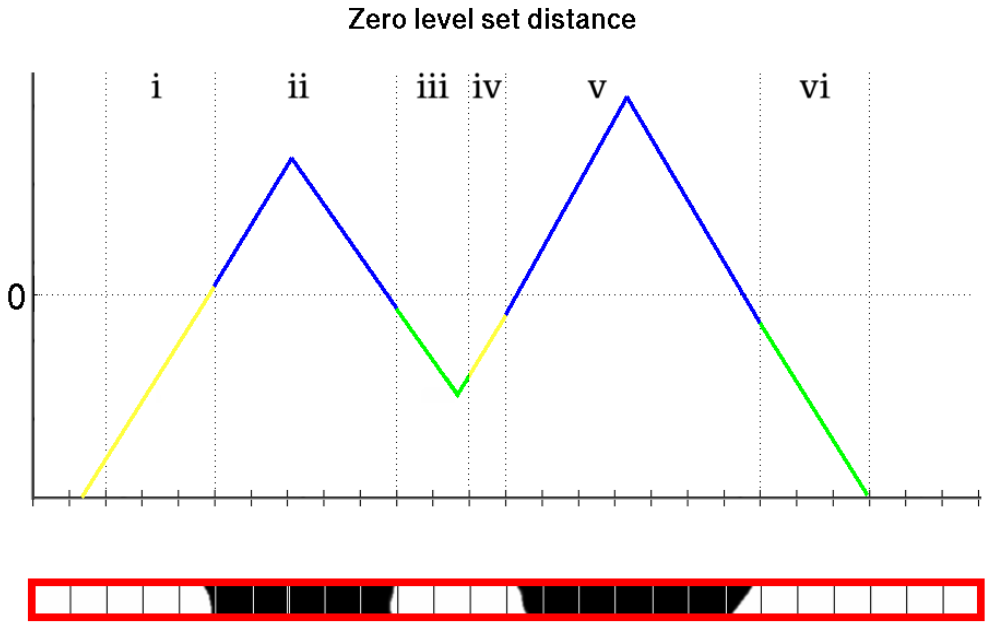

(b)

Figure 5.7: Schematic of the coordinate-wise decomposition of the domain for midpoint flux reconstruction based on the distance function. Regions *i*, *iii*, *iv*, and *vi* are ghost cells separated based on the gradient of the signed distance function. Regions *ii* and *v* are physical material regions. At each of the boundaries of the regions a Riemann problem for the surface normal direction is used to approximate the flux and pad the regions. For all other midpoints a fifth-order flux-splitting WENO reconstruction of the flux is utilized.

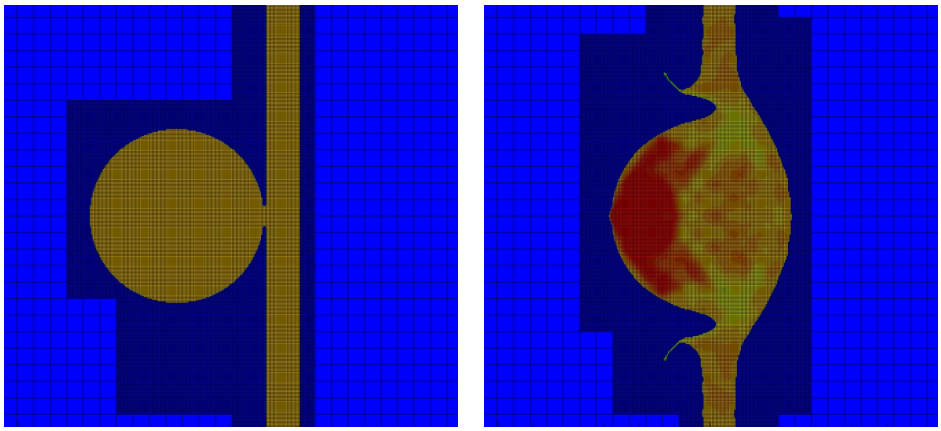

(a) (b)

Figure 5.8: Adaptive mesh refinement for ghost fluid method axisymmetric simulation of a sphere-plate impact. One level of refinement is utilized to solve the problem. The base mesh is very coarse at only 64x64 while the fine mesh is 16x refinement of the base.

and the approach is not a practical solution to modeling spallation in many situations, particularly those in more complex multidimensional problems.

The initial conditions for the impact problem are plotted in Figure 5.9. Two aluminum slabs of finite length 0.07 m, modeled by Mie-Grüneisen equation of state, initially are separated on either sides of the origin by $0.02m$. The slabs travel in opposite directions at a speed of 400 m/s until they meet at the origin and are welded into one by impact. The domain is discretized by 200 uniform points and adaptive time stepping is utilized to maintain a CFL of 0.75 throughout the simulation. Upon impact two shock waves travel in opposite directions away from the impact, shown in Figure 5.10. The shock waves travel until reaching the ends of the slab and generate a reflected expansion waves traveling towards the origin (see Figure 5.11). Upon reaching the origin a large amount of tension is created which splits the single slab of aluminum back into two. Figure 5.12 shows the resulting split slab with a shockwave closely followed by an expansion wave as a result of the split. The collision is effectively inelastic with the resulting velocity profiles in the individual slabs slightly less in magnitude on average than the initial 400 m/s.

5.3.2 Three-dimensional axisymmetric rod impact problem

As a second test problem, analogous to the first impact problem studied in one dimension, next simulated is the three-dimensional axisymmetric impact of two aluminum rods. Signed distance function reinitialization is performed by partial differential equation solution and no simple cell erosion approach to handling spallation is implemented. The two rods are initially in contact traveling at 500 m/s in opposite directions. The two rods have length 0.04 m and radius of 0.01 m. A base mesh of 64x128 points with 3 levels of 2x refinement was used to simulate the impact with adaptively

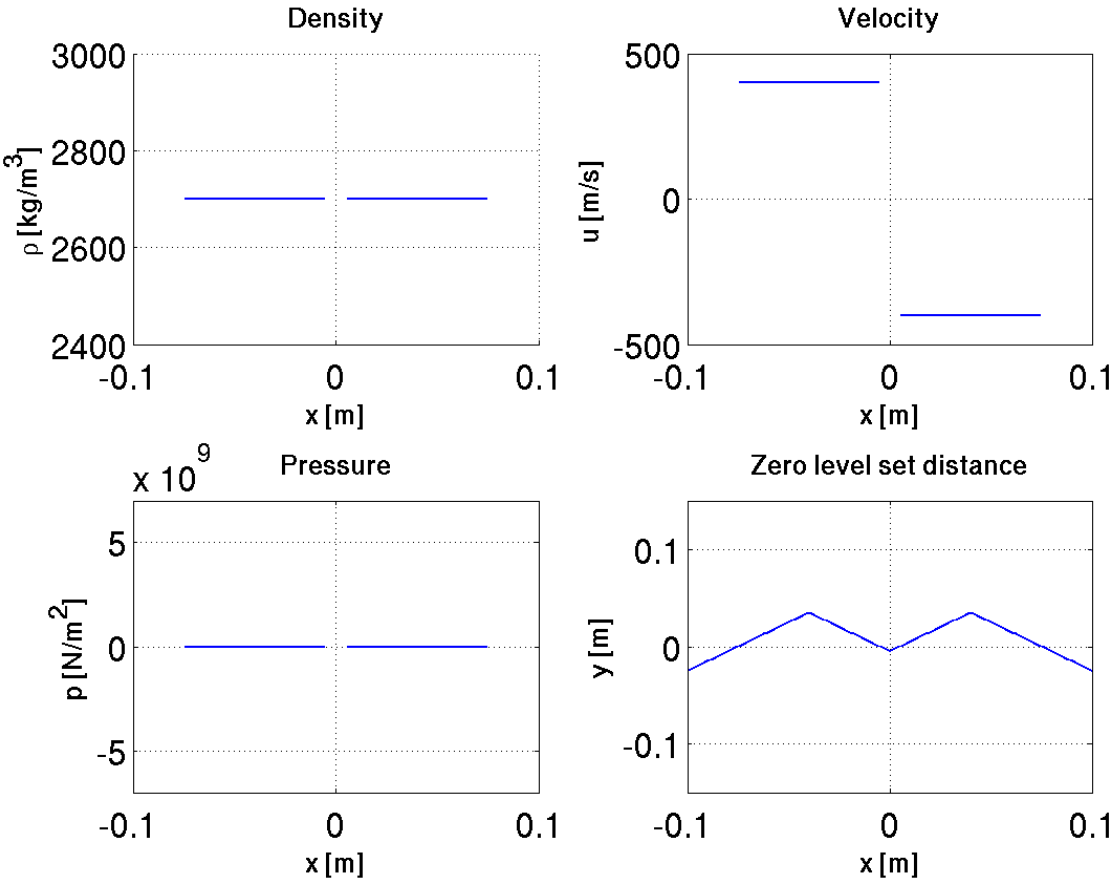

Figure 5.9: Plot of the initial conditions for a one-dimensional simulated impact of two finite aluminum pieces modeled by Mie-Grüneisen equation of state traveling in opposite directions at 400 m/s. The domain is decomposed in to 200 points including the void regions.

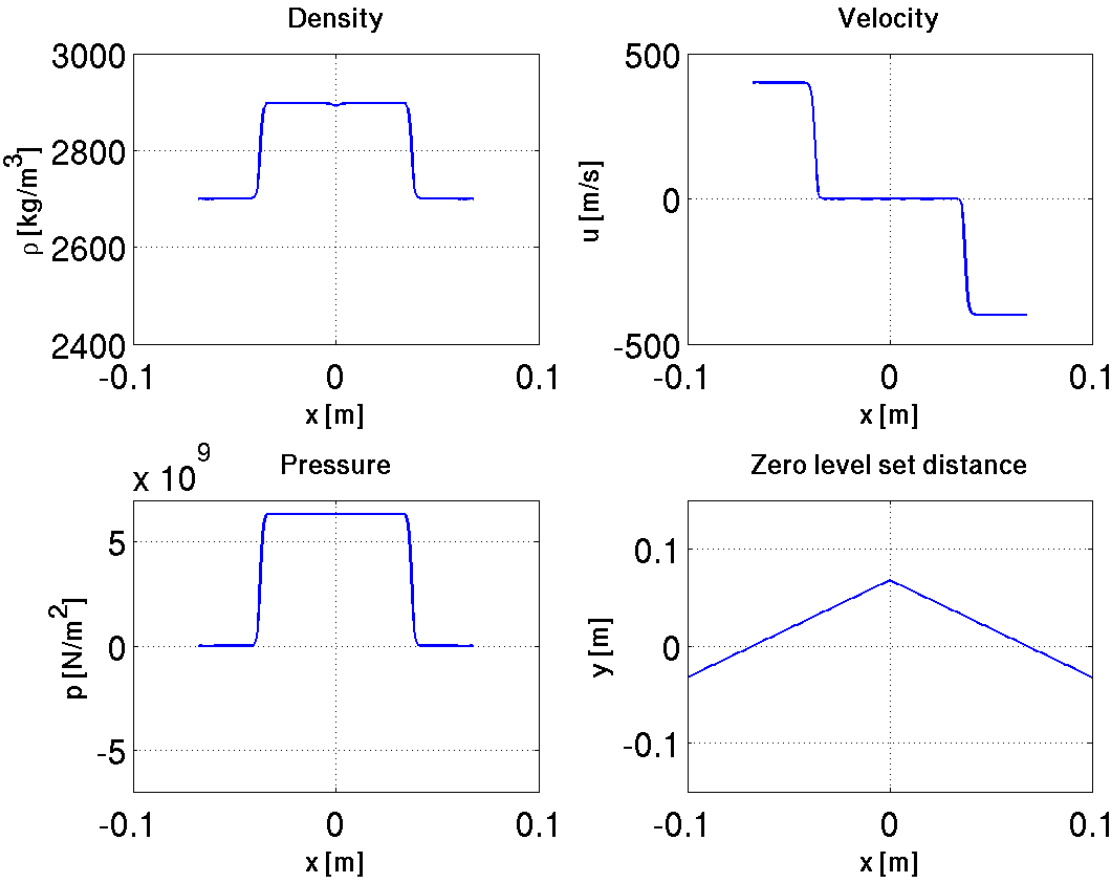

Figure 5.10: One-dimensional finite length 400 m/s Mie-Grüneisen aluminum impact problem solution at $t = 18.0$ μs. Shock waves are seen to propagate away from the impact on either side.

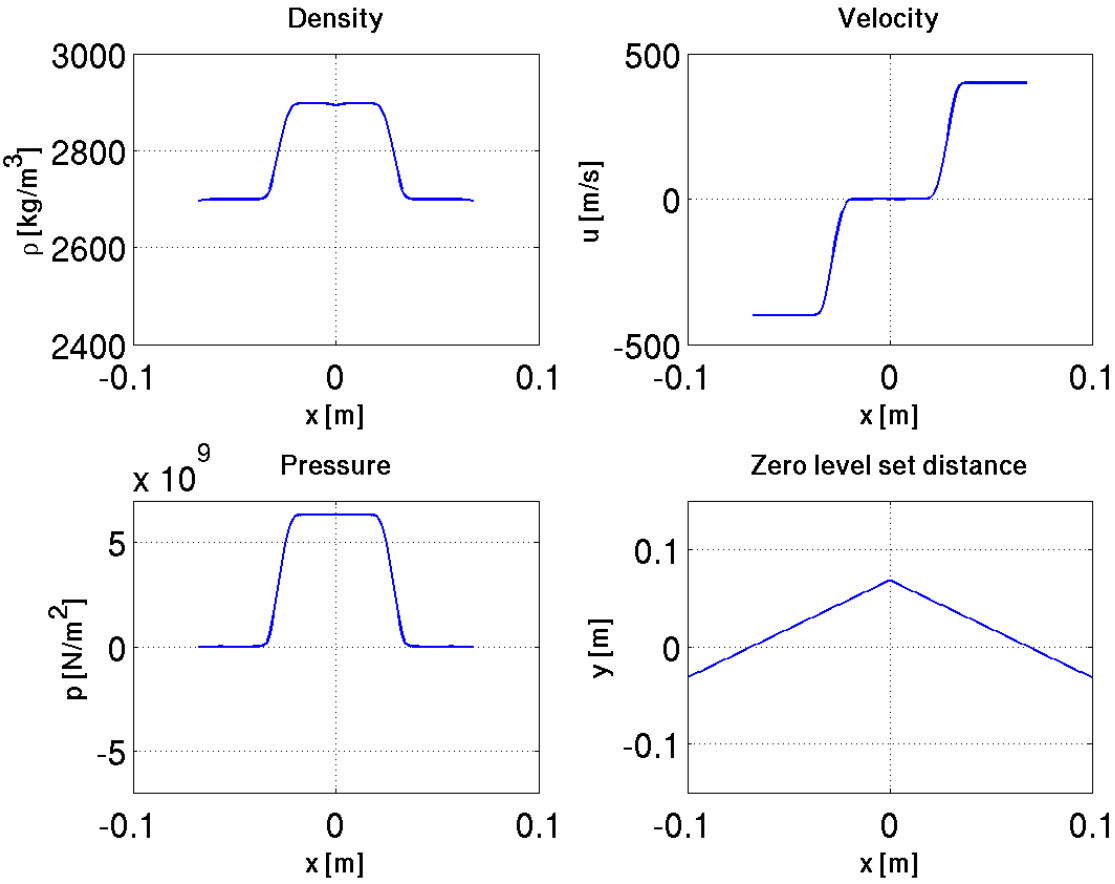

Figure 5.11: One-dimensional finite length 400 m/s Mie-Grüneisen aluminum impact problem solution at $t = 30.0$ μs. Once the shock waves reach the end of the finite length material a reflected expansion wave is generated as is presently shown.

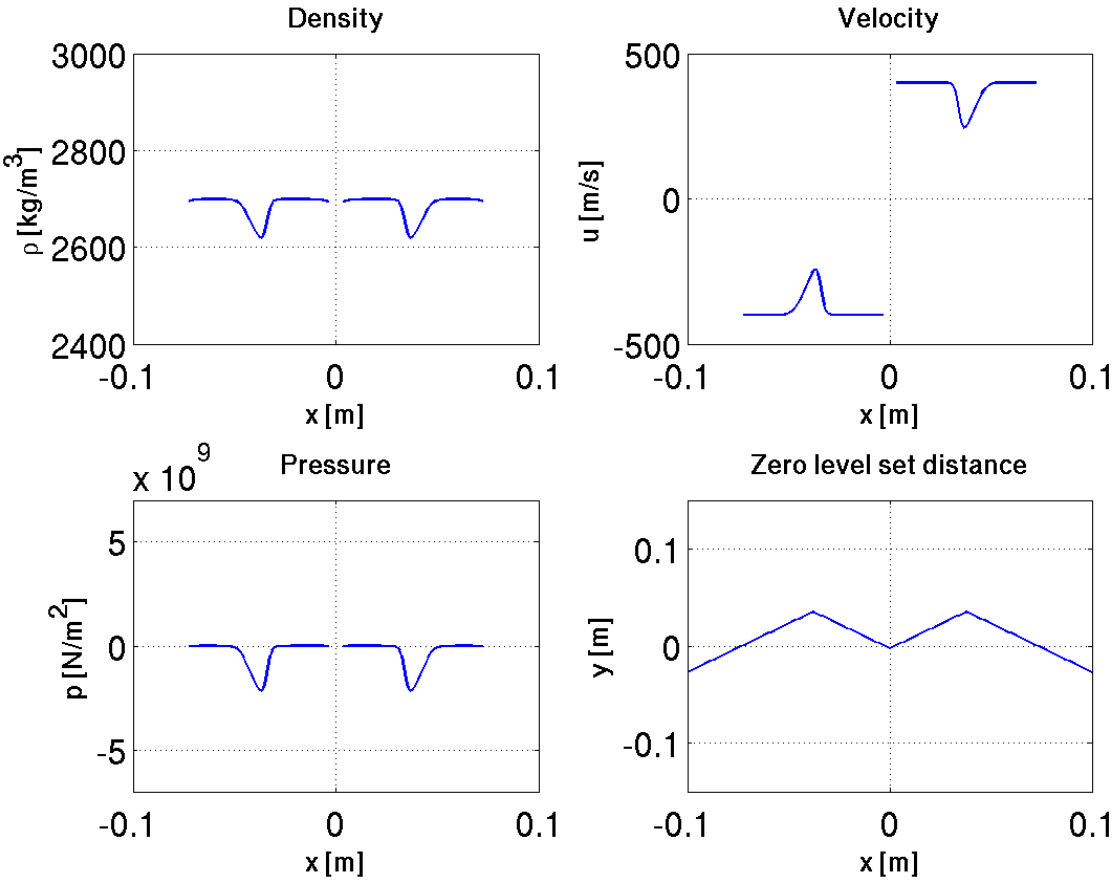

Figure 5.12: One-dimensional finite length 400 m/s Mie-Grüneisen aluminum impact problem solution at $t = 42.0$ μs. Once the expansion waves meet at the middle of the material a large amount of tension occurs splitting the material in two again. Each piece propagates away at an average speed slightly less in magnitude than the original impact speed.

maintained CFL of 0.75. Figure 5.13(a) shows density contours shortly after impact at time 1.25 micro seconds. Two planar shocks are immediately created as in the one-dimensional problem, but due to the free surface of the cylinder the initial compressive stress of the impact cannot be supported and the rod begins to expand in the radial direction behind the shock front. The expanding material creates tension behind the increasingly weak shockwave. The expansion waves generated in the radial direction eventually meet and generate compression, seen at time 6.25 in Figure 5.13(b). The now weak shock reflects off the end of the rods. A series of complex wave patterns develops due to radial and horizontal waves bouncing between free surfaces.

5.3.2.1 Three-dimensional axisymmetric sphere-plate impact problem

To further examine the ghost fluid method for free surface impact problems a three-dimensional axisymmetric aluminum sphere-plate impact problem is simulated. The sphere has a radius 0.025 m and travels toward the plate at 500 m/s. The plate has a thickness of 0.01 m. A base mesh of 64x64 points is utilized with 1 level of 16x refinement for an equivalent of 128 points across the diameter of the sphere. A CFL of 0.75 was adaptively maintained throughout the simulation.

Density and x-velocity component contours are given in Figure 5.14 for initial conditions and two successive times. The sphere generates a continuous series of impacts as more and more of it welds to the plate. These impacts set up a curved shock which reflects off the back end of the plate and generates tension. Failure to support the compression of the impact at the free surface of the plate forces expansion. The expansion sets up something analogous to a "splash" as the material tries to move aside and is forced in the direction of least resistance. By 3.0 micro seconds a very complex and seemingly chaotic set of waves reflecting through the medium are observed. Further away from the impact site the x-velocity component remains close to the initial 500 m/s in magnitude. The feature analogous to a "splash" continues to grow, perhaps unrealistically due to poor numerical treatment at regions of high curvature in the free surface.

One quantity of physical interest for such impact problems is the hole size generated. The ability to accurately capture the impact hole diameter is essential for any simulation to be a practical tool for prediction. Hole radius results for the present ghost fluid method and material model are presented in Figure 5.16. The growth rate of the impact hole is observed to only gradually decrease with time, perhaps never to reach a constant value. The simulation therefore does not provide a realistic prediction, as should be expected without shear strength.

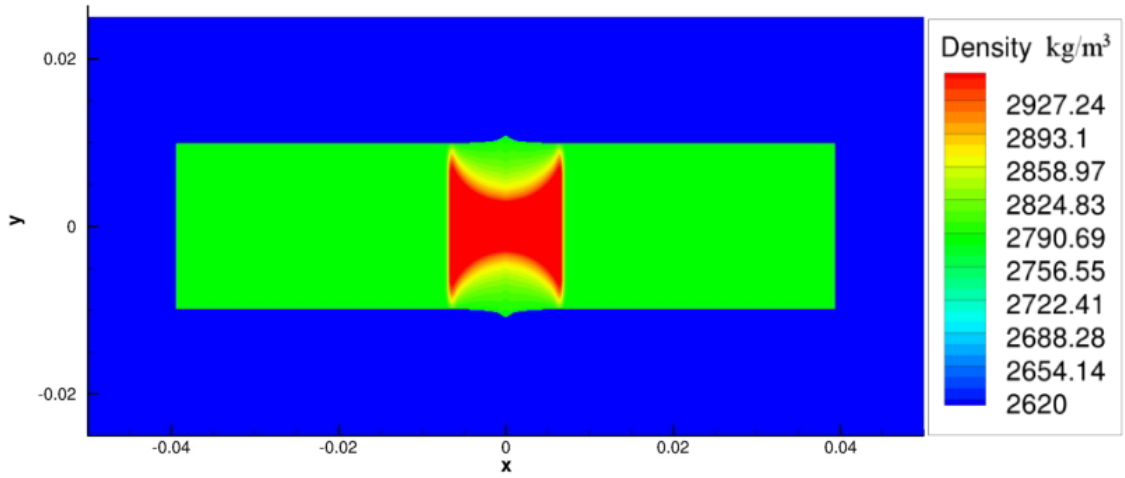

(a)

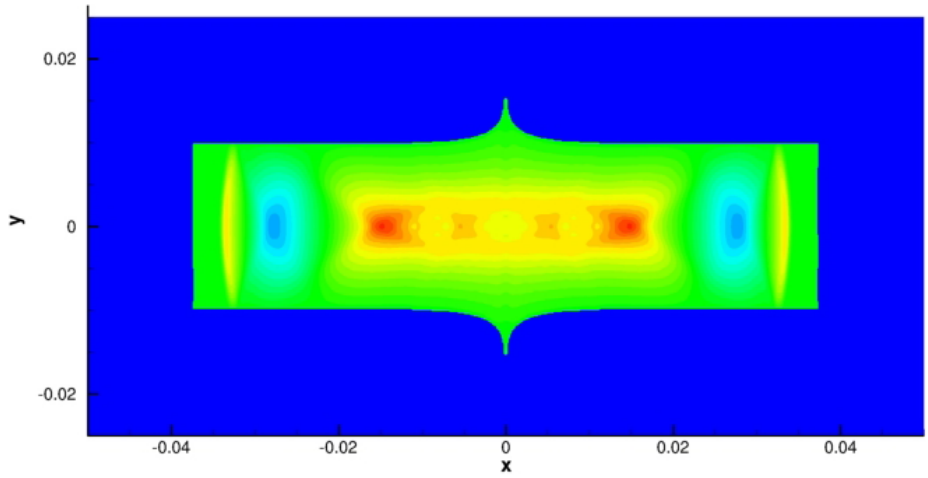

(b)

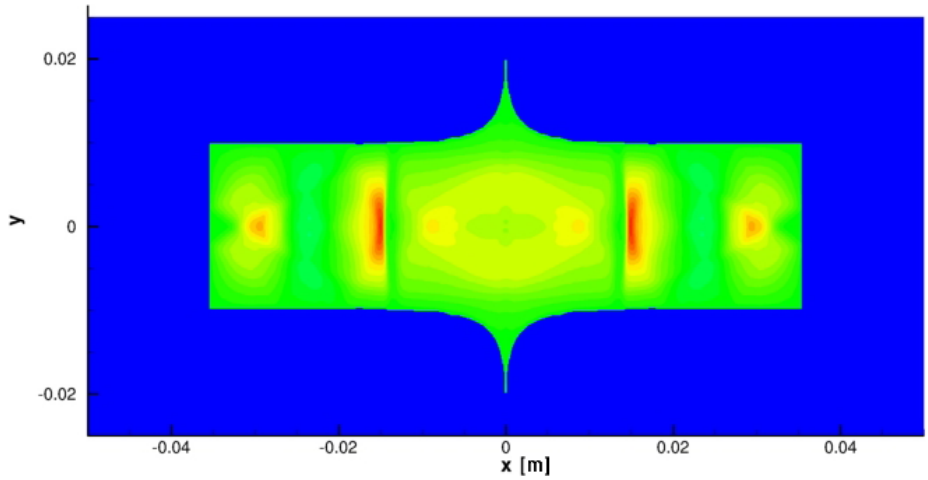

(c)

Figure 5.13: Axisymmetric simulation of the collision of two aluminum rods initially traveling 500 m/s in opposite directions in a vacuum. Density contours shown at times 1.25, 6.25, and 11.25 micro seconds.

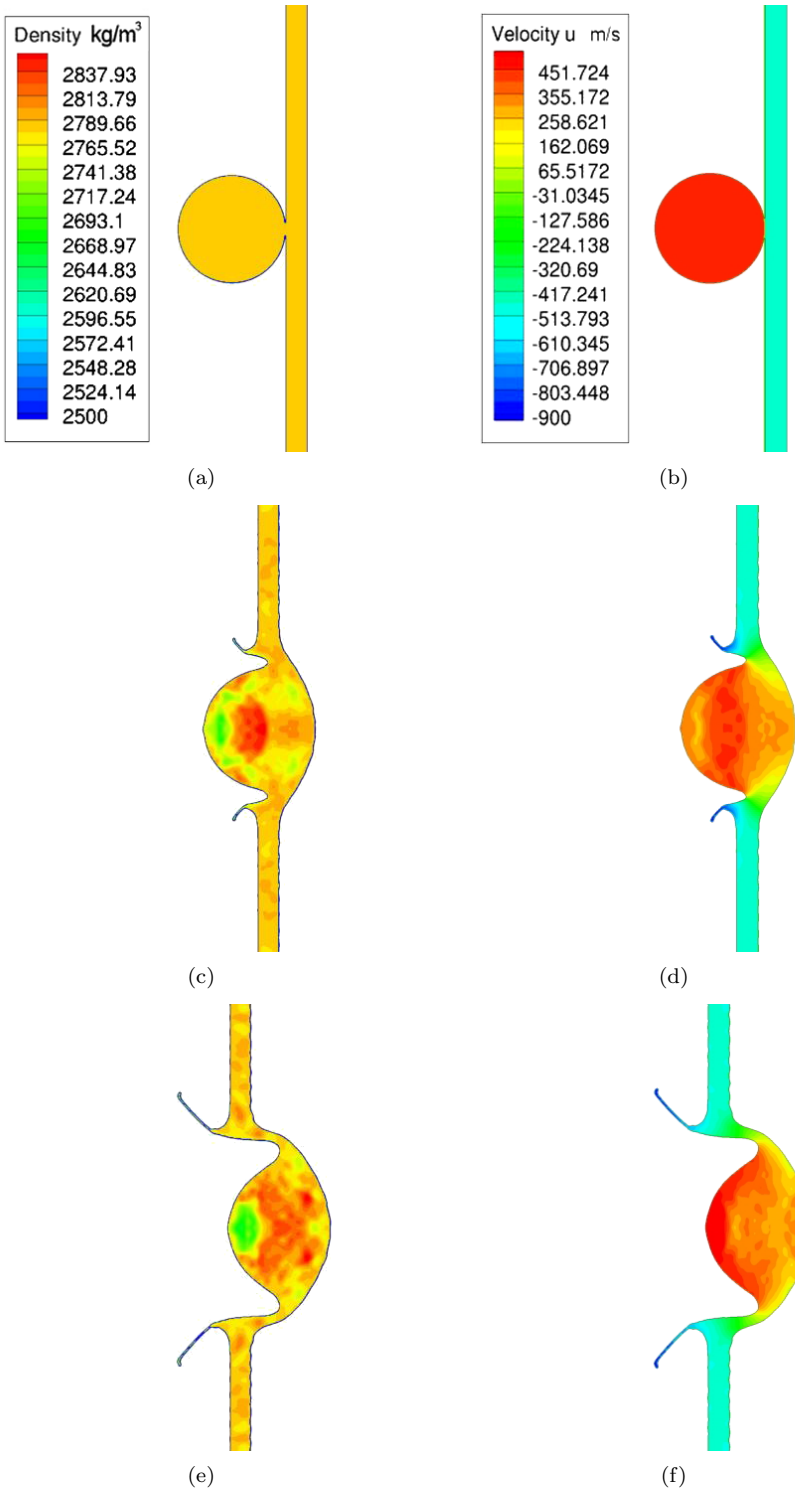

Figure 5.14: Axisymmetric simulation of a sphere impacting a plate at 1.0 km/s. Density and x-velocity component contours shown at time 0.0, 3.0, and 6.0 μs.

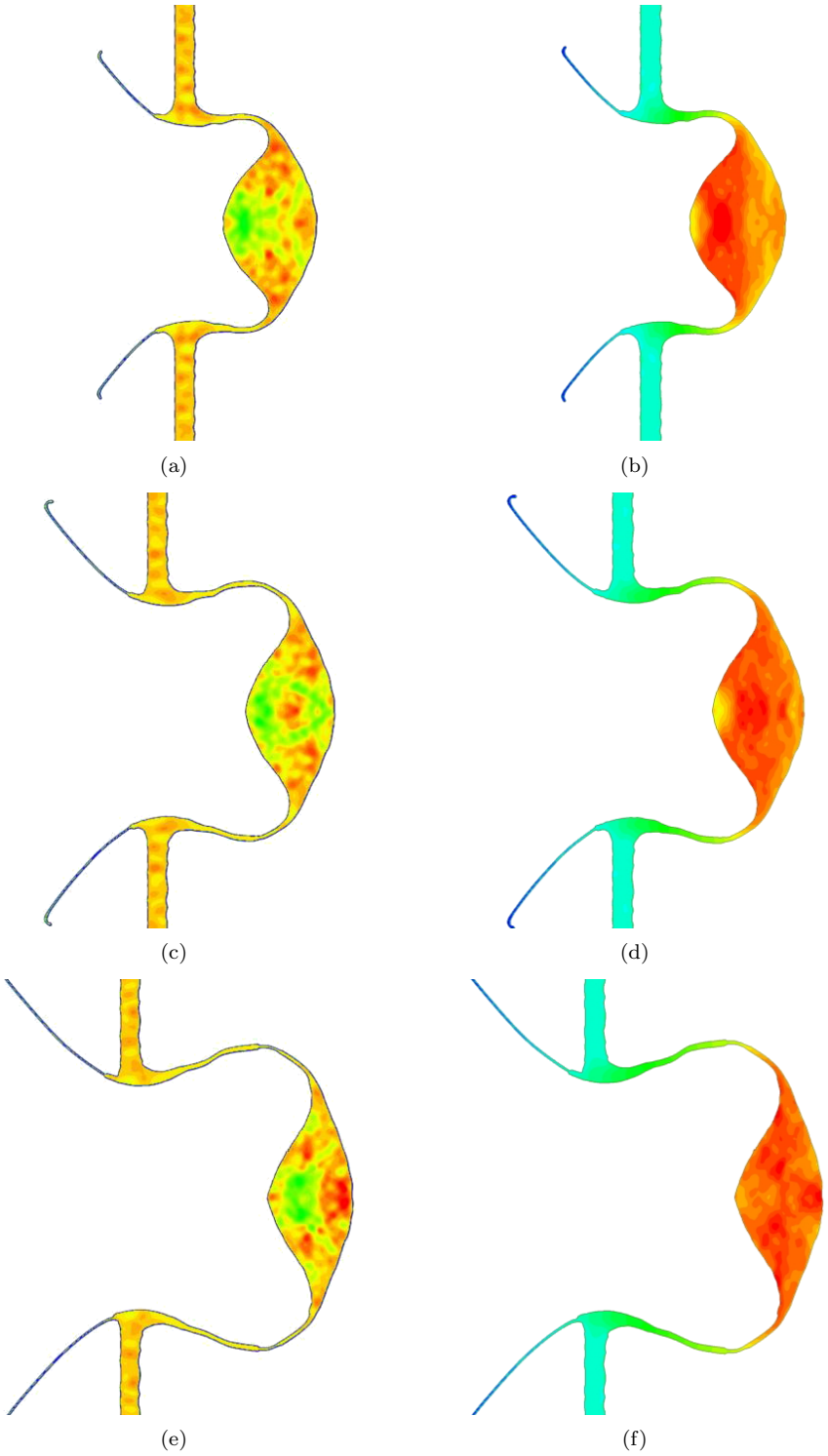

(a) (b) (c) (d) (e) (f)

Figure 5.15: Further results for axisymmetric simulation of a sphere impacting a plate at 1.0 km/s. Density and x-velocity component contours shown at time 9.0, 11.0, and 13.0 μs.

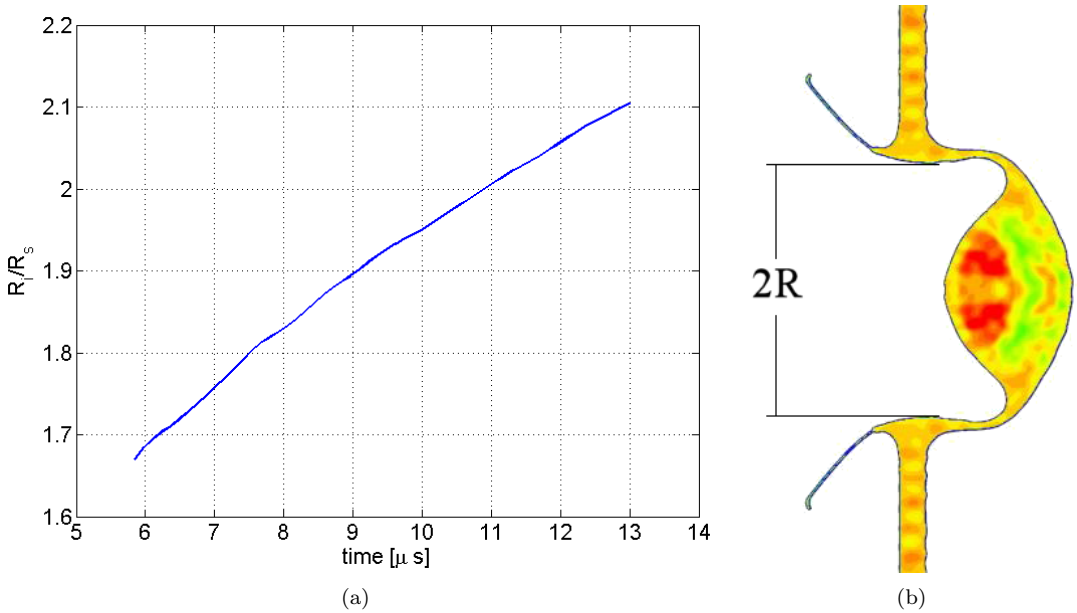

(a) (b)

Figure 5.16: Aluminum 1.0 km/s sphere-plate impact hole radius as a function of time. The hole radius is seen to increase as a function of time, only slowing gradually.

Chapter 6

Nonlinear elastic-plastic solids

In the following Chapter a brief investigation of the assumptions made in using an isotropic stress model for solids is undertaken. Solids are distinguishable from fluids in that they resist continuous deformation under shear stresses. It is therefore reasonable to expect that isotropic models will not give realistic results when shear is important. Furthermore, most solids can support anisotropic states of stress in a limited capacity. For many ductile solids under high compressive stress plastic yielding occurs limiting the amount of shear stress and thus anisotropy in the stress state [31, 96]. Under such conditions at least some similarity in flow structure should be expected between purely fluid and solid material models. In the following sections these issues are explored using comparisons between materials with Mie-Grüneisen equation of state and hyper-elastic solid models.

6.1 Nonlinear hyper-elastic solids

At a minimum, to simulate the response of a material to internal and external forces by continuum, a model that relates relative displacement of points to internal stresses must be made. The displacement of points can be described as a function of the initial position X and the present time t, $\mathbf{x} = \mathbf{x}(\mathbf{X}, \mathbf{t})$. The relative displacement of two infinitesimally close points is then described by the deformation gradient tensor [5, 78],

$$F_{ij} = \frac{\partial x_i}{\partial X_j}. \tag{6.1}$$

For isotropic inviscid fluids only volumetric changes are of interest in relation to density changes, related to the deformation gradient tensor by

$$\rho_0/\rho = det(\mathbf{F}). \tag{6.2}$$

Alternatively, for a solid the stress state may be anisotropic and depend on the full nature of the deformation. Material models which relate stress strictly to the deformation gradient tensor and some other thermodynamic quantity are known as hyper-elastic solid models [28, 55, 56]. For

consistency it is convenient to formulate the hyper-elastic solid model directly in terms of internal energy

$$e = e(\mathbf{X}, \mathbf{F}, \mathbf{s}), \tag{6.3}$$

where s is the entropy. The definition of the stress tensor follows directly from required consistency in conservation of energy [78],

$$\sigma_{ij} = -\rho \frac{\partial e}{\partial F_{ik}} F_{jk}. \tag{6.4}$$

An alternative equivalent formulation of a hyper-elastic solid is in terms of the inverse deformation gradient tensor defined by $\mathbf{f} = \mathbf{F^{-1}}$. In terms of the inverse deformation gradient tensor the stress tensor becomes

$$\sigma_{ij} = -\rho \frac{\partial e}{\partial f_{kj}} f_{ki}. \tag{6.5}$$

Further consideration of frame indifference arguments demonstrate that internal energy must only be a function of $\mathbf{C} = \mathbf{F}^{\mathbf{T}}\mathbf{F}$, the right Cauchy-Green tensor [78].

$$e = e(\mathbf{X}, \mathbf{C}, \mathbf{s}) \tag{6.6}$$

Additionally, only isotropic materials are considered. For isotropic solids the internal energy must depend on the right Cauchy-Green tensor only through its invariants [78],

$$\begin{aligned} I_1 &= tr(\mathbf{C}), \\ I_2 &= det(\mathbf{C}) tr(\mathbf{C^{-1}}) = \tfrac{\mathbf{1}}{\mathbf{2}} \Big[tr(\mathbf{C^2}) - tr(\mathbf{C})^{\mathbf{2}} \Big], \\ I_3 &= det(\mathbf{C}). \end{aligned} \tag{6.7}$$

6.1.0.2 A simple hyper-elastic aluminum model

A large variety of models for equations of state for various materials can be found in literature [28, 55, 56]. Presently, a simple hyper-elastic model is used that was proposed by Miller and Colella [55] that is a variant of the Blatz and Ko model,

$$e = \frac{\mu_0}{2\rho_0} \Big(I_1 - 3 I_3^{1/3} \Big) + \int_{\rho}^{\rho_0} \frac{p(\rho', s)}{{\rho'}^2} d\rho'. \tag{6.8}$$

Here $p(\rho, s)$ could come from a variety of models for the bulk response including Hugoniots. Currently, the third-order polynomial

$$p(\rho) = w_1(\rho/\rho_0 - 1) + w_2(\rho/\rho_0 - 1)^2 + w_3(\rho/\rho_0 - 1)^3 \tag{6.9}$$

proposed in [55] is used. For aluminum the coefficients to this polynomial are taken as $w_1 = 72.0$ GPa, $w_2 = 172.0$ GPa, and $w_3 = 40.0$ GPa. Additionally, the shear modulus for aluminum is taken

to be $\mu_0 = 24.8\ GPa$ and $\rho_0 = 2785.0\ kg/m^3$. The model is strictly dependent on the deformation of the material as no thermodynamic quantities other than density are utilized. The stress tensor associated with this equation of state is then [28]

$$\sigma = \mu_{\mathbf{o}} \frac{\rho}{\rho_{\mathbf{o}}} \Big(\mathbf{F}\mathbf{F}^{\mathbf{T}} - \Big(\frac{\rho}{\rho_{\mathbf{o}}} \Big)^{\mathbf{-2/3}} \mathbf{I} \Big) + \mathbf{p}(\rho, \mathbf{s})\mathbf{I}. \tag{6.10}$$

Furthermore, for flux-splitting and CFL calculations it is useful to have acoustic propagator tensor. For direction n the acoustic propagator tensor is given by

$$\mathbf{A}^{\mathbf{n}}_{\mathbf{ij}} = -\frac{\mathbf{1}}{\rho} \frac{\partial \sigma_{\mathbf{in}}}{\partial \mathbf{f}_{\mathbf{kn}}} \mathbf{f}_{\mathbf{kj}} \tag{6.11}$$

with no sum on n [28]. For the modified Blatz and Ko model the acoustic propagator tensor in analytic form is therefore

$$\mathbf{A}^{\mathbf{n}}_{\mathbf{ij}} = \frac{\mu_{\mathbf{o}}}{\rho_{\mathbf{o}}} \mathbf{F}_{\mathbf{nk}} \mathbf{F}_{\mathbf{nk}} \delta_{\mathbf{ij}} + \Big(\frac{\partial \mathbf{p}(\rho)}{\partial \rho} + \frac{\mathbf{1}}{\mathbf{3}} \frac{\mu_{\mathbf{o}}}{\rho_{\mathbf{o}}} \Big(\frac{\rho}{\rho_{\mathbf{o}}} \Big)^{\mathbf{-2/3}} \Big) \delta_{\mathbf{in}} \delta_{\mathbf{jn}} \tag{6.12}$$

6.1.1 Plasticity

Most ductile metals can only support a limited amount of anisotropic stress before yielding occurs. Upon yielding an irreversible change in the material occurs resulting in what is observed as plastic deformation. For ductile metals the process of yielding is caused by dislocation motion in the atomic crystal structure [31]. For metals where the crystal grains are randomly oriented and grain sizes are much smaller than gradients of interest it is reasonable to model plastic behavior with a continuum model [66, 67, 91]. Presently, the method developed by Miller and Colella [55] for tracking plastic deformation is utilized. In their approach the deformation gradient is modeled by matrix multiplication of two tensors, one an elastic deformation gradient tensor and the other a tensor associated with plastic deformation,

$$\mathbf{F} = \mathbf{F}^{\mathbf{e}} \mathbf{F}^{\mathbf{p}}. \tag{6.13}$$

6.1.1.1 Visco-plastic modeling

To describe a material completely a model of how the plastic deformation tensor $\mathbf{F}^{\mathbf{p}}$ evolves must be formed. Evolution of the form

$$\frac{D\mathbf{F}^{\mathbf{p}}}{Dt} = \mathbf{L}^{\mathbf{p}} \mathbf{F}^{\mathbf{p}} \tag{6.14}$$

is assumed [55]. Where $\mathbf{L}^{\mathbf{p}}$ is a tensor utilized to control the rate of plastic deformation. This evolution equation is essentially that of advection with a rate correction source term. For further details on various forms of the tensor $\mathbf{L}^{\mathbf{p}}$ see [28, 55]. Presently, a von Mises yield surface is utilized

with an ideal power law rate based model for $\mathbf{L^P}$ in order to keep the stress on the yield surface through source term correction to the evolution of the plastic deformation gradient tensor.

6.2 Equations of motion

The equations of motion for hyper-elastic solids in an Eulerian setting form a conservative hyperbolic set of equations. Reynold's transport theorem remains true with only slight variation, due to a full stress tensor, in the conservation of mass, momentum, and energy equation,

$$\frac{\partial \rho}{\partial t} + \frac{\partial(\rho u_j)}{\partial x_j} = 0, \tag{6.15}$$

$$\frac{\partial(\rho u_i)}{\partial t} + \frac{\partial(u_j \rho u_i)}{\partial x_j} - \frac{\partial \sigma_{ij}}{\partial x_j} = 0, \tag{6.16}$$

$$\frac{\partial(\rho E)}{\partial t} + \frac{\partial(u_j \rho E + u_i \sigma_{ij})}{\partial x_j} = 0, \tag{6.17}$$

$$\tag{6.18}$$

where $E = e + \frac{1}{2} u_i u_i$ [55]. In addition to these familiar equations, a set of evolution equations for the inverse deformation gradient tensor must be formed. These conservative evolution equations for the inverse deformation tensor follow directly from its Definition 6.1,

$$\frac{\partial f_{kj}}{\partial t} + \frac{\partial(f_{ki} u_i)}{\partial x_j} = 0. \tag{6.19}$$

$$\tag{6.20}$$

For use of the plasticity model of Miller and Colella [55] an additional plastic tensor must be advected along with the flow and corrected by a rate source term,

$$\frac{\partial(\rho F^p_{ij})}{\partial t} + \frac{\partial(\rho u_k F^p_{ij})}{\partial x_k} = \rho L^p_{ik} F^p_{kj}. \tag{6.21}$$

As discussed, the source term here acts to bring the stress state back on to the yield surface [55]. The rate at which the deformation is corrected by this source term would typically require a much smaller time step for numerical stability than the standard wave speed based CFL condition of the rest of the hyperbolic system. The system is therefore "stiff" in nature and requires special treatment to solve efficiently.

6.3 Numerical method

Without the plastic rate source term the governing equations of motion are a system of hyperbolic partial differential equations. Thus, for single-phase strictly elastic problems a fifth-order WENO

reconstruction of Lax-Fredrichs split fluxes is utilized in conjunction with third-order Runge-Kutta temporal discretization to advance the solution in time [30]. For two-phase elastic problems an ad hoc mixing approach analogous to that used previously for the Mie-Grüneisen equation of state. As discussed in previous sections, for Mie-Grüneisen fluids phase errors can result in serious additional complications. Although not as serious as the catastrophic oscillations observed for many Mie-Grüneisen fluids, minor phase error oscillations can occur for the presently used variant of the Blatz and Ko model. To mitigate these problems the conserved quantity ρ/ρ_0 is tracked,

$$\frac{\partial(\rho/\rho_0)}{\partial t} + \frac{\partial(u_k\rho/\rho_0)}{\partial x_k} = 0, \tag{6.22}$$

which is a fundamental ratio in the polynomial model for the bulk material response and thus eliminates associated phase errors. The ad hoc mixture fraction is then simply

$$y(\mathbf{x},\mathbf{t}) = \frac{\rho_{\mathbf{0}}(\mathbf{x},\mathbf{t}) - \rho_{\mathbf{0}}^{\mathbf{1}}}{\rho_{\mathbf{0}}^{\mathbf{2}} - \rho_{\mathbf{0}}^{\mathbf{1}}}. \tag{6.23}$$

The use of such mixture models enforces a no-slip condition at the contact between materials. The deformation across the ad hoc mixture zone is continuous.

6.3.1 Plastic source term

The visco-plastic model utilized in keeping the stress state on the yield surface results in an additional complication in that it requires severe limitations on time stepping for stability in comparison to the rest of the system. To treat this term properly while maintaining the standard approach to solving the rest of the system of partial differential equations a first-order operator splitting approach is taken [30, 55]. In the present approach the solution is first advanced in time without the source term by third-order TVD Runge-Kutta. Following this update a second update is performed strictly on the plastic deformation gradient tensor due to the source term. Since the source term is only dependent on the local state the solution update can be performed as though each point were governed by a system of ordinary differential equation. To solve the ordinary differential equation numerically to the desired precision ODEPACK developed at Lawrence Livermore National Laboratory (LLNL) is utilized [32]. The stiff solver subroutine LSODE [70] which uses Adam's method for non-stiff problems and Gear implicit methods for stiff problems is applied.

6.3.2 Gauge constraint

Since the components of the deformation gradient tensor and its inverse are derived from the gradient of a scalar field the gauge constraint

$$\vec{G}_i = \vec{\nabla} \times f \cdot \vec{e}_i = \vec{\nabla} \times (\vec{\nabla} X_i) = 0, \tag{6.24}$$

if initially satisfied, should be satisfied for all time [55]. Additionally, the determinant of the inverse deformation gradient tensor should be related to the density by

$$\rho_0/\rho = \frac{1}{det(\mathbf{f})}. \tag{6.25}$$

Numerical errors introduce deviation from these constraints which lead to spurious waves. For this reason Miller and Colella [55] introduce a diffusion term in the evolution equations to force the inverse deformation gradient toward satisfying the gauge constraint. Furthermore, a relaxation correction is applied to force the determinant of the inverse deformation gradient to remain related to the density. The numerical evolution equation utilized in evolving the inverse deformation gradient tensor is given by

$$\frac{\partial(f \cdot \vec{e}_i)}{\partial t} + \vec{\nabla}\big(\vec{u} \cdot (f \cdot \vec{e}_i)\big) = \big(\vec{u} \times \vec{G}_i\big) - D\big(\vec{u} \times \vec{G}_i\big) + \eta\Big(\frac{\rho}{\rho_0 det(f)} - 1\Big) f \cdot \vec{e}_i. \tag{6.26}$$

In two dimensions the optimal diffusion dampening and relaxation are given by $D = \frac{\Delta x^2}{8\Delta t}$ and $\eta = \frac{1}{6\Delta t}$. The CFL for the system is

$$\frac{\Delta t(|u| + a)_{max}}{\Delta x} + \frac{4D\Delta t}{\Delta x^2}. \tag{6.27}$$

The optimal D coefficient therefore leads to a constrained time step half of the standard value by a CFL condition of one.

6.4 Equation of state comparison

In the following two sections an examination and comparison of the various equation of state models is undertaken. First, results for a simple one-dimensional impact problem are presented for fluid, elastic, and elastic-plastic models of aluminum. Secondly, an axisymmetric impact problem with multiple phases is examined for fluid and elastic-plastic models.

6.4.1 One-dimensional impact problem

To examine the effect of the isotropic stress tensor utilized in Mie-Grüneisen models for aluminum a one-dimensional impact problem is simulated using fluid, elastic, and elastic-plastic models. The initial conditions for the problem are given by two semi-infinite slabs of aluminum traveling in opposite directions at 400 m/s. The slabs are initially in contact at the origin resulting in an impact and symmetric compressive waves traveling away from the origin. The fluid solution is expected to be composed of two shocks traveling away from the impact.

Presented first are results for elastic and elastic-plastic models. All simulations were performed using a domain of $|x| < 0.1$ m discretized uniformly by 200 points. The CFL was maintained adaptively around 0.45 or less. Solution density and velocity profiles are seen in Figure 6.1 for a time of 10.0 micro seconds after impact. Differences in shock structure and speed are observable between elastic and elastic-plastic solutions. A single elastic shock propagates away from the impact, leading the elastic-plastic wave structure. Alternatively, the elastic-plastic wave structure is composed of two distinct shocks. The leading shockwave is considerably weaker and just slightly faster than the proceeding shock. The smaller shockwave is known as an elastic precursor. Under certain conditions elastic precursor shocks are known to occur [96] before transition to plastic flow. The stronger shock is plastic in nature. The density at the origin is considerably less for the elastic solution than for the elastic-plastic.

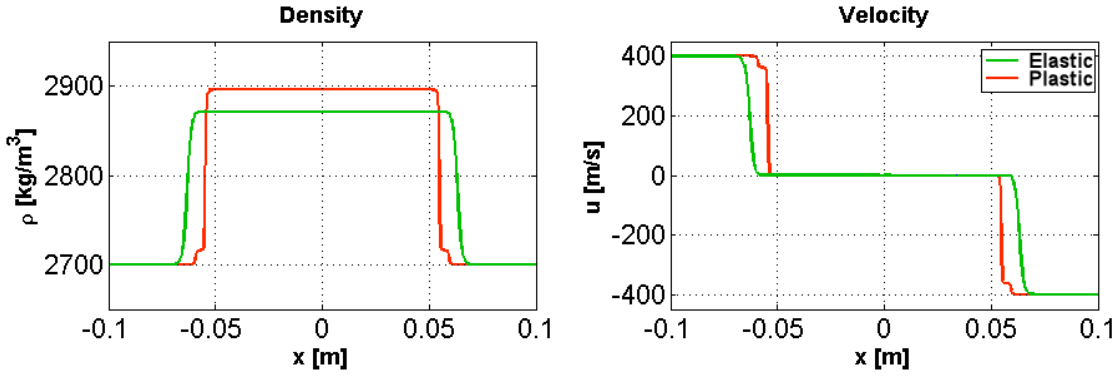

Figure 6.1: One-dimensional aluminum impact problem comparison. Two semi-infinite slabs of aluminum impact traveling in opposite directions at 400 m/s. Solution shown at 10.0 micro seconds for elastic and elastic-plastic models of aluminum.

In Figure 6.2, the Mie-Grüneisen equation of state solution for the problem is imposed on the elastic and elastic-plastic solutions. As is expected, the solution consists of two compressive shocks traveling in opposite directions away from the impact. The speed at which these shock waves travel is close to that of the plastic shock of the elastic-plastic solution. Additionally, the density jump across the shocks for the fluid and elastic-plastic models are in good agreement. The result is expected

since the elastic deformation is limited for the elastic-plastic model and therefore the bulk response should become the dominant factor.

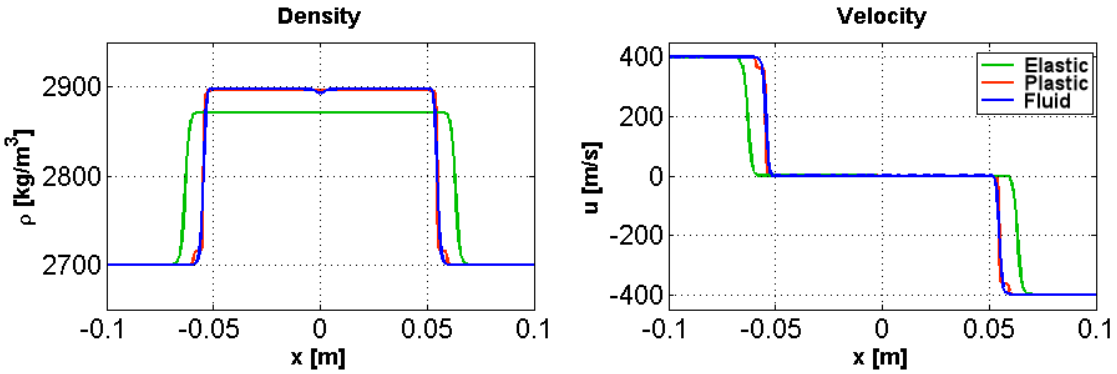

Figure 6.2: One-dimensional aluminum impact problem comparison. Two semi-infinite slabs of aluminum impact traveling in opposite directions at 400 m/s. Solution shown at 10.0 micro seconds for Mie-Grüneisen fluid, elastic, and elastic-plastic models of aluminum.

6.4.2 Three-dimensional axisymmetric impact problem

Next, the axisymmetric simulation of a problem with experimental application to measuring material Hugoniots is examined [11]. For details on the extension of the equations of motion for fluids and elastic-plastic solids to cylindrically axisymmetric problems see Appendix A. The problem involves a semi-infinite slab of aluminum striking a cylindrical copper core surrounded by aluminum at 1.0 km/s. The inner copper core has a radius of 2.38 mm. Figure 6.3 shows the initial conditions and configuration for a plane of symmetry.

Upon impact planar shock structures are initiated in the inner copper and outer aluminum. The shock waves in the outer aluminum travel faster than those in the copper. As a result, an oblique shockwave structure traveling at the same horizontal speed as the planar aluminum shock begins to form in the copper at the contact with aluminum. The oblique shock never reflects off the centerline of the copper cylinder, instead forming a Mach stem that travels along at the same speed as the outer aluminum planar shock (see Figure 6.4). The configuration allows for the creation of stronger shocks in the copper than would be achievable by a simple impact approach of the same momentum, which is useful for measuring Hugoniot properties [11].

Simulation density contour results for Mie-Grüneisen fluid and elastic-plastic models are given in Figures 6.5 and 6.9 for times 2.0 and 6.0 micro seconds after impact, respectively. The fundamental shape and speed of the plastic shocks is quite similar to those of the fluid model. However, subtle solution differences are evident between material models. As was the case in one dimension, although not clearly visible in the density contour plots, a leading set of elastic precursor shocks exists in the

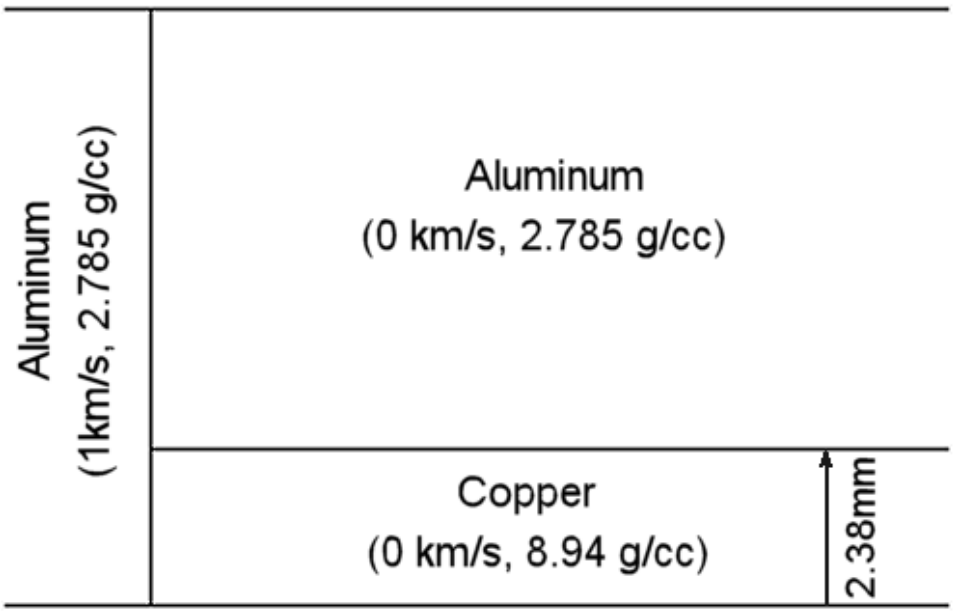

Figure 6.3: Schematic of initial conditions for axisymmetric impact-driven Mach reflection problem

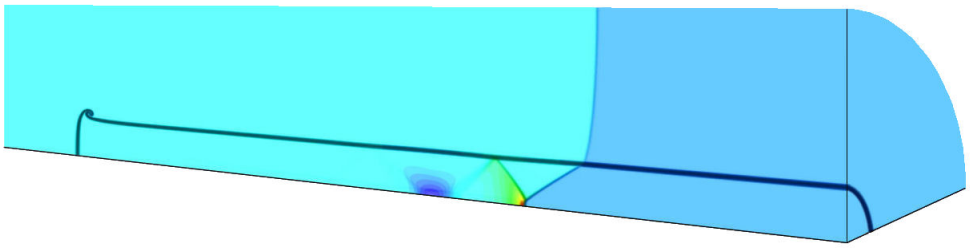

Figure 6.4: Schematic with density contours for Mie-Grüneisen fluid solution to axisymmetric impact-driven Mach reflection problem. The faster shock speed in the outer material drives the formation of a Mach disc in the inner material.

elastic-plastic solution. Regions of plastic deformation are indicated in Figures 6.7 and 6.11 which show the Mandel stress deviator normalized by the yield stress. Figures 6.8 and 6.12 give density and velocity results along the centerline $r = 0$. In these centerlines the leading elastic shock in the copper can be observed. The density and velocity jump across the Mach stem plastic shock are seen to match well between solid and fluid models at the centerline. Behind the Mach stem the reflected wave structures along the centerline give considerable varriation between models. Shear stresses account for most of these observed differences. Roll-up generated at the copper corner at the location of impact for the fluid model simulation is missing in the elastic-plastic simulation. Additionally, the slip line generated at the triple point in the Mach stem in the fluid case appears to be missing in the elastic-plastic case. Figures 6.6 and 6.10 give vorticity plots at time 3.0 and 6.0 micro seconds for the two models presently used. Following the triple point, as is expected, both fluid and solid simulations have some vorticity. However, the vorticity in the fluid model is caried along further from the triple point while the elastic-plastic vorticity is stripped away by shear waves [51]. In light of this, intially following the triple point it may be expected that some "slip" occurs in the elastic-plastic flow through plastic deformation, but is likely eliminated further downstream by shear effects.

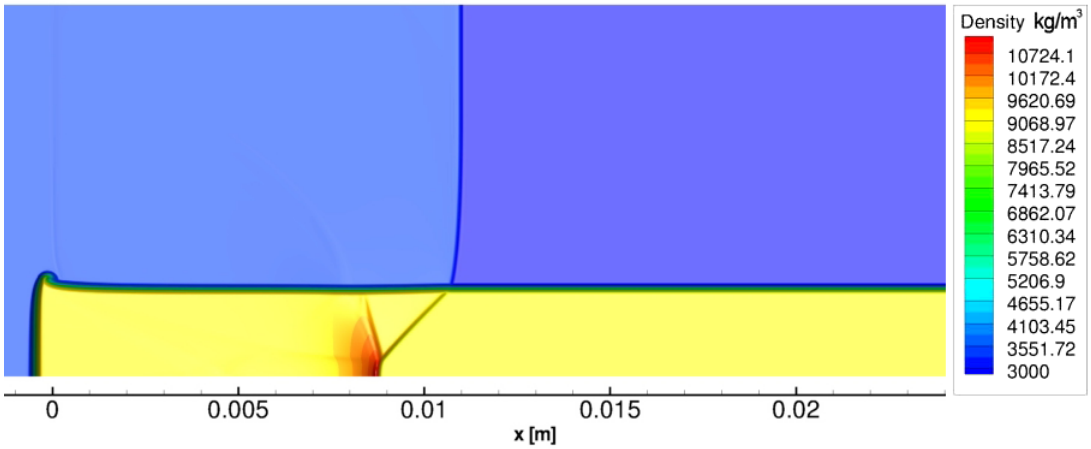

(a)

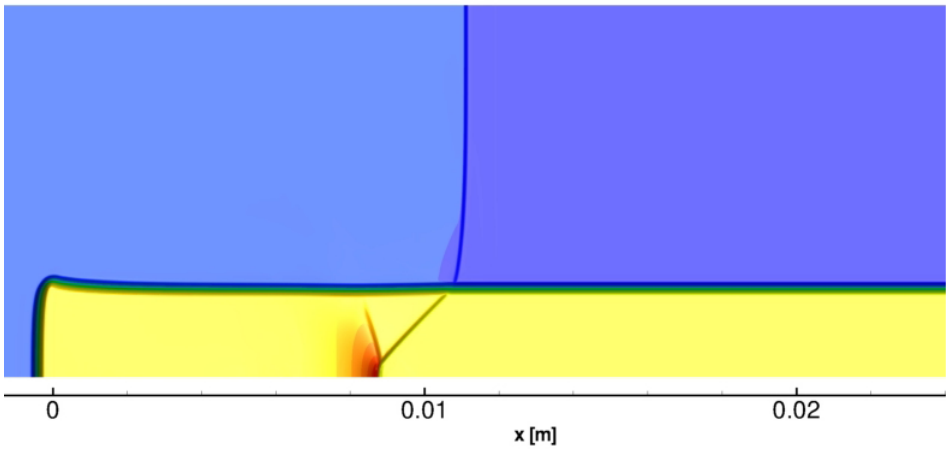

(b)

Figure 6.5: Axisymmetric impact-driven Mach reflection simulation results after 2.0 micro seconds. Density contours for Mie-Grüneisen fluid equation of state (above) and elastic-plastic modified Blatz and Ko model (below)

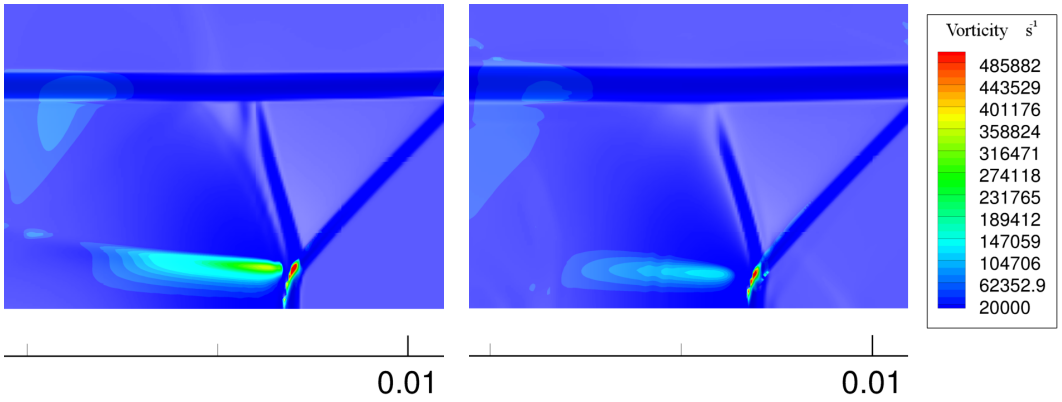

(a) (b)

Figure 6.6: Axisymmetric impact-driven Mach reflection simulation Mach stem vorticity contours at 3.0 micro seconds. (a) Vorticity contours for Mie-Grüneisen fluid equation of state and (b) for the Elastic-plastic modified Blatz and Ko model. The vorticity seen in the Elastic-plastic simulation resides primarily near the triple point. Alternatively, the fluid model allows slip to continue further on behind the triple point.

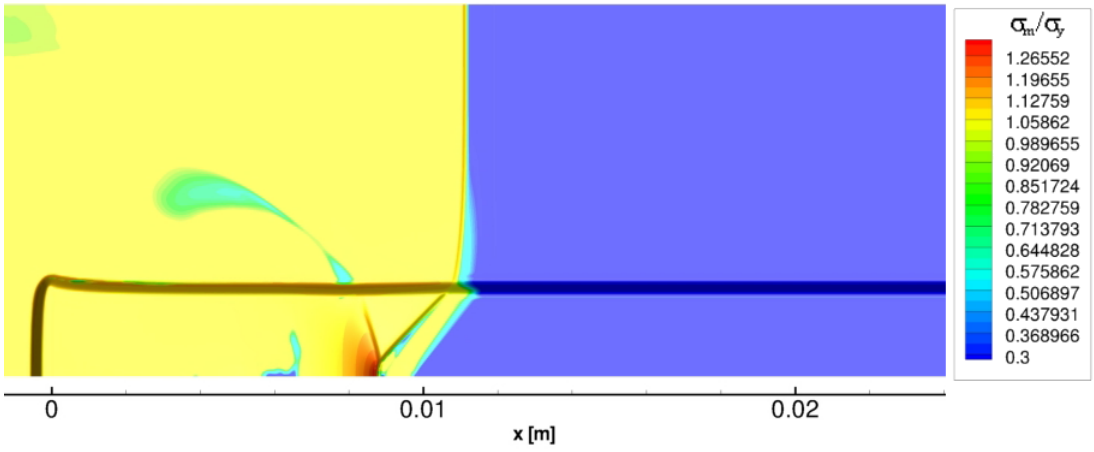

Figure 6.7: Axisymmetric impact-driven Mach reflection simulation elastic-plastic Mandel stress deviator normalized by yield stress after 3.0 micro seconds. The elastic precursor in the inner copper is clearly observable.

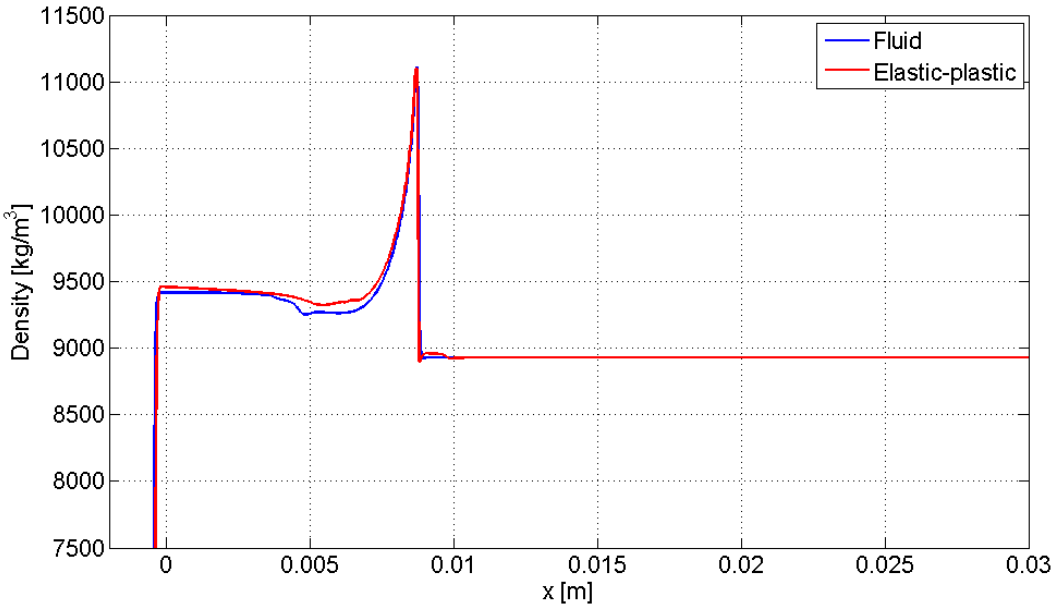

(a)

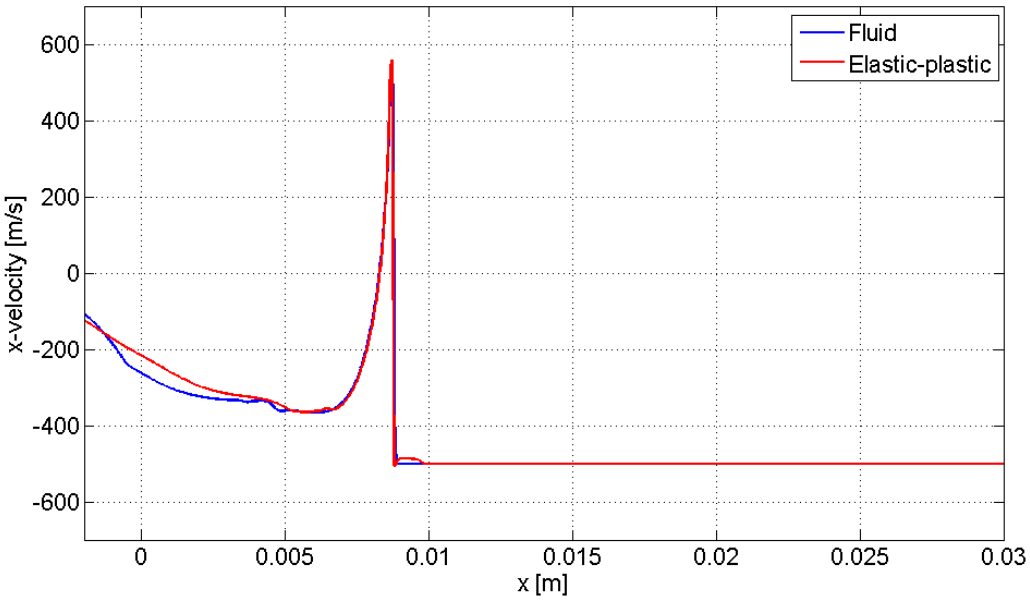

(b)

Figure 6.8: Axisymmetric impact-driven Mach reflection simulation centerline density and x-velocity component after 2.0 micro seconds. Density (above) and x-velocity component (below) for $r = 0$ plotted in blue for the Mie-Grüneisen fluid equation of state and red for the elastic-plastic modified Blatz and Ko model.

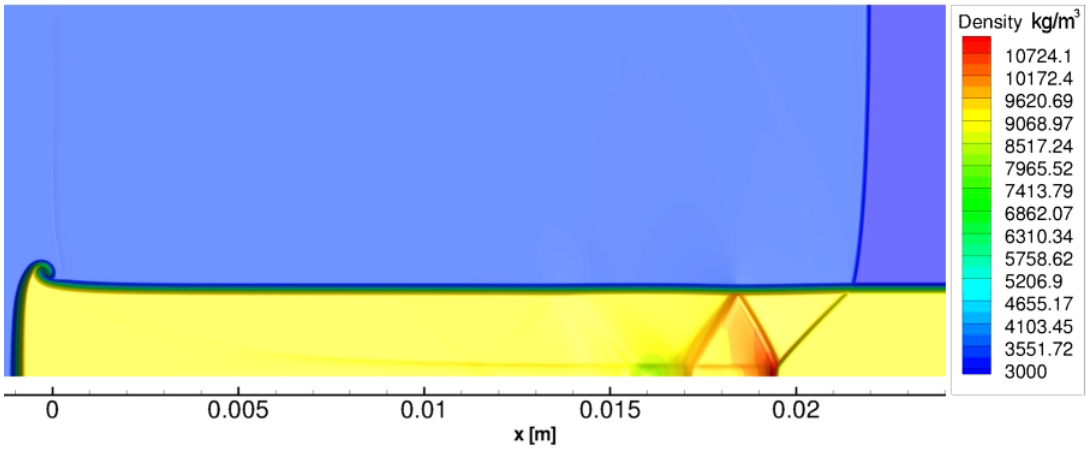

(a)

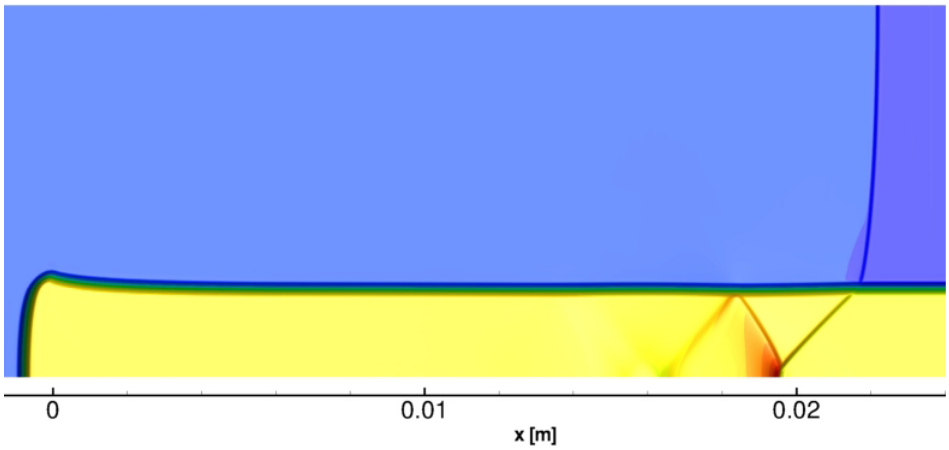

(b)

Figure 6.9: Axisymmetric impact-driven Mach reflection simulation results after 6.0 micro seconds. Density contours for Mie-Grüneisen fluid equation of state (above) and elastic-plastic modified Blatz and Ko model (below)

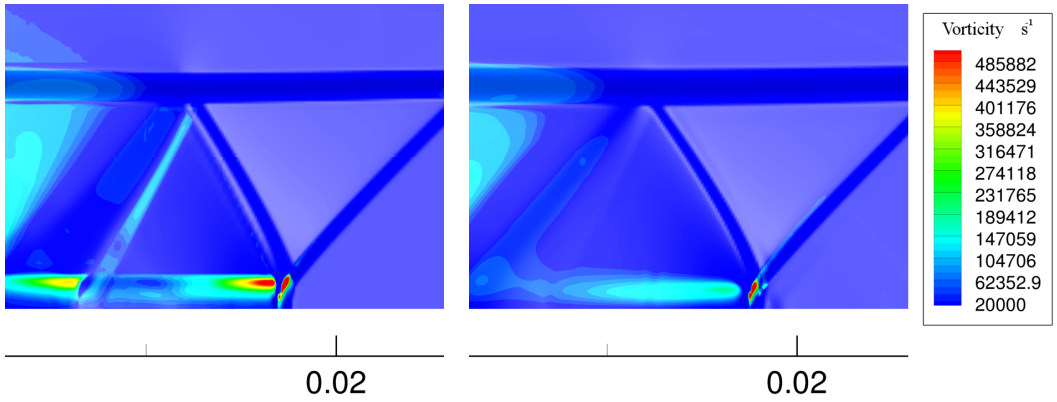

Figure 6.10: Axisymmetric impact-driven Mach reflection simulation Mach stem vorticity contours at 6.0 micro seconds. (a) Vorticity contours for Mie-Grüneisen fluid equation of state and (b) for the Elastic-plastic modified Blatz and Ko model. The vorticity seen in the Elastic-plastic simulation resides primarily near the triple point. Alternatively, the fluid model allows slip to continue further on behind the triple point.

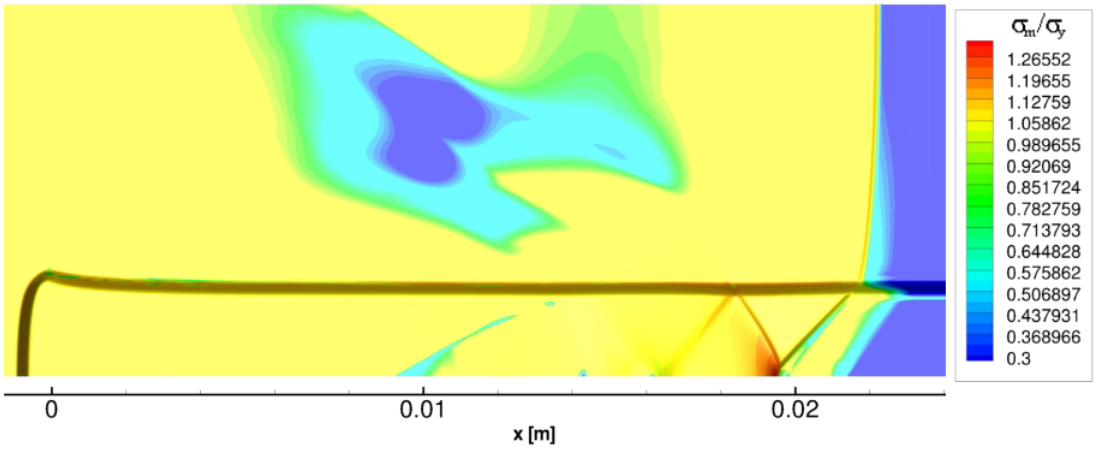

Figure 6.11: Axisymmetric impact-driven Mach reflection simulation elastic-plastic Mandel stress deviator normalized by yield stress after 6.0 micro seconds. The elastic precursor in the inner copper is clearly observable.

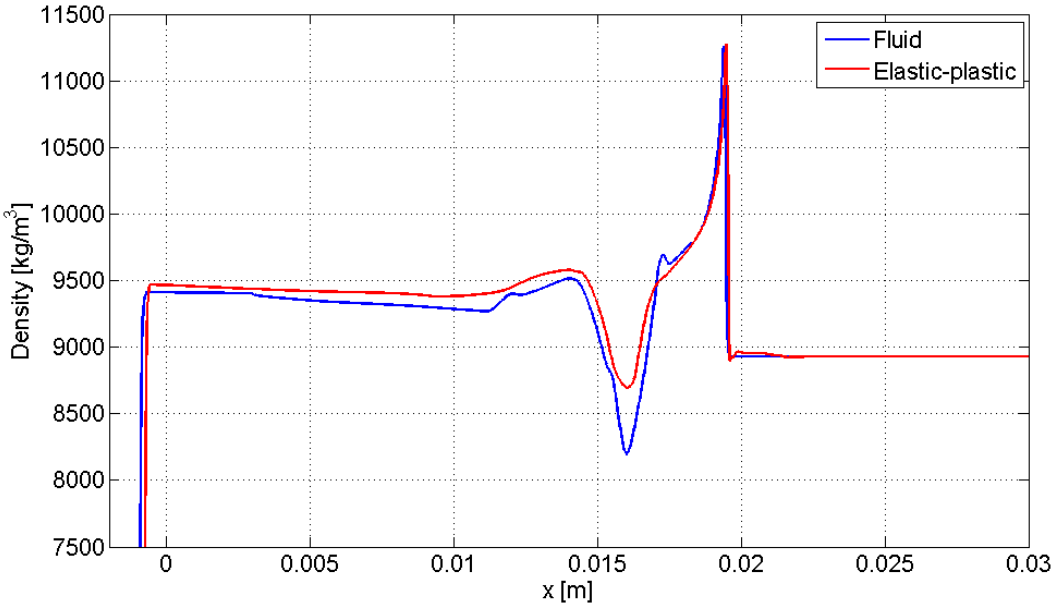

(a)

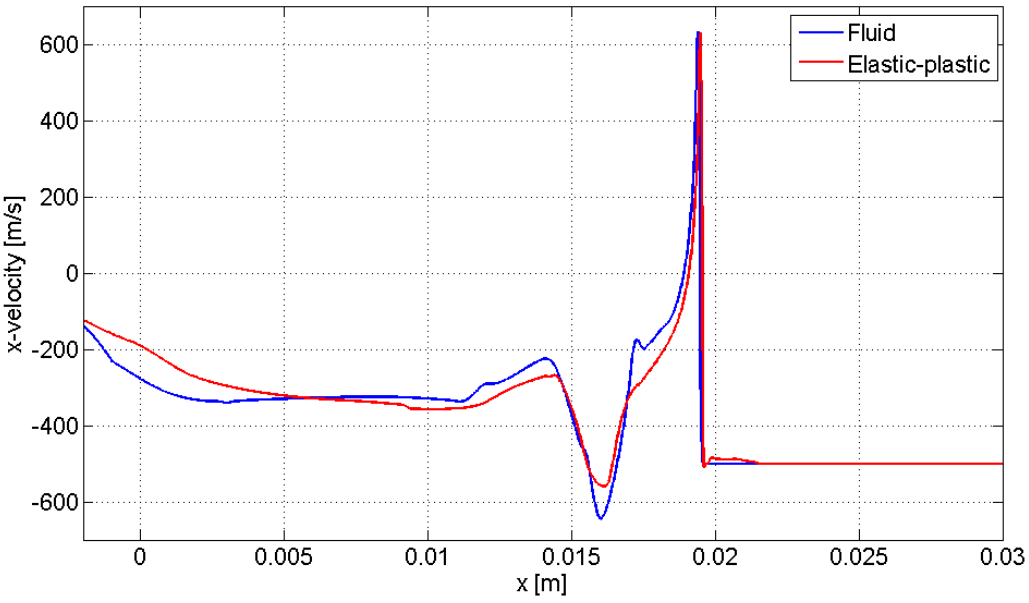

(b)

Figure 6.12: Axisymmetric impact-driven Mach reflection simulation centerline density and x-velocity component after 6.0 micro seconds. Density (above) and x-velocity component (below) for $r = 0$ plotted in blue for the Mie-Grüneisen fluid equation of state and red for the elastic-plastic modified Blatz and Ko model.

Chapter 7

Summary and conclusions

The focus of the research presented in this thesis is on shock and impact-driven flows with Mie-Grüneisen equations of state. Simulations of such Mie-Grüneisen fluids present unique challenges which have been addressed for several flows of interest. Firstly, for multiphase shock driven flows a new hybrid methodology has been developed that allows a skew-symmetric, kinetic-energy preserving, center-difference method to be combined with a shock-capturing Riemann solver, resulting in low numerical dissipation in smooth solution regions while preventing catastrophic oscillations common in flux-splitting schemes. The new method was then applied to explore the role of the equation of state in Richtmyer-Meshkov instability. Simulations of fluids with Mie-Grüneisen equations of state were matched in initial conditions to those with perfect gas models based the post-shock Atwood ratio, the post-shock amplitude-to-wavelength ratio, and a nondimensional pressure jump across the incident shock.

The second portion of the work presented here focuses on the simulation of various free surface impact-driven flows with Mie-Grüneisen equations of state. The ghost fluid method was extended in order to simulate these free surface impact-driven flows. The surface normal Riemann problem solutions were utilized to determine ghost cell values. The method was then applied in one dimension to study a simple impact problem. An extension to multi-dimensions was then applied to study several axisymmetric free surface flows of interest.

The final segment of this thesis was an exploration of the isotropic stress state assumption applied when modeling materials with Mie-Grüneisen equations of state. Several simulations were performed using visco-plastic equation of state models and were compared to those with Mie-Grüneisen equations of state.

7.1 Shock-driven flows

7.1.1 Hybrid limiter methodology

Although previously developed conservative flux-splitting WENO solvers can be tuned to center-differences [65], such solvers fail to maintain the integrity of constant pressure translation solutions and generate catastrophic oscillations in multiphase regions. Alternatively, schemes that address such oscillations by separating phases or tracking additional equations of state related quantities are always upwinding at material interfaces [4, 22, 57, 81]. To circumvent such issues a new generalized set of limiters, based on the deviation of WENO weights from the ideal, has been proposed allowing for smooth transition from high-order center-differences to low-order upwinding methods [90]. The method was first successfully applied to study the linear advection equation.

To demonstrate the methodology a spatially fourth-order version was applied to the multiphase Euler equations with special adaptation for Mie-Grüneisen equations of state in one and two-dimensions. Implementation was performed using the California Institute of Technology's VTF (Virtual Test Facility) AMROC [15–17]. To prevent oscillations in mixtures, a set of redundant primitive quantities that depend on density and scalar mixture fraction were tracked [81]. For the low dissipation scheme a fourth-order, skew-symmetric difference scheme was utilized [65]. Upwinding was achieved by a second-order Roe-Riemann solver blended in with a limiter given by the deviation of weights associated with fifth-order WENO. Temporal discretization was achieved by SSP-TVD third-order Runge-Kutta.

In one dimension, the solver was successfully applied to single-phase and multiphase flows with shock waves. In each case, the limiter adjusts to introduce dissipation at shocks in order to maintain relatively smooth flow on either side. For smooth flows, a fourth-order convergence rate was demonstrated. In two-dimensions, the solver was applied to simulate Mach 2.5 single-mode Richtmyer-Meshkov instability with reshock in MORB and molybdenum modeled by shock-Hugoniot Mie-Grüneisen equations of state. Comparison to third-order WENO demonstrates slightly more resolution in small scale structures at the interface post reshock.

7.1.2 Richtmyer-Meshkov instability comparative study

The present equation of state comparison study of planar Richtmyer-Meshkov instability based on matching the post-shock Atwood ratio, post-shock corrugation shape, time nondimensionalized by Richtmyer's growth rate time constant, and nondimensional pressure difference across the incident shock, reveals several noteworthy differences. Firstly, for the case when a reflected shock occurs, the comparison of results for perfect gases under typical laboratory conditions to results for fluids with linear shock-particle speed central Hugoniot Mie-Grüneisen equations of state demonstrates that differences in compressibility play an important role. The compressibility-driven differences

are most evident in the start-up time and growth rate oscillations, which are observed to be an order of magnitude different between simulations with the presently used flow parameter matching. Additionally, second-order differences are observed in the vorticity distributions shortly after shock-interface interactions due to the nature of the Hugoniot. Vorticity deposition variation, in turn, drives the coherent structure differences observed in the nonlinear growth regime roll-up.

Also of interest are the many similarities that provide useful insight into what information can be extrapolated from results obtained with one equation of state with regard to expectations for another. The prediction of the mixing layer amplitude evolution is of fundamental interest. Despite the delay of growth by the shock driven start-up process, the simulation results presented demonstrate that the nondimensional mixing layer width evolution can be well extrapolated across equations of state for many cases of interest when the nondimensional parameter family

$$(kA^+\Delta vt, \frac{\Delta p}{\rho a_2^2}, A^+, kh_0^+) \tag{7.1}$$

is matched. Furthermore, good agreement is observed in the post-shock corrugation amplitude and centerline spectrum by the present matching for all cases. Some further unexpected similarities are observed for the case of a reflected expansion wave. For such situations the present initial condition matching gives a high level of similarity even for start-up time and oscillation frequencies in spite of the difference in wave speeds. However, this is most likely coincidental and will not hold true for other comparisons based on the same parameter matching.

In assessing how well results from one equation of state predict behavior in another, it is useful to consider the parameters that affect flow similarity. The present comparison results provide insight into which parameter family is required to be matched in order to achieve a high level of flow similarity for inviscid Richtmyer-Meshkov instability with initially small corrugation amplitude. As mentioned before, in general, the generation of full similarity between flows with different equations of state is not likely possible. However, above and beyond the approximate similarity of amplitude afforded by the nondimensional parameters matched in the presented comparison study, the similarities and differences observed indicate that the nondimensional parameter family

$$(\Delta v/V_{s_i}, A^+, h_0/\lambda, a_4/a_5, \frac{dP_{H_1}}{d\rho}\Big|_{\rho_4}/a_4^2, \frac{dP_{H_3}}{d\rho}\Big|_{\rho_5}/a_5^2, \Delta v/a_4, \Delta v/V_{s_4}, \Delta v/V_{s_5}) \tag{7.2}$$

is essential for achieving a high level of flow similarity. Mismatching of any of these parameters can be directly linked to observed differences between perfect gas and Mie-Grüneisen equations of state simulations. For fixed equations of state, this list is considerably longer than the number of nondimensional initial condition paramter choices that can be made.

7.2 Impact-driven flows

A brief examination of the ghost fluid method presented here demonstrates the potential for use in free surface impact-driven flows. The essential solution structures expected are observed in one-dimensional and axisymmetric three-dimensional simulations, however, further work is needed to capture many important features not seen and eliminate unphysical features. A fracture model is minimally needed to attain a realistic prediction for hypervelocity impact problems. Additionally, the thin ligaments observed in the multi-dimensional simulations are most likely numerical in origin rather than physical. Without something like shear strength or surface tension to regularize the length scale associated with shock-wave-generated surface deformations high curvature can arise leading to inadequate surface normal characterization by numerical means.

7.3 Eulerian solids

In Chapter 6, an examination and comparison of nonlinear, elastic-plastic solids to isotropic stress, Mie-Grüneisen fluids are presented. Several important differences were found in a comparison of one-dimensional and axisymmetric three-dimensional simulations. Firstly, in one dimension, the Mie-Grüneisen equation of state was found to model the bulk plastic shock response of the corresponding visco-plastic Blatz and Ko model well by capturing both the shock speed and density jump. However, anisotropic, elastic effects, including elastic precursor shocks, were not captured by the Mie-Grüneisen equation of state. Therefore, at low stress, before plastic effects become dominant, a simple isotropic stress model is not a reasonable approximation.

Additionally, through the axisymmetric simulation of an impact-driven Mach reflection several further important differences due to shear strength were observed. The effect of the visco-plastic model's ability to support shear-stress is most prominently seen at the Mach stem's triple point and material contact. Although vorticity follows behind the triple point in both cases, the slip line following the triple point in the fluid simulation is not observed in the corresponding visco-plastic solution. Likewise, at the copper-aluminum contact, roll-up instability is inhibited and reflected wave structures generated by the Mach stem differ from those seen in the fluid solution. This gives some insight into when meaningful, physical results can be achieved with a simple, isotropic stress model. In particular, for the Richtmyer-Meshkov instability simulations presented for isotropic stress Mie-Grüneisen equations of state to be physically accurate, the incident shock must be sufficiently strong to yield plastic deformation and the contact between materials should be well modeled by nearly perfect slip for the solution to be considered valid for times beyond some timescale associated with the material shear strength and the angular deformation generated by the vorticity deposition of the incident shock.

Appendix A

Axisymmetric equations of motions

A.1 Mie-Grüneisen equation of state

For flows which are axisymmetric the single fluid one-dimensional Euler equations can be written in the form (see [86])

$$\frac{\partial \mathbf{q}}{\partial t} + \frac{\partial \mathbf{F}(\mathbf{q})}{\partial z} + \frac{\partial \mathbf{G}(\mathbf{q})}{\partial r} = \mathbf{S}(\mathbf{q}), \tag{A.1}$$

where

$$\mathbf{F}(\mathbf{q}) = \begin{pmatrix} \rho v_z \\ \rho v_z^2 + p \\ \rho v_r v_z \\ v_z(\rho E + p) \end{pmatrix}, \mathbf{G}(\mathbf{q}) = \begin{pmatrix} \rho v_r \\ \rho v_r v_z \\ \rho v_r^2 + p \\ v_r(\rho E + p) \end{pmatrix}, \mathbf{S}(\mathbf{q}) = -\frac{1}{r} \begin{pmatrix} \rho v_r \\ \rho v_r v_z \\ \rho v_r^2 \\ v_r(\rho E + p) \end{pmatrix}, \tag{A.2}$$

with conserved vector of state $\mathbf{q}$ defined by

$$\mathbf{q} = (\rho, \rho v_z, \rho v_r, \rho E). \tag{A.3}$$

Subscripted z and r denote velocity components along the axisymmetric and radial coordinates, respectively. The total energy per unit mass is denoted by E, with $E = e + \frac{1}{2}(v_z^2 + v_r^2)$.

For multiphase flows with Mie-Grüneisen equations of state it is useful to track additional variables in primitive form such as in equation (3.24). For axisymmetric flows the primitive evolution equations for scalars and general functions of density follow directly from conservation of mass. For a scalar ψ the axisymmetric primitive evolution equations are simply

$$\frac{\partial \psi}{\partial t} + v_z \frac{\partial \psi}{\partial z} + v_r \frac{\partial \psi}{\partial r} = 0. \tag{A.4}$$

Alternatively, for a simple function of density $g(\rho)$ the axisymmetric primitive evolution equation is

given by

$$\frac{\partial g(\rho)}{\partial t} + v_z \frac{\partial g(\rho)}{\partial z} + v_r \frac{\partial g(\rho)}{\partial r} = -\rho g'(\rho)\Big(\frac{\partial v_z}{\partial z} + \frac{\partial v_r}{\partial r}\Big) - \frac{1}{r}\rho v_r g'(\rho), \tag{A.5}$$

with $g'(\rho) = dg(\rho)/d\rho$. For application to numerical simulation of fluids with Mie-Grüneisen equations of state $g(\rho) \rightarrow 1/\Gamma_{_H}(\rho)$, $p_{_H}(\rho)/\Gamma_{_H}(\rho)$, and $\rho e_{_H}(\rho)$.

A.2 Nonlinear elastic-plastic

Conversion of (6.15) through (6.21) to any locally orthogonal coordinate system is relatively straightforward. Each vector and tensor must simply be rotated into the local orthogonal coordinates accordingly and chain rule differentiation applied. For example, consider the conversion of the evolution equation for the inverse deformation gradient tensor (6.19) into polar coordinates (r, θ, ζ) related to Cartesian coordinates (x, y, z) by

$$x = r\cos(\theta) \tag{A.6}$$

$$y = r\sin(\theta) \tag{A.7}$$

$$z = \zeta. \tag{A.8}$$

The physical components of any tensor in Cartesian coordinates are related to those in polar coordinates through directional Cosines R_{ij},

$$\mathbf{R} = \begin{bmatrix} \cos(\theta) & -\sin(\theta) & 0 \\ \sin(\theta) & \cos(\theta) & 0 \\ 0 & 0 & 1 \end{bmatrix}, \tag{A.9}$$

with the property that $R^{-1} = R^T$. For the second-order inverse deformation gradient tensor the Cartesian coordinate components f_{ij} are related to the polar coordinate components $\overline{f}_{ij}$ by

$$\mathbf{f} = \mathbf{R}\bar{\mathbf{f}}\mathbf{R}^{\mathbf{T}}. \tag{A.10}$$

Likewise the velocity components are related by

$$\mathbf{u} = \mathbf{R}\overline{\mathbf{u}}. \tag{A.11}$$

The evolution of the inverse deformation gradient is then

$$\frac{\partial(\overline{f}_{il} R_{ki} R_{jl})}{\partial t} + \frac{\partial(R_{kj}\overline{f}_{ji}\overline{u}_i)}{\partial x_j} = 0, \tag{A.12}$$

or equivalently

$$\frac{\partial(\mathbf{R}\bar{\mathbf{f}}\mathbf{R}^{\mathbf{T}})}{\partial t} + \left[\begin{array}{ccc} \frac{\partial(\mathbf{R}\bar{\mathbf{f}}\bar{\mathbf{u}})}{\partial x} & \frac{\partial(\mathbf{R}\bar{\mathbf{f}}\bar{\mathbf{u}})}{\partial y} & \frac{\partial(\mathbf{R}\bar{\mathbf{f}}\bar{\mathbf{u}})}{\partial z} \end{array} \right] = \mathbf{0}. \tag{A.13}$$

Applying the chain rule to this equation gives

$$\frac{\partial(\mathbf{R}\bar{\mathbf{f}}\mathbf{R}^{\mathbf{T}})}{\partial t} + \left[\begin{array}{ccc} \frac{\partial(\mathbf{R}\bar{\mathbf{f}}\bar{\mathbf{u}})}{\partial r} & \frac{\partial(\mathbf{R}\bar{\mathbf{f}}\bar{\mathbf{u}})}{\partial \theta} & \frac{\partial(\mathbf{R}\bar{\mathbf{f}}\bar{\mathbf{u}})}{\partial z} \end{array} \right] \mathbf{J}^{-\mathbf{1}} = \mathbf{0}, \tag{A.14}$$

where $\mathbf{J}$ is the coordinate system Jacobian,

$$\mathbf{J} = \left[\begin{array}{ccc} \cos(\theta) & -r\sin(\theta) & 0 \\ \sin(\theta) & r\cos(\theta) & 0 \\ 0 & 0 & 1 \end{array} \right]. \tag{A.15}$$

This simplifies to the evolution equation for the physical components of the inverse deformation gradient in polar coordinates,

$$\frac{\partial \bar{\mathbf{f}}}{\partial t} + \mathbf{R}^{\mathbf{T}} \left[\begin{array}{ccc} \frac{\partial(\mathbf{R}\bar{\mathbf{f}}\bar{\mathbf{u}})}{\partial r} & \frac{\partial(\mathbf{R}\bar{\mathbf{f}}\bar{\mathbf{u}})}{\partial \theta} & \frac{\partial(\mathbf{R}\bar{\mathbf{f}}\bar{\mathbf{u}})}{\partial z} \end{array} \right] \mathbf{J}^{-\mathbf{1}}\mathbf{R} = \mathbf{0}. \tag{A.16}$$

Expanding out (A.16) and setting $\frac{\partial}{\partial \theta}(\cdot) = 0$ and $u_\theta = 0$ for axisymmetric purposes yields

$$\frac{\partial}{\partial t} \left[\begin{array}{c} \bar{\mathbf{f}}\mathbf{e_r} \\ \bar{\mathbf{f}}\mathbf{e}_\theta \\ \bar{\mathbf{f}}\mathbf{e_z} \end{array} \right] + \frac{\partial}{\partial r} \left[\begin{array}{c} \bar{\mathbf{f}}\bar{\mathbf{u}} \\ \mathbf{0} \\ \mathbf{0} \end{array} \right] + \frac{\partial}{\partial z} \left[\begin{array}{c} \mathbf{0} \\ \mathbf{0} \\ \bar{\mathbf{f}}\bar{\mathbf{u}} \end{array} \right] = \frac{1}{r} \left[\begin{array}{c} \mathbf{0} \\ (\overline{f}_{\theta r}u_r + \overline{f}_{\theta z}u_z, -\overline{f}_{rr}u_r - \overline{f}_{rz}u_z, 0)^T \\ \mathbf{0} \end{array} \right]. \tag{A.17}$$

Further details concerning the conversion of the rest of the equations of motion for axisymmetric problems is omitted The results from conversion to axisymmetric situations are now summarized beginning with continuity:

$$\frac{\partial \rho}{\partial t} + \frac{\partial(\rho u_r)}{\partial r} + \frac{\partial(\rho u_z)}{\partial z} = -\frac{1}{r}\rho u_r. \tag{A.18}$$

Conservation of momentum:

$$\begin{aligned} \frac{\partial \rho u_r}{\partial t} + \frac{\partial(\rho u_r^2)}{\partial r} + \frac{\partial(\rho u_r u_z)}{\partial z} + \frac{\partial \sigma_{rr}}{\partial r} + \frac{\partial \sigma_{zr}}{\partial z} &= \frac{1}{r}(\sigma_{rr} - \sigma_{\theta\theta}), & \text{(A.19)} \\ \frac{\partial \rho u_z}{\partial t} + \frac{\partial(\rho u_r u_z)}{\partial r} + \frac{\partial(\rho u_z^2)}{\partial z} + \frac{\partial \sigma_{rz}}{\partial r} + \frac{\partial \sigma_{zz}}{\partial z} &= \frac{1}{r}(\sigma_{rz}). & \text{(A.20)} \end{aligned}$$

Conservation of energy:

$$\frac{\partial(\rho E)}{\partial t} + \frac{\partial(\rho u_r E)}{\partial r} + \frac{\partial(\rho u_z E)}{\partial z} + \frac{\partial(u_r\sigma_{rr} + u_z\sigma_{rz})}{\partial r} + \frac{\partial(u_r\sigma_{zr} + u_z\sigma_{zz})}{\partial z} = -\frac{1}{r}(u_r\rho E - u_z\sigma_{rz} - u_r\sigma_{rr}), \tag{A.21}$$

where $E = e + \frac{1}{2}(u_r^2 + u_z^2)$. The components of the plastic part of the deformation tensor are advected like scalars:

$$\frac{\partial(\rho F_{ij}^p)}{\partial t} + \frac{\partial(\rho u_r F_{ij}^p)}{\partial x_r} + \frac{\partial(\rho u_z F_{ij}^p)}{\partial x_z} = \rho L_{ik}^p F_{kj}^p - \frac{1}{r}\rho u_r F_{ij}^p. \tag{A.22}$$

Also of interest for numerical purposes is the term $\mathbf{u} \times \nabla \times \mathbf{f^T}$:

$$\mathbf{u} \times \nabla \times \mathbf{f^T} = \begin{bmatrix} u_z \frac{\partial f_{rz}}{\partial r} - u_z \frac{\partial f_{rr}}{\partial z} & -u_r \frac{\partial f_{r\theta}}{\partial r} - u_z \frac{\partial f_{r\theta}}{\partial z} - \frac{u_r(f_{r\theta}+f_{\theta r})+u_z f_{rz}}{r} & u_r \frac{\partial f_{rr}}{\partial z} - u_r \frac{\partial f_{rz}}{\partial r} \\ u_z \frac{\partial f_{\theta z}}{\partial r} - u_z \frac{\partial f_{\theta r}}{\partial z} & -u_r \frac{\partial f_{\theta\theta}}{\partial r} - u_z \frac{\partial f_{\theta\theta}}{\partial z} + \frac{u_r(f_{rr}-f_{\theta\theta})+u_z f_{rz}}{r} & u_r \frac{\partial f_{\theta r}}{\partial z} - u_r \frac{\partial f_{\theta z}}{\partial r} \\ u_z \frac{\partial f_{zz}}{\partial r} - u_z \frac{\partial f_{zr}}{\partial z} & -u_r \frac{\partial f_{z\theta}}{\partial r} - u_z \frac{\partial f_{z\theta}}{\partial z} & u_r \frac{\partial f_{zr}}{\partial z} - u_r \frac{\partial f_{zz}}{\partial r} \end{bmatrix}. \tag{A.23}$$

Bibliography

[1] S.I. Abarzhi. A new type of the evolution of the bubble front in the Richtmyer-Meshkov instability. *Physics Letters A*, 294(2):95–100, 2002.

[2] R. Abgrall. How to prevent pressure oscillations in multicomponent flow calculations: a quasi conservative approach. *Journal of Computational Physics*, 125(1):150–160, 1996.

[3] N.A. Adams and K. Shariff. A high-resolution hybrid compact-ENO scheme for shock-turbulence interaction problems. *Journal of Computational Physics*, 127(1):27–51, 1996.

[4] G. Allaire, S. Clerc, and S. Kokh. A five-equation model for the simulation of interfaces between compressible fluids. *Journal of Computational Physics*, 181(2):577–616, 2002.

[5] R. Aris. *Vectors, tensors, and the basic equations of fluid mechanics*. Dover Publications, 1989.

[6] D.S. Balsara and C.W. Shu. Monotonicity preserving weighted essentially non-oscillatory schemes with increasingly high order of accuracy. *Journal of Computational Physics*, 160(2):405–452, 2000.

[7] P.T. Barton and D. Drikakis. An Eulerian method for multi-component problems in non-linear elasticity with sliding interfaces. *Journal of Computational Physics*, 2010.

[8] P.T. Barton, D. Drikakis, and E.I. Romenski. An Eulerian finite-volume scheme for large elasto-plastic deformations in solids. *International Journal for Numerical Methods in Engineering*, 81(4):453–484, 2010.

[9] M.J. Berger and P. Colella. Local adaptive mesh refinement for shock hydrodynamics. *Journal of computational Physics*, 82(1):64–84, 1989.

[10] M.J. Berger and J.E. Oliger. Adaptive mesh refinement for hyperbolic partial differential equations. 1983.

[11] J.L. Brown and G. Ravichandran. Shockwaves in converging geometries. In *AIP Conference Proceedings*, volume 1195, page 747, 2009.

[12] M.H. Carpenter, D. Gottlieb, and S. Abarbanel. The stability of numerical boundary treatments for compact high-order finite-difference schemes. *Journal of computational physics*, 108(2):272–295, 1993.

[13] P. Colella. Direct Eulerian MUSCL scheme for gas dynamics. *SIAM Journal of Science and Statistical Computing*, 6(1):104–117, 1985.

[14] B.D. Collins and J.W. Jacobs. PLIF flow visualization and measurements of the Richtmyer–Meshkov instability of an air/SF6 interface. *Journal of Fluid Mechanics*, 464:113–136, 2002.

[15] J. Cummings, M. Aivazis, R. Samtaney, R. Radovitzky, S. Mauch, and D.I. Meiron. A virtual test facility for the simulation of dynamic response in materials. *The Journal of Supercomputing*, 23(1):39–50, 2001.

[16] R. Deiterding. *Parallel adaptive simulation of multi-dimensional detonation structures.* PhD thesis, Brandenburgische Technische Universität Cottbus, Sep 2003.

[17] R. Deiterding. Construction and application of an AMR algorithm for distributed memory computers. In Timur Plewa, Linde and V. Gregory Weirs, editors, *Adaptive Mesh Refinement: Theory and Applications*, volume 41 of *Lecture Notes in Computational Science and Engineering*, pages 361–372. Springer, 2005.

[18] M. Dumbser, J.M. Moschetta, and J. Gressier. A matrix stability analysis of the carbuncle phenomenon. *Journal of Computational Physics*, 197(2):647–670, 2004.

[19] S.P. D'yakov. On the stability of shock waves. *Z. Eksper. Teoret. Fiz*, 27:288–295, 1954.

[20] B. Engquist and B. Sj
"ogreen. The convergence rate of finite difference schemes in the presence of shocks. *SIAM Journal on Numerical Analysis*, 35(6):2464–2485, 1998.

[21] G. Fairweather. *Finite element Galerkin methods for differential equations.* M. Dekker, 1978.

[22] R.P. Fedkiw, T. Aslam, B. Merriman, and S. Osher. A non-oscillatory Eulerian approach to interfaces in multimaterial flows (the ghost fluid method). *Journal of Computational Physics*, 152(2):457–492, 1999.

[23] V.N. Goncharov. Analytical model of nonlinear, single-mode, classical Rayleigh-Taylor instability at arbitrary Atwood numbers. *Physical review letters*, 88(13):134502, 2002.

[24] S. Gottlieb, C.W. Shu, and E. Tadmor. Strong stability-preserving high-order time discretization methods. *SIAM review*, pages 89–112, 2001.

[25] J.W. Grove, R. Holmes, D.H. Sharp, Y. Yang, and Q. Zhang. Quantitative theory of Richtmyer-Meshkov instability. *Physical Review Letters*, 71(21):3473–3476, 1993.

[26] D. Hartmann, M. Meinke, and W. Schröder. Differential equation based constrained reinitialization for level set methods. *Journal of Computational Physics*, 227(14):6821–6845, 2008.

[27] G. Hazak. Lagrangian formalism for the rayleigh-taylor instability. *Physical Review Letters*, 76(22):4167–4170, May 1996.

[28] D.J. Hill. Eulerian Solids for the Fluid Mechanic: Working notes for the fluids group. 2010.

[29] D.J. Hill and D.I. Pullin. Hybrid tuned center-difference-weno method for large eddy simulations in the presence of strong shocks. *Journal of Computational Physics*, 194(2):435–450, 2004.

[30] D.J. Hill, D.I. Pullin, M. Ortiz, and D.I. Meiron. A Conservative Three-Dimensional Eulerian Method for Coupled Solid-Fluid Shock Capturing. *Journal of Computational Physics*, 2010.

[31] R. Hill. *The mathematical theory of plasticity*. Oxford University Press, USA, 1998.

[32] A.C. Hindmarsh. ODEPACK, a systematized collection of ODE solvers. *North-Holland, Amsterdam*, 1:55–64, 1983.

[33] R.L. Holmes, G. Dimonte, B. Fryxell, M.L. Gittings, J.W. Grove, M. Schneider, D.H. Sharp, A.L. Velikovich, R.P. Weaver, and Q. Zhang. Richtmyer–Meshkov instability growth: experiment, simulation and theory. *Journal of Fluid Mechanics*, 389:55–79, 1999.

[34] J.W. Jacobs and V.V. Krivets. Experiments on the late-time development of single-mode Richtmyer–Meshkov instability. *Physics of Fluids*, 17:034105, 2005.

[35] J.W. Jacobs and J.M. Sheeley. Experimental study of incompressible Richtmyer–Meshkov instability. *Physics of Fluids*, 8:405, 1996.

[36] R. Jeanloz. Shock wave equation of state and finite strain theory. *Journal of Geophysics Research*, 94:5873–5886, 1989.

[37] G.S. Jiang and C.W. Shu. Efficient implementation of weighted ENO schemes. *Journal of Computational Physics*, 126:202–228, 1996.

[38] E. Johnsen and T. Colonius. Implementation of weno schemes in compressible multicomponent flow problems. *Journal of Computational Physics*, 219(2):715–732, 2006.

[39] M.A. Jones and J.W. Jacobs. A membraneless experiment for the study of Richtmyer–Meshkov instability of a shock-accelerated gas interface. *Physics of Fluids*, 9:3078, 1997.

[40] E.H. Kennard. *Kinetic theory of gases*, volume 304. McGraw-Hill New York, 1938.

[41] R.M.J. Kramer, D.I. Pullin, D.I. Meiron, and C. Pantano. Shock-resolved Navier–Stokes simulation of the Richtmyer–Meshkov instability start-up at a light–heavy interface. *Journal of Fluid Mechanics*, 642:421, 2009.

[42] L.D. Landau and E.M. Lifshitz. *Course of theoretical physics. vol. 6: Fluid mechanics.* London, 1987.

[43] M. Latini, O. Schilling, and W.S. Don. Effects of WENO flux reconstruction order and spatial resolution on reshocked two-dimensional Richtmyer–Meshkov instability. *Journal of Computational Physics*, 221(2):805–836, 2007.

[44] D. Layzer. On the Instability of Superposed Fluids in a Gravitational Field. *The astrophysical journal*, 122:1, 1955.

[45] R.J. LeVeque. *Numerical methods for conservation laws.* Birkhäuser, 1992.

[46] R.J. LeVeque. *Finite volume methods for hyperbolic problems.* Cambridge university press, 2002.

[47] H.W. Liepmann and A. Roshko. *Elements of gasdynamics.* Dover Publications, 2001.

[48] X.D. Liu, S. Osher, and T. Chan. Weighted essentially non-oscillatory schemes. *Journal of Computational Physics*, 115(1):200–212, 1994.

[49] M. Lombardini. *Richtmyer-Meshkov instability in converging geometries.* PhD thesis, 2008.

[50] M. Lombardini and D.I. Pullin. Startup process in the Richtmyer–Meshkov instability. *Physics of Fluids*, 21:044104, 2009.

[51] A. López Ortega, D.J. Hill, D.I. Pullin, and D.I. Meiron. Linearized Richtmyer-Meshkov flow analysis for impulsively accelerated incompressible solids. *Physical Review E*, 81(6):66305, 2010.

[52] R.G. McQueen, S.P. Marsh, J.W. Taylor, J.N. Fritz, and W.J. Carter. The equation of state of solids from shock wave studies. *High Velocity Impact Phenomena*, pages 294–417, 1970.

[53] E.E. Meshkov. Instability of the interface of two gases accelerated by a shock wave. *Fluid Dynamics*, 4(5):101–104, 1969.

[54] K.A. Meyer and P.J. Blewett. Numerical Investigation of the Stability of a Shock-Accelerated Interface between Two Fluids. *Physics of Fluids*, 15:753, 1972.

[55] G.H. Miller and P. Colella. A High-Order Eulerian Godunov Method for Elastic-Plastic Flow in Solids. *Journal of Computational Physics*, 167(1):131–176, 2001.

[56] G.H. Miller and P. Colella. A Conservative Three-Dimensional Eulerian Method for Coupled Solid-Fluid Shock Capturing. *Journal of Computational Physics*, 183(1):26–82, 2002.

[57] G.H. Miller and E.G. Puckett. A high-order godunov method for multiple condensed phases. *Journal of Computational Physics*, 128(1):134–164, 1996.

[58] P. Moin and K. Mahesh. Direct numerical simulation: a tool in turbulence research. *Annual Review of Fluid Mechanics*, 30(1):539–578, 1998.

[59] E. Morano and R. Sanders. Carbuncle phenomenon: On upwind schemes in multidimensions*. *Comptes Rendus de l'Académie des Sciences Series IIB Mechanics Physics Chemistry Astronomy*, 325(6):339–346, 1997.

[60] C.E. Niederhaus and J.W. Jacobs. Experimental study of the Richtmyer–Meshkov instability of incompressible fluids. *Journal of Fluid Mechanics*, 485:243–277, 2003.

[61] B.J. Olson and A.W. Cook. Rayleigh–Taylor shock waves. *Physics of Fluids*, 19:128108, 2007.

[62] A. Ortiz, MA Puso, and N. Sukumar. Maximum-entropy meshfree method for compressible and near-incompressible elasticity. *Computer Methods in Applied Mechanics and Engineering*, 199(25-28):1859–1871, 2010.

[63] S. Osher and R.P. Fedkiw. *Level set methods and dynamic implicit surfaces*. Springer Verlag, 2003.

[64] S. Osher and J.A. Sethian. Fronts propagating with curvature-dependent speed: algorithms based on Hamilton-Jacobi formulations. *Journal of computational physics*, 79(1):12–49, 1988.

[65] C. Pantano, R. Deiterding, D.J. Hill, and D.I. Pullin. A low-numerical dissipation, patch-based adaptive-mesh-refinement method for large-eddy simulation of compressible flows. *Journal of Computational Physics*, 2006.

[66] P. Perzyna. Fundamental problems in viscoplasticity. *Advances in applied mechanics*, 9(2):244–368, 1966.

[67] P. Perzyna. Thermodynamic theory of viscoplasticity. *Advances in Applied Mechanics*, 11:313–354, 1971.

[68] S. Pirozzoli. Conservative hybrid compact-WENO schemes for shock-turbulence interaction. *Journal of Computational Physics*, 178(1):81–117, 2002.

[69] J.J. Quirk. A contribution to the great Riemann solver debate. *International Journal for numerical methods in fluids*, 18(6), 1994.

[70] K. Radhakrishnan and A.C. Hindmarsh. Description and use of LSODE, the Livemore Solver for Ordinary Differential Equations. Technical report, Lawrence Livermore National Laboratory (LLNL), Livermore, CA, 1993.

[71] R.D. Richtmyer. Taylor instability in shock acceleration of compressible fluids. Technical report, LA-1914 (del.), Los Alamos Scientific Lab., N. Mex., 1954.

[72] P.L. Roe. Approximate Riemann solvers, parameter vectors, and difference schemes. *Journal of computational physics*, 135(2):250–258, 1997.

[73] L. Rowan. *1. Equation of State of Molten Mid-Ocean Ridge Basalt; II. Structure of Kilauea Volcano*. PhD thesis, Ph. D. Dissertation thesis, pp., California Institute of Technology, Pasadena, CA, 1993.

[74] D.H. Rudy and J.C. Strikwerda. A nonreflecting outflow boundary condition for subsonic Navier-Stokes calculations. *Journal of Computational Physics*, 36(1):55–70, 1980.

[75] G. Russo and P. Smereka. A remark on computing distance functions. *Journal of Computational Physics*, 163(1):51–67, 2000.

[76] R. Samtaney and N.J. Zabusky. Circulation deposition on shock-accelerated planar and curved density-stratified interfaces: models and scaling laws. *Journal of Fluid Mechanics*, 269(45-78):2, 1994.

[77] R. Sanders, E. Morano, and M.C. Druguet. Multidimensional dissipation for upwind schemes: stability and applications to gas dynamics. *Journal of Computational Physics*, 145(2):511–537, 1998.

[78] L.I. Sedov and T. Scripta. *Introduction to the Mechanics of a Continuous Medium*. Addison-Wesley, 1965.

[79] C.W. Shu, Institute for Computer Applications in Science, and Engineering. Essentially non-oscillatory and weighted essentially non-oscillatory schemes for hyperbolic conservation laws. *LECTURE NOTES IN MATHEMATICS-SPRINGER VERLAG-*, pages 325–432, 1998.

[80] K.M. Shyue. A fluid-mixture type algorithm for compressible multicomponent flow with van der waals equation of state. *Journal of Computational Physics*, 156:43–88, 1999.

[81] K.M. Shyue. A fluid-mixture type algorithm for compressible multicomponent flow with mie-gruneisen equation of state. *Journal of Computational Physics*, 171(2):678–707, 2001.

[82] S.I. Sohn. Simple potential-flow model of Rayleigh-Taylor and Richtmyer-Meshkov instabilities for all density ratios. *Physical Review E*, 67(2):26301, 2003.

[83] M. Sussman, P. Smereka, and S. Osher. A level set approach for computing solutions to incompressible two-phase flow. *Journal of computational Physics*, 114(1):146–159, 1994.

[84] K.W. Thompson. Time-dependent boundary conditions for hyperbolic systems, II. *Journal of Computational Physics*, 89(2):439–461, 1990.

[85] P.A. Thompson and A.A. Sonin. Compressible-Fluid Dynamics. *Physics Today*, 26:65, 1973.

[86] E.F. Toro. *Riemann solvers and numerical methods for fluid dynamics: a practical introduction*. Springer Verlag, 2009.

[87] EF Toro, M. Spruce, and W. Speares. Restoration of the contact surface in the HLL-Riemann solver. *Shock waves*, 4(1):25–34, 1994.

[88] B. Van Leer. Towards the ultimate conservative difference scheme. IV. A new approach to numerical convection. *Journal of Computational Physics*, 23(3):276–299, 1977.

[89] M. Vetter and B. Sturtevant. Experiments on the Richtmyer-Meshkov instability of an air/SF 6 interface. *Shock Waves*, 4(5):247–252, 1995.

[90] G.M. Ward and D.I. Pullin. A hybrid, center-difference, limiter method for simulations of compressible multicomponent flows with mie-grüneisen equation of state. *Journal of Computational Physics*, 2010.

[91] G. Weber and L. Anand. Finite deformation constitutive equations and a time integration procedure for isotropic, hyperelastic-viscoplastic solids. *Computer Methods in Applied Mechanics and Engineering*, 79(2):173–202, 1990.

[92] G.B. Whitham and GB Whitham. *Linear and nonlinear waves*. Wiley New York, 1974.

[93] J.G. Wouchuk. Growth rate of the linear Richtmyer-Meshkov instability when a shock is reflected. *Physical Review E*, 63(5):56303, 2001.

[94] J.G. Wouchuk and K. Nishihara. Asymptotic growth in the linear Richtmyer-Meshkov instability. *Physics of Plasmas*, 4(4):1028–1038, 1997.

[95] Y. Yang, Q. Zhang, and D.H. Sharp. Small amplitude theory of Richtmyer–Meshkov instability. *Physics of Fluids*, 6:1856, 1994.

[96] Y.B. Zel'Dovich and Y.P. Raizer. *Physics of shock waves and high-temperature hydrodynamic phenomena*. Dover Publications, 2002.

[97] Q. Zhang. Analytical solutions of Layzer-type approach to unstable interfacial fluid mixing. *Physical Review Letters*, 81(16):3391–3394, 1998.

[98] Q. Zhang and S.I. Sohn. An analytical nonlinear theory of Richtmyer-Meshkov instability. *Physics Letters A*, 212(3):149–155, 1996.